

7

Numerical Modeling and Simulation of Thermal Energy Storage Systems

7.1 Introduction

The numerical modeling of thermal energy storage (TES) systems has attracted considerable attention recently because of the increased feasibility of a wide array of TES applications. Although appropriate numerical procedures can vary widely depending on the system, the impetus for their use can almost always be attributed to cost and time constraints. For example, experimental methods to assess performance in TES systems can be quite costly. Additionally, analytical models can be subject to extensive assumptions that render models incomplete, but are necessary since the exclusion of such assumptions can make equations overly complicated and cumbersome to evaluate. Therefore, there has been a growing need for numerical models to describe TES systems, thereby allowing computational methods to help solve governing equations. As a result, much of the research regarding this subject reflects the advancement of numerical analysis as a very sophisticated field.

Over the past few decades, advances in computing technology have made numerical analysis much more of an acceptable technique. However, numerical methods have been in use for centuries; even prominent mathematicians such as Isaac Newton and Leonhard Euler developed algorithms that are still used today in optimization problems. Because of the complicated form of the governing equations used in heat transfer and fluid flow, solving numerical equations in TES applications is more tractable with modern computers.

Numerical analyses differ from analytical methods in that they do not solve governing equations explicitly; rather they use approximations that make the equations solvable to a certain tolerance. For fluid flow in three dimensions, for example, pipe flow, solving the Navier–Stokes and continuity equations results in a function that allows velocities and pressures to be specified continuously within the domain. However, for more complex situations, for example, a pipe elbow, the introduction of a complicated boundary condition results in a difficult problem, which, in most cases, is too cumbersome to solve analytically. In these cases, numerical methods are advantageous, and can approximate real-world behavior to a high degree of accuracy. Using an approximated function and a sophisticated algorithm, the fluid flow domain can be discretized so that a finite number of points or volumes can be solved to any desired tolerance, depending on computing power. Most fluid flow and heat transfer problems can be solved by using commercially available software, much of which has been developed over the past several decades. Consequently, numerical analysis and computational codes are now widely used to solve problems.

Perhaps, the most important use for numerical modeling is when experimental or analytical means are not feasible. Complicated dimensional analysis coupled with scale modeling can be expensive and time consuming, whereas with some commercially available software, modeling design platforms can be combined with computational solvers to simulate many processes accurately. Although analytical means can provide high accuracy in the form of continuous solutions, they usually do not represent real scenarios and, if they do, assumptions are usually made, which neglect certain effects, such as radiation or contact resistance. The need is also great for computational procedures for the optimization and improvement of existing systems, which permit cost to be lowered and energy resources to be used more efficiently. For new TES systems, numerical techniques can greatly aid design. For TES systems already in use, numerical techniques can be used to properly identify locations, causes, and magnitudes of losses and help develop more efficient operational strategies. Potential retrofits of existing systems can also be simulated and assessed using numerical techniques, saving money and time compared to experimental approaches.

This chapter describes and illustrates various numerical approaches and methods for the modeling, simulation, and analysis of sensible and latent TES systems. An overview of the approaches, methods, and applications in numerical analysis is presented, after which a more detailed description of the finite volume approach, which is commonly used, is provided. Several case studies are considered to illustrate numerical techniques for both sensible and latent systems. The chapter concludes with a summary of the methods used and the trends observed.

7.2 Approaches and Methods

For any problem, there is often more than one technique that will result in an adequate solution. Similarly, for numerical analysis, there are many techniques available to simulate real-world processes, with varying levels of success. This section provides a brief overview of several techniques used in typical analyses of TES applications, with an emphasis on numerical simulation.

Although there are hundreds – perhaps even thousands – of published works on numerical analysis in the realm of TES, they have many similarities. Generally, numerical analysis is the study of developing or using algorithms to solve continuous problems in mathematics. In most cases, an exact solution to an equation or system of equations is not obtainable and numerical analysis can provide approximate solutions to a high degree of accuracy.

Consider, for example, the problem of solving for the perimeter of a circle with diameter 1. While ancient mathematicians had varying success in approximating the now well-known irrational number π ; it was not until Archimedes of Syracuse (~250 BC) developed a numerical algorithm to approximate π that the accuracy was increased to three decimal places. By the method of exhaustion, he drew a large n -sided polygon outside of the circle, then another n -sided polygon just inside of the circle and calculated the perimeter of each. Since the value of π must lie between these two values, he deduced by drawing a 96-sided polygon that π must have a value between 3.1429 and 3.1408. Through methods such as this, mathematicians, scientists, and engineers have been using numerical analysis to approximate solutions for thousands of years.

For most numerical analysis problems in the real world, the challenge is not in solving a single value (such as π) but a continuous function representing scalar and/or vector quantities in a finite domain. In these cases, unless the governing equations and boundary and initial conditions are in the simplest forms, the domain must be *discretized* in order to obtain meaningful results. Discretization refers to the segregation of a volume into a discrete number of nodes or volumes in order to approximate the solution as a series of finite values or vectors. Although some TES applications of numerical analysis do not rely on discretized schemes (see Section 7.3), the great majority of work in the literature is concerned with discretized problems.

Currently, there are many commercially available software programs that allow numerical analyses for TES applications. These are mainly of two types: finite element methods (FEMs) and finite volume methods (FVMs). Spectral methods as well as finite difference methods are also common in similar applications, but of the four, the FVM and the FEM are the most abundant in the

literature, since they are much more attractive in terms of versatility. At the simplest level, the main difference between the two is the method of discretization. The FEM divides the domain into a number of elements or nodes (points), while the FVM separates the domain into volumes or cells. Both the methods use various techniques in order to achieve convergence.

The FEM generally solves the system of equations (i.e., the strong form of the problem) by first transforming to an equivalent variational (or weak) form of the problem. Then, by employing a specific method (Galerkin methods are the most common), the system is ultimately converted to a system of linear equations represented by a matrix equation, which can be solved using a sparse matrix solver for larger systems. This is a rather simplistic description of the FEM method; for a much more effective treatment of the subject, the reader is referred to Hughes (2000). FEMs have the widest range of applications, since both solid and fluid mechanics can effectively be modeled; however, it is much more computationally expensive than other techniques, which is the main reason FVMs are most often used in TES applications.

In the FVM, the initial solution is essentially guessed, and a formal integration of each volume using the Gauss divergence theorem indicates the errors between cells. This theorem states that the outward flux through a surface equals the volume integral of the divergence inside the surface. In simpler terms, the net flow of any property out of a volume must equal the sum of sources less the sum of sinks in the volume. The computational domain is updated iteratively based on the errors in adjacent volumes and is converged to specified residual error limits.

Although there are advantages to both techniques, the FEM generally is the superior choice when dealing with changes in domain. For instance, the FEM is preferred in cases where elastic deformation, contraction, or expansion of the physical domain may occur, for example, in crash tests in automobiles. The FEM also allows for a varied tolerance according to geometry, so that higher precision can be obtained in areas of importance, reducing the overall cost of simulation. The FEM is often used on structural mechanics and other problems where a discontinuous trend is expected in the results.

The FVM has been used extensively in computational fluid dynamics (CFD), since its conservative nature allows for a good simulation of many fluid flow phenomena. Unstructured or abnormal meshings are readily created with the FVM and can be structured to increase cell density in areas of importance, which, like the FEM, reduces the cost of computation. For this reason, FVMs are normally used for the simulation of complex TES systems, especially since fluid motion and heat transfer equations can be coupled to achieve highly accurate solutions.

This chapter focuses on the utilization of FLUENT, an FVM commercial code, to simulate problems involving sensible and latent TES. A brief overview of selected applications in the literature follows, along with a more detailed examination of the simulation and modeling procedures and the algorithms used in this software.

7.3 Selected Applications

Some of the numerical techniques and applications in the literature are briefly reviewed here. Although the field of TES is broad, most TES research is concerned with space heating or cooling, so this review focuses on applications of these types. This review is not intended to be comprehensive, but rather covers selected informative applications of numerical analysis in both sensible and latent TES.

In sensible TES design, considerable research has been reported on such stores as stratified water tanks, cold and warm water storage, rock bed TES, packed-bed TES, and others. Numerical analysis can assist greatly in reducing costs that would otherwise be incurred to construct and perform experiments, and can model real processes accurately, often with relative ease. For example, Chen *et al.* (2006) considered a vapor compression refrigeration cycle with a cold water TES. Three system types with different water cycle patterns are theoretically analyzed and simulated using numerical techniques. Although the physical system was not simulated directly using a finite volume approach, the numerical solution involved solving a system of partial

differential equations, likely based on finite difference models. In such cases, the exact numerical procedure is not explicitly defined, but the usefulness of such methods is clear: performance investigations and efficiency comparisons can be computed without resorting to experiments, reducing investments of time and money. In another study using numerical optimization, Zohoor and Moosavi (2008) developed a numerical model for optimizing a solar TES system. The hybrid storage system consists of both a hot water tank acting as a sensible storage and a paraffin tank for latent heat storage. A computational approach is used to optimize the charging and storage time schedules that coincide with available solar radiation conditions.

In the two examples described, numerical approaches are used to solve systems of equations that rely on analytical approximations. For example, convective heat transfer rates or flow fields are solved using laminar flow principles. Another useful application of numerical analysis is to compare these approximations, as is done in a study by Ismail and Stuginsky (1999). Here, a packed-bed model for both sensible and latent storage is investigated, and groups of models are examined to determine their accuracy under various system criteria. Four groups of models with different energy expressions are monitored, using a porous-medium method when the heat transfer fluid is of concern. That approach demonstrates well the usefulness of numerical analysis: bed particle size, void fraction, and particle material can be varied to illustrate the advantage of some models, depending on TES conditions.

Another feature of numerical analysis is that all-encompassing models can be constructed to simulate the transient behavior of TES systems. Finite volume or finite difference models are usually used for this purpose and, depending on the user-defined boundary conditions, pressure, temperature, and phase change phenomena can be observed at any point in the system, depending on how grid structures are set. An example is presented by Ghaddar and Al-Maarafie (1997), who considered a thermally stratified solar TES tank. A spectral-element method is employed, which is an FEM with good convergence properties. Their two-dimensional model is used to analyze a cylindrical storage tank and compared with both experimental data and a one-dimensional plug flow model. The spectral-element model presented in Ghaddar and Al-Maarafie (1997) was found to be superior for representing experimental data. Similarly, Oliveski *et al.* (2003) applied numerical approaches to simulate experimental data, but they included more effects (e.g., turbulence) and considered both forced and free convection. The developed numerical model is observed to be accurate in simulating the experimental process, reinforcing the advantage of numerical over corresponding analytical techniques.

Numerical simulations via commercial codes are popular, and greatly facilitate computational assessments for TES and other applications. Shah and Furbo (2003) utilized FLUENT to determine entrance effects in a solar hot water tank. The finite volume approach incorporated in this software permitted the construction of three separate inlet jets and the evaluation of their first- and second-law efficiencies. The simulated results were validated with experimental data and aided an investigation of efficiencies when flow rate and thermal conditions were varied.

The above applications of the numerical approach generally simulate or numerically solve for parameters relating to sensible TES systems. Although the concepts for latent TES are similar, a number of other variables need to be addressed in latent TES and can greatly complicate calculations. For example, density changes during solidification and melting are difficult to model, especially when natural convection is taken into consideration. However, recent advances in computing and numerical codes have permitted the modeling of latent TES processes and the optimization of latent TES systems. These include ice-on-coil systems, packed-bed encapsulated phase change material (PCM) systems, ice slurry systems, and microencapsulated systems. The most useful and readily observed applications are concerned with the former two systems, and therefore are the focus of attention here.

Erek and Ezan (2007) reported a numerical and experimental study of the charging process in an external-melt ice-on-coil TES system. The numerical procedure was simplified by considering a small section of the tank and exploiting symmetries. The control-volume approach used described the system dynamics and accurately predicted the effects of heat transport fluid (HTF) flow rate

and inlet temperature on the storage characteristics of this cold storage tank. Such characteristics include heat transfer rate, total stored energy, and energy efficiency.

Kiatreungwattana and Krarti (2002) reported another numerical application on an ice-on-coil TES system, focusing on an internal melt system during both charging and discharging. The numerical scheme allows a parametric analysis, so that the brine HTF inlet flow rate and temperature as well as the duration of the charging and discharging cycles could be varied to indicate their effects on overall performance. Partial charging and discharging processes are also considered and the model was validated with experimental data.

An increasingly popular latent TES application is based on encapsulated PCMs. As with latent or ice-on-coil TES, these can be divided into two groups: those which use numerical techniques to solve problems concerned with the packed-bed encapsulates as a whole and those which are concerned with analyses involving single capsules.

Most of the numerical procedures observed in the recent literature concerning packed-bed encapsulated TES deal with warm TES using paraffin waxes. Zukowski (2007) analyzed the heat transfer characteristics in a ventilation duct filled with encapsulated paraffin wax in rectangular configurations. He considered a three-dimensional transient model, which is used to predict the effects of capsule geometry and configuration on heat storage. Introducing parallel connectors downstream from the inlet is found to make the heat storage and retrieval more uniform. Benmansour *et al.* (2006) provided a two-dimensional transient analysis of a cylindrical storage tank filled with uniformly sized spherical capsules. The paraffin wax in the randomly packed capsules exchanges heat with air, acting as a heat transfer fluid, and the resulting model is found to agree favorably with observations.

Kousksou *et al.* (2005) proposed a two-dimensional approach to simulate the temperature field in a cylindrical container containing spherical capsules for ice storage. Using the porous-medium model along with the average Nusselt number for such flows proposed by Churchill (1983), the charging and discharging processes are evaluated. Density variations within the HTF are considered and the system is run in both vertical and horizontal positions. The optimal case occurs with the tank in the vertical position, when natural convective currents coincide with forced convection currents.

In addition to macroscopic views of packed-bed encapsulated TES systems, microscopic views that more correctly describe the inner flow networks in such systems are also popular. These can be helpful in determining viscous dissipation and the effect of capsule size, configuration, and orientation. Ismail *et al.* (2003) proposed a finite difference method to simulate the solidification of water in a spherical capsule. A moving-grid scheme is used to enhance the accuracy of the algorithm. The effects of shell size, as well as PCM internal and exterior temperatures, are found to be related to liquid fraction and solidification times.

Other geometries besides spheres have been analyzed numerically. De Souza and Vielmo (2005) investigated the freezing and melting of water in tubes, accounting for natural convection and density changes during the phase change. This analysis is applicable to cylindrical capsule geometries. Wei *et al.* (2005) reported numerical and experimental simulations for spherical, cylindrical, plate, and tube geometries, using the finite volume approach. The capsules in this case are constructed of stainless steel and contain paraffin wax, and are packed in a bed-like geometry and exposed to a cross-flow heat transfer fluid. The model agrees well with the experimental heat transfer rates.

Pinelli and Piva (2003) used FLUENT to investigate a vertical cylindrical cavity heated from above. In this study, the top and bottom of the upright cylinder are maintained at temperatures higher and lower, respectively, than the solidification temperature of the PCM (*n*-octadecane, a paraffin wax). Convective heat transfer occurs from the sides of the cylinder to the atmosphere, defining the boundary conditions that permit the numerical code to solve the problem accurately and examine the flow fields, temperature distributions, and total energy stored. These parameters are also obtained experimentally with a heating and cooling system controlling the upper and lower parts of the cylinder and a Styrofoam belt across the sides. The two sets of results agree reasonably well.

Assis *et al.* (2007) demonstrated the ability of FLUENT to analyze complicated flows accurately. In this study, a sphere containing a commercially available paraffin PCM is monitored qualitatively

and quantitatively during melting, induced by maintaining its outer shell at a constant temperature above the melting temperature. The change in density from solid to liquid is accounted for, as are the minor density differences in the liquid state due to temperature variations, which lead to convective flows. The sphere diameter and wall temperature are varied, and the simulation is validated in large part by visual studies of the moving solid–liquid interface with time. Relationships between various dimensionless parameters are determined, and the model is tested for grid size and time step independence, with good results. However, the computational time ratio was found to be over 300:1, that is, 300 s of computational time is required for 1 s of real flow time. Thus, a typical simulation required several days, even using a powerful computer by the standards at the time of the investigation. This example demonstrates that computational accuracy often needs to be balanced against simulation computational cost. Although computing power continually increases, many phenomena are still better neglected or simplified in numerical codes, where only minor losses in accuracy are caused.

7.4 Numerical Modeling, Simulation, and Analysis of Sensible TES Systems

One of the most important aspects of a CFD code is its ability to incorporate governing equations and conservation laws. For example, a code must apply conservation of energy and momentum and continuity principles during simulations of steady state and transient behavior. Here, we explain how a commercially available computational heat transfer and fluid flow code, ANSYS FLUENT 6.3, handles these phenomena in TES applications.

Since TES stores thermal energy in a medium for later extraction, all computational codes relating to TES need to account for energy conservation. Additionally, both sensible and latent TES systems usually involve one or more fluids. For instance, many cold latent TES systems employ an HTF to deliver heat to or from the PCM, and sensible TES media like rock beds transfer heat to or from a surrounding fluid, often air. The finite volume techniques used in the solution algorithms in FLUENT 6.3 are shown in this section to be able to handle such situations and their complicated governing equations.

In this section, geometric modeling techniques in fixed-grid schemes are outlined, including grid size and boundary layer construction in two and three dimensions. Also, the governing equations are presented, which the various FLUENT algorithms solve to analyze heat transfer and fluid flow. Attention is focused on the more complicated models that allow for phase change, natural convection, and viscous heating. Then, the simulation procedures used in most TES simulations are briefly explained as is the post-processing of the obtained data. Finally, the use of the data for thermodynamic analysis is described, illustrating how it can help present information about performance criteria and efficiencies in an effective manner.

7.4.1 Modeling

Proper and effective modeling is essential for the accuracy of numerical simulations. The geometry that one models or creates for use in computational analysis must satisfy three main criteria. That is, it must

- be constructed so as to facilitate accurate simulation of real-world scenarios;
- be sufficiently simple and/or contain fewer volumes to permit simulations with available computing power and within time constraints; and
- be sufficiently complicated or contain sufficient computational volumes to achieve accurate results.

These criteria can be illustrated with a simple example. Using ANSYS GAMBIT software, we construct a two-dimensional duct of length 100 cm and width 20 cm, in which air flows from left

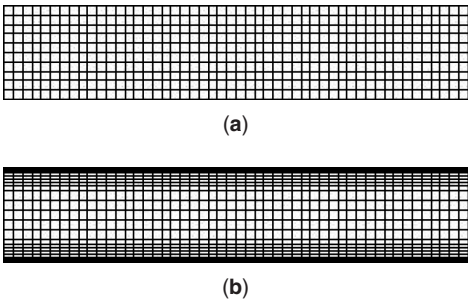


Figure 7.1 Grid structuring for two flow cases. (a) 500 cells of equal size and (b) 1050 cells with increased cell density at wall boundaries

to right at a speed of 10 cm/s. Owing to the no-slip condition at the duct walls, a velocity boundary layer develops in the duct and a velocity profile exists. Note that due to the length of the duct, the flow is considered laminar so that no turbulence modeling is needed.

Two cases are examined (see Figure 7.1). The grid structure for the first case contains 500 rectangular volumes (cells) of equal size and for the second it contains 1050 rectangular volumes and a concentration of such volumes in the upper and lower boundary layers.

Both grid cases fit the system configuration but allow different results to be obtained. The duct is of the same size in each case, and the inlet and outlet criteria are identical. Thus, the first criterion mentioned earlier is satisfied for both the cases. The second criterion (the model should be sufficiently simple that the simulation can be carried out in a reasonable amount of time) is also satisfied. That is, both the cases were solved transiently in a matter of seconds using a somewhat outdated laptop with a Pentium M 1.6 GHz processor with 512 Mb DDR RAM, a time step of 0.5 s, 50 iterations, and a total of 25 s of flow time. The third criterion is significantly impacted by the grid structuring and cell density within the computational domain. In the first case, the flow is treated equally at all points and extra attention is not paid to those areas that experience the largest velocity gradients, that is, near the walls. The situation in the second case is different, as most of the cells in the computational domain are located along the walls. The finer grid near the walls ensures that information is not lost in these areas of the flow. Since all conservation laws are solved to a specific tolerance (as explained in more detail in Section 7.4.3), locating more cells in areas of higher gradients improves predictions in those areas.

Figure 7.2 depicts the simulated velocity profiles for the two cases. The velocity profiles in Figure 7.2(a) and (b) differ. The first (Figure 7.2a) exhibits a sharper increase in velocity as the

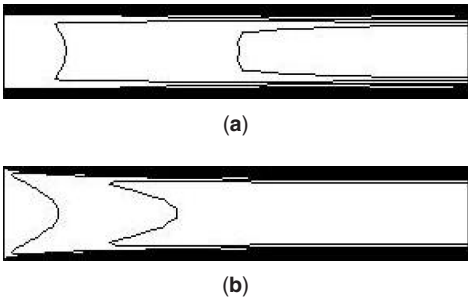


Figure 7.2 Velocity profiles for two flow cases, characterized by the grid structures in Figure 7.1. Each solid line represents a contour of constant velocity

distance from the wall increases, with an almost constant boundary layer thickness. It is apparent from fluid mechanics principles that the first case (Figure 7.2a) does not accurately depict the process, since the boundary layer thickness should start at zero and increase gradually over the flat plate (see Section 1.5.6). Further, the transition in the first case from a zero velocity to the centerline velocity is not smooth, as should occur for laminar fluid flow. The second case (Figure 7.2b) characterizes the flow more accurately, with the velocity profiles transitioning smoothly across the duct and the boundary layer thickness changing in a more reasonable manner. Thus, the second case (case b) attains a more accurate numerical simulation than case a and thus better satisfies the third criterion above.

The previous example illustrates the need for care when constructing a computational domain for a TES simulation. Although heat transfer is not accounted for in the example, the same steps in terms of developing appropriate meshing or grid procedures must be taken to ensure that thermal boundary layers and temperature profiles are accurately depicted.

In addition to ensuring that the above three criteria are met, there is a need to develop independence tests with any numerical model. These include grid size, grid orientation, and time step independence tests, as well as in some cases far-field boundary independence tests. Furthermore, model validation is required before results generated by a numerical code are utilized.

A grid size and orientation test is needed to help in model validation and to assure accuracy. The need for a grid size test is illustrated in part by the above example. By adjusting the grid size slightly and, in some cases, the orientation in different ways with respect to temperature and velocity profiles, the dependence of numerical solutions on these small changes can be observed. If the simulation results change significantly, grid refinement is necessary. If the results do not change significantly, the numerical procedure is established to be independent of grid meshing changes and the geometric constraints for numerical simulation are satisfied.

The time step independence test is similar and is intended to ensure that time steps in simulation are as large as possible to reduce computation time while being sufficiently small to provide accurate solutions. If the time step in an unsteady flow problem is increased significantly, numerical solutions lose accuracy because information details are lost between time steps. For example, in the case considered earlier (see Figure 7.2b), if the time step is increased from 50 steps of 0.5 s to a single step of 25 s, the velocity profile that results can be seen in Figure 7.3. This profile differs qualitatively and quantitatively from the one in Figure 7.2(b), mainly because of the lack of information transferred from one time step to another. To ensure solutions are independent of time step, care should be taken to retain an adequate amount of flow information by decreasing time step, while decreasing computational time by increasing time step. In complicated problems, the choice of time step is often crucial, as it can mean the difference between simulation times ranging from a few hours to a few days.

In some cases, a far-field independence test is also required to assure the accuracy of a simulation. In those cases, a well-developed profile may be needed or assumed in the problem description, and care must be taken to ensure that the length or size of the boundary does not detract from the results. A simple example is provided by the cooling of a large, heated rock at the bottom of the ocean. Since it is not necessary to model the entire ocean, a smaller body of water can be created for modeling purposes, but the size of the water body would have to satisfy far-field independence tests. That is, the water body must be created so that its boundaries match the conditions, for



Figure 7.3 Velocity profile with a single time step of 25 s

example, temperature gradients, far from the system being assessed. If the size of the smaller water body is established correctly, loss of simulation data is avoided and, in this example, a “virtual” ocean is developed.

Together, the various independence tests ensure that a model achieves accurate results. The tests can help identify grid configurations, which increase computing speeds without significant loss of accuracy.

7.4.2 Heat Transfer and Fluid Flow Analysis

During TES numerical simulation, governing equations are solved to determine velocity, pressure, and temperature fields. In general, the governing equations involve energy and momentum balances and the continuity equation. Sometimes, simplifications can be made. For cases with no moving fluid, only the energy equation needs to be considered. For cases with fluid flow but no heat transfer or heat generation, the momentum and continuity equations must be invoked. For the case of combined fluid flow and heat transfer, all equations must be solved within specified tolerances (see Section 7.4.3).

For sensible TES, the energy equation in FLUENT is usually expressed as follows:

$$\frac{\partial}{\partial t} (\rho h - p) + \nabla \cdot (\vec{V} \rho h) = k \nabla^2 T + \Phi \quad (7.1)$$

Here, h denotes specific enthalpy, p pressure, ρ density, and \vec{V} the velocity vector, while k and T denote thermal conductivity and temperature, respectively. This equation expresses the principle of energy conservation, but is simplified somewhat by assuming that kinetic and potential energy effects, radiation effects, and source terms from chemical reactions or other heat sources are negligible and that the medium is homogenous. The last term on the right-hand side of Equation 7.1 accounts for viscous heating and can be expressed in three-dimensional Cartesian coordinates as follows:

$$\Phi = \mu \left[2 \left(\frac{\partial u}{\partial x} \right)^2 + 2 \left(\frac{\partial v}{\partial y} \right)^2 + 2 \left(\frac{\partial w}{\partial z} \right)^2 + \left(\frac{\partial v}{\partial x} + \frac{\partial u}{\partial y} \right)^2 + \left(\frac{\partial w}{\partial y} + \frac{\partial v}{\partial z} \right)^2 + \left(\frac{\partial u}{\partial z} + \frac{\partial w}{\partial x} \right)^2 \right] \quad (7.2)$$

This equation is used in all subsequent TES case studies. Care must be taken for media undergoing phase change. For media not subject to phase change, the sensible specific enthalpy from Equation 7.1 can be derived using incompressible assumptions as

$$h(T) = h_o + C(T - T_o) \quad (7.3)$$

where the subscript o refers to the reference state, which is typically at a temperature of 298.15 K. This assumption of incompressibility is normally reasonable since in most cases water or some liquid solution, which behaves like an incompressible fluid, is used as the heat transfer fluid and/or storage medium.

Aspects of computationally solving the flow field for the general energy equation are now outlined. Fluids must adhere to the principle of conservation of mass. For incompressible substances, the continuity equation can be written as

$$\nabla \cdot \vec{V} = 0 \quad (7.4)$$

The Navier–Stokes equations, or flow energy conservation equations, also apply:

$$\rho \frac{\partial \vec{V}}{\partial t} + \vec{V} \cdot \nabla \vec{V} = -\nabla p + \mu \nabla^2 \vec{V} + \rho \vec{g} \quad (7.5)$$

These equations depend primarily on the velocities and pressure differentials within the velocity field. The change in velocity at any point in the fluid depends on the pressure gradient at that point ∇p as well as on the viscous dampening effect, represented by $\mu \nabla^2 \vec{V}$.

For temperature differences like the ones experienced in most TES applications, which normally would be considered “small,” it is often useful to consider natural convection as well, by accounting for the small density differences experienced when the temperature distribution in a fluid is nonuniform. Then, the *Boussinesq* model is often preferred, since it achieves faster convergence by solving the energy and continuity equations using a constant density. For the Navier–Stokes equations, the natural buoyancy term (the far right term of Equation 7.5) is solved using the Boussinesq density approximation:

$$(\rho - \rho_o) g \approx -\rho_o \beta (T - T_o) g \quad (7.6)$$

This approximation is valid provided density differences are not large, in which case $\beta (T - T_o) \ll 1$. This condition applies for TES heating and cooling applications, and is adopted throughout the case studies presented here, which take natural convection into consideration.

Although the above discussion simplifies the governing equations in many TES systems, the approach is sufficient in analyzing basic systems. These equations provide a useful and simple means to achieve an accurate simulation and analysis for some of the sensible TES systems included in the case studies in Section 7.5.

Note that FLUENT includes sophisticated turbulence modeling and combustion packages, which are not utilized here and are beyond the scope of this discussion.

7.4.3 Simulation

The computational procedures used in FLUENT are complex and much research has gone into developing the many algorithms used in FLUENT to solve the differential equations in complex fluid flow and heat transfer problems. As a result, numerous algorithms and discretization schemes are available in FLUENT. Only those pertinent to sensible heat storage are considered in this section.

As noted earlier, FLUENT uses a finite volume approach to solve for domain data. Grid and mesh construction splits each domain into a finite number of volumes (cells) and the relationships between adjacent cells are computed over their adjoining faces (facets). To solve the necessary governing equations from Section 7.4.2, several initial and boundary conditions must be established, including cell initializations (initial conditions) and wall or flow information concerning boundaries. If the energy balance (Equation 7.1) is enabled, each cell must be assigned an initial temperature and pressure by the user before computation for transient solutions begins. In the case of fluid flow, the velocity and pressure vectors in all cells must be initialized so that Equations 7.4 and 7.5 can be solved. The boundary conditions, which must be applied to all wall surfaces (denoted by W in the following equations) as well as inlet and outlet flows, are equally important. For geometries which have walls, a “no-slip” boundary condition is often employed, which establishes a zero velocity on the surface. In other words, for those wall facets \vec{f} that are part of the no-slip wall regime, the velocity vector is zero, or

$$\vec{V} (\vec{f} \subset W_{ns}) = 0 \quad (7.7)$$

All cell data is extrapolated from cell centers, for which information is stored, to cell facets by a linear interpolation scheme.

In many cases, the number of computational volumes can be greatly reduced by splitting flow regimes into symmetric segments, as is readily visible in Section 7.7.2, where a “slip” condition is applied.

The slip boundary condition requires zero-shear stress at points of flow symmetry:

$$\frac{d\vec{V}}{d\vec{n}} \left(\vec{f} \subset W_s \right) = 0 \quad (7.8)$$

For outflow zones, where fluid is expected to flow out of the domain, FLUENT extrapolates the required information from the interior of the domain. A zero diffusion flux is assumed for all flow variables in outlet type flows. In other words, for any flow variable γ ,

$$\frac{d\gamma}{dz} \left(\vec{f} \in W_{out} \right) = 0 \quad (7.9)$$

where the subscript *out* refers to the outlet boundary region. The symbol γ can refer to any of the velocity, temperature, or pressure vectors. This criterion can create some problems with the robustness of simulations with respect to far-field boundary conditions, so care must be taken when choosing boundaries of this type.

Other boundary types include velocity inlet, where flow velocity and temperature at the inlet must be indicated. Convective and conductive walls, adiabatic walls, and constant-temperature walls are some of the many useful conditions that can be employed at boundaries as well. These conditions are explained in Section 1.6.

A pressure-based solver is used in the case studies investigated here, since all of the materials used are assumed incompressible. Flows are therefore governed solely by pressure differentials. However, for the case of natural convection using the Boussinesq model in Section 7.4.2, the pressure is discretized using a body-force-weighted scheme. In this scheme, facet pressures are computed assuming that the normal gradient of the difference between pressure and body forces is constant. This approach works well in most natural convection cases.

The pressure-based solver employs an algorithm that belongs to a general class of methods called *projection methods* (Chorin, 1968). In this method, continuity is achieved by solving a pressure correction equation. This equation is derived from the continuity and momentum equations, outlined earlier, in such a way that the pressure/velocity field satisfies the continuity equation. Since the differential equations that must be satisfied are nonlinear by nature and coupled, the solution must be obtained by iteration in a closed loop until convergence is achieved within the specified tolerances. A schematic of the general pressure-based solution process is shown in Figure 7.4.

The premise of the segregated pressure-based algorithm is that the variables (u , v , w , p , and so on) are solved sequentially (segregated). Although this approach is somewhat tedious computationally, advances in computer speed and memory capacity make it an excellent choice for more simple problems. Then, the SIMPLE algorithm for pressure-based segregated solvers is used.

The SIMPLE (Semi-Implicit Method for Pressure-Linked Equations) algorithm follows the basic outline of the flow diagram in Figure 7.4, but each step is somewhat more complicated. Owing to the complexity of the algorithm when applied to discrete cell volumes, the general outline of the model is described in lieu of a more involved explanation, which is beyond the scope of this discussion.

Since all pertinent flow and energy information is stored in the centroid of each cell, the mass, continuity, and energy equations must be applied at cell facets. To do this, the momentum and continuity equations are discretized using projected face values from the centers of adjacent cells, using the Green–Gauss cell-based method:

$$\gamma_f = \frac{\gamma_{ca} + \gamma_{cb}}{2} \quad (7.10)$$

In other words, the facet values of all variables are taken as the average at the centers of the adjoining two cells, “*ca*” and “*cb*,” and all variables in the solution can be seen as piecewise linear at any time. But the overall solution appears continuous rather than discrete since the number of cells is large and each cell is small compared to the total volume.

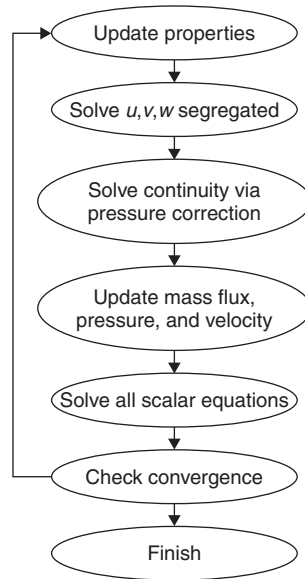


Figure 7.4 Solution procedure flow chart for the coupled pressure-based solution algorithm, such as the one used in the SIMPLE method

The first step in the SIMPLE algorithm is to solve the momentum equations sequentially, by guessing the pressure field, say p^* . The pressure field must subsequently be improved, and much of this algorithm is devoted to that task. As the solution loop progresses, the algorithm updates the pressure field continuously until a solution is achieved within specified tolerances.

If the pressure field, p^* , is not initially correct, the continuity equation, which is evaluated next, is not satisfied. A correction factor is then introduced in order to correct the face fluxes so that continuity can be achieved. The corrected face fluxes for each cell are then substituted back into the discrete continuity equation to obtain a discrete equation for the pressure correction in each cell. The pressure correction equation is achieved by solving this discrete pressure correction equation using the algebraic multigrid (AMG) method. Details of this method are complex and are not discussed here, but it is noted that the AMG method does not depend on problem geometry and thus can be used for complicated problems like TES applications.

Once the pressure correction equation has been obtained, it is used, along with several user-defined under-relaxation factors, to correct all cell pressure values and face fluxes. The penultimate step in the algorithm is the solution of the energy equations using the corrected continuity and momentum equations. Once the energy equations, which are important in any heat transfer application and which differ from zone to zone, are solved, the residual error of the conservation equations is checked, completing the algorithm.

The residual error is the total summed differences in the governing equations from cell to cell. Since the equations cannot be solved perfectly using the cells in the computational domain, there are always errors when updating solutions. The error for each of the x , y , and z velocities, along with the continuity and energy equation errors, are summed separately over the domain. If the result is below the specified tolerance, the solution is deemed to have converged. If the convergence criteria are not met, the solution has not converged and the corrected pressure field becomes the new pressure field guess in the first step of the algorithm. The process is then repeated iteratively.

The residual values are dependent on the scale of the problem. For example, a large system with many computational domains and a fast moving flow would typically have a much larger

residual error than a small system with little flow. If the total residual error tolerance is fixed at the same value in both cases, the simpler problem would lose much more information about these differences per cell. Hence, residual values are often scaled based on cell values. A simplification of the normalized or scaled residual can be obtained as follows. For any domain parameter, γ , a cell value is obtained by considering neighboring cells, nb , so that $f(nb) = \gamma$, at which the cell residual is $|\gamma - f(nb)|$. Then, the scaled residual over a domain of n cells is

$$Res^\gamma = \sum_{i=1}^n \frac{|\gamma_n - f(nb_n)|}{|\gamma_n|} \quad (7.11)$$

These residuals are applicable to the momentum, continuity, and energy equations, and are automatically implemented in FLUENT whenever the pressure-based algorithm is employed. The scaled residual approach allows for a more accurate solution convergence across a wide range of applications and is used throughout the TES applications herein.

7.4.4 Thermodynamic Analysis

Although the heat transfer and fluid flow analysis allows for TES simulation, thermodynamic analysis is necessary to link the obtained information to physical phenomena. Thermodynamic analysis is concerned with evaluating the mass, energy, entropy, and exergy equations to provide performance and efficiency data. These quantities are described in this section, as is an associated balance equation used for control volume analysis. The method by which physical quantities are monitored using FLUENT for solving the balances is explained.

The mass balance for a control volume is shown in Equation 7.12. Mass can be transferred to or from the control volume, and the difference is the gain in mass of the system:

$$\Delta m_{CV} = m_{in} - m_{out} \quad (7.12)$$

The energy balance is similar. Since energy can be neither created nor destroyed according to the first law of thermodynamics, energy is conserved. For sensible TES applications, kinetic and potential energy effects are usually neglected. The energy balance equation for a single-inlet, single-outlet system is

$$\Delta E_{CV} = E_{in} - E_{out} = Q - W + H_{in} - H_{out} \quad (7.13)$$

The change in energy of the control volume is equal to the net heat added to the system, less the net work done by the system, plus the difference of the enthalpy flow into and out of the control volume with mass flows. The usual sign convention treats heat into a system as positive and work out as negative. Often substances are assumed incompressible, and enthalpy differences can be evaluated as follows:

$$\Delta H = H_2 - H_1 = m(h_2 - h_1) = mC(T_2 - T_1) \quad (7.14)$$

In contrast to mass and energy, entropy and exergy are not conserved. For a single-inlet, single-outlet case with j heat interactions with the surroundings, the entropy balance can be written as

$$\Delta S_{CV} = \sum_j \frac{Q_j}{T_j} + S_{in} - S_{out} + \Pi \quad (7.15)$$

The second law of thermodynamics implies that the entropy of a system increases because of irreversibilities, so the last term of Equation 7.15 is always greater than zero for real applications. The entropy transfer associated with a heat interaction is the ratio of the heat transfer across a

surface to the temperature T_j at which the interaction occurs. For incompressible substances, the entropy change can be simplified:

$$\Delta S = S_2 - S_1 = m(s_2 - s_1) = mC \ln \left(\frac{T_2}{T_1} \right) \quad (7.16)$$

Exergy analysis is useful in TES applications, providing assessments based on the first and second laws and assessing both the quantity and usefulness of energy. As an example, consider cold TES. Since exergy methods treat cold as a useful commodity relative to ambient conditions, more realistic performance assessments are obtained using exergy rather than energy efficiencies. Exergy, like entropy, is not conserved. For a single-inlet, single-outlet case with j heat interactions with the surroundings, an exergy balance can be written as

$$\Delta \Xi_{CV} = \sum_j \left(1 - \frac{T_\infty}{T_j} \right) X_j - W + \epsilon_{in} - \epsilon_{out} \quad (7.17)$$

where the exergy difference for an incompressible substance is

$$\Delta \Xi = \epsilon_2 - \epsilon_1 = m(e_2 - e_1) = mC \left(T_2 - T_1 - T_\infty \ln \left(\frac{T_2}{T_1} \right) \right) \quad (7.18)$$

With these thermodynamic principles, energy (first law) and exergy (second law) efficiencies can be defined. In both cases, the efficiencies are often based on the ratio of the product (or desired) output to total input. Expressions for energy efficiency η and exergy efficiency ψ based on this definition, which are used in the case studies, are as follows:

$$\eta = \frac{\text{Product energy output}}{\text{Total energy input}} = \frac{E_{prod}}{E_{input}} \quad (7.19)$$

$$\psi = \frac{\text{Product exergy output}}{\text{Total exergy input}} = \frac{\Xi_{prod}}{\Xi_{input}} \quad (7.20)$$

To evaluate efficiencies, energy and exergy quantities must be obtained, in general and with FLUENT. For mass flows, the temperature of the flow on a mass-weighted average is preferred. The mass-weighted average temperature obtained by a surface monitor for an outflow containing n facets is defined as follows in FLUENT:

$$\bar{T}_{out} = \frac{\sum_{i=1}^n T_i \rho_i \left| \vec{V}_i \cdot \vec{A}_i \right|}{\sum_{i=1}^n \rho_i \left| \vec{V}_i \cdot \vec{A}_i \right|} \quad (7.21)$$

The mass flow rate is provided as the divisor of Equation 7.21. Surface integrals can also be computed, and are usually used for evaluating the total heat flow through a surface. For a heat flux q , the total surface heat flux for a surface containing n facets is calculated in FLUENT as:

$$Q = \int q dA = \sum_{i=1}^n q_i |A_i| \quad (7.22)$$

In addition, a volume monitor is often used to determine the average temperature in a specified material or section of the domain. For a volume comprised of n elements, the volume average temperature from a volume monitor is

$$\bar{T}_v = \frac{1}{V} \sum_{i=1}^n T_i |V_i| \quad (7.23)$$

The above two methods are used in the case studies and permit calculation of performance parameters for each case.

7.5 Case Studies for Sensible TES Systems

The thermodynamic analysis described in the previous section is applied to several TES case studies. The case studies are chosen to be illustrative and are therefore simple. They are easily repeated and provide useful insights into sensible and latent TES systems. The cases are simulated using FLUENT 6.3, using an IBM Thinkpad laptop with a Pentium M 1.60 GHz processor and equipped with 512 Mb of DDR RAM. This computer is sufficient for performing the calculations with the software (although more computing power is required to attain convergence for complex problems in a reasonable time).

In the following examples, typical uses for ANSYS FLUENT software are outlined. As one of the most popular finite volume solvers in the industry, it is adept at solving many computational fluid flow and heat transfer problems over a wide range of applications. Many examples are cited in the literature in which FLUENT simulates real scenarios, varying from simple to complex. FLUENT can implement a wide range of models, which can be toggled on or off, to handle phenomena such as multiphase flows (e.g., gas diffusion beds), viscous heating, radiation, solidification and melting, acoustics, turbulence, and others. The advantage of commercially available software is relatively straightforward problem setup and solution, although care must be exercised for more complicated applications to ensure that proper models are enabled, residual tolerances are within reason, and computational domains, including boundary and initial conditions, are properly constructed.

Two cases are investigated here, both involving relatively simple FLUENT simulations. The first is natural convection in a hot water storage tank, and is intended to simulate the cooling process for an uninsulated residential hot water tank in ambient conditions. The second case is forced convection in a stratified cylindrical storage tank, where hot water is pumped into the tank as in solar heating applications. Although grid and time step dependence tests are administered, because of the lengthy nature of such tests they are shown in more detail when a complicated case study is undertaken in Section 7.7.2. These examples are intended to provide the reader with an understanding of the usefulness of such software in sensible TES applications.

7.5.1 Case Study 1: Natural Convection in a Hot Water Storage Tank

In this case, natural convection is simulated using FLUENT. This simple case permits some of the basic aspects of the software to be understood and utilized. We consider an upright cylindrical storage tank with a radius of 30 cm and a height of 120 cm. These dimensions are typical of commercial hot water tanks. The tank is assumed to have negligible insulation on its walls and to exchange heat with its surroundings through convective heat transfer only. The hot water tank has an initial temperature higher than that at ambient conditions. The resulting convection and stratification within the tank are examined as time progresses over a 24-hour period. Various physical quantities are considered so as to provide sufficient information to calculate energy and exergy efficiencies.

The sole heat storage and transport medium is water, which provides the sensible thermal storage capacity. The water has an initial temperature of 60 °C and exchanges energy through convective heat transfer with the ambient surroundings at a temperature $T_{\infty} = 20^{\circ}\text{C}$. The simplistic modeling applied here permits the ambient atmosphere to be excluded from the physical domain and instead for a convective boundary condition to be imposed at the tank walls with a heat transfer coefficient of 10 W/m² K. This value compares well with that found in a similar study by Oliveski *et al.* (2003). The tank walls are uninsulated, and this lack of conductive thermal resistance allows the wall to be treated as very thin. The water is assumed to have constant thermophysical properties, including a density of 992.2 kg/m³, a specific heat of 4.182 kJ/kg K, a conductivity of 0.618 W/m K, a dynamic viscosity of 0.000653 kg/m s, and a thermal expansion coefficient of 0.000386/K. These values are taken at 40 °C, the mean temperature of the system and its surroundings.

To create the physical domain and segregate it into finite volumes, GAMBIT software is used. Special care is taken to ensure a higher concentration of cells in regions expected to experience higher thermal and velocity gradients, namely, the inside walls of the tank. This is done to ensure

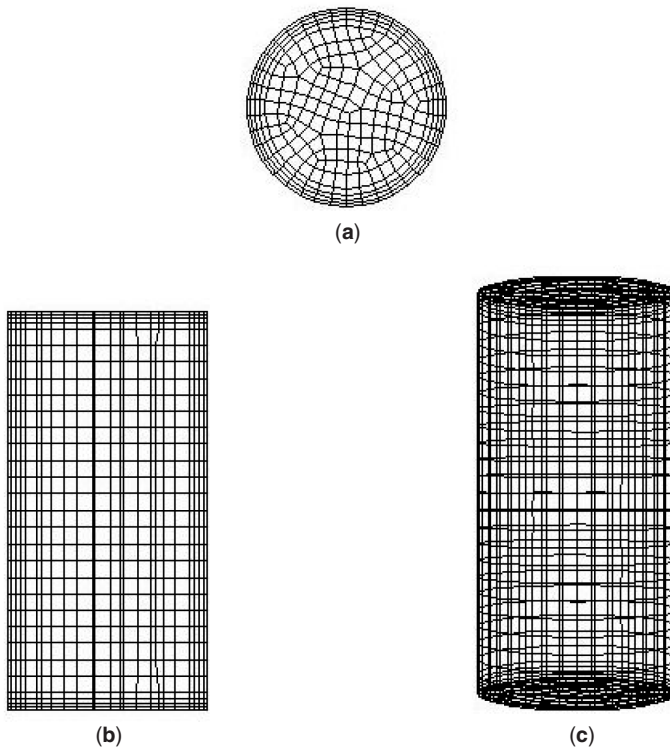


Figure 7.5 Cross-sectional views of the cell density in the (a) radial plane, (b) axial plane, and (c) outer wall regions

greater simulation accuracy, as explained earlier. The cell configurations for horizontal and vertical cross sections through the tank are shown in Figure 7.5, along with a three-dimensional view of the cell distribution in the outer walls.

To establish this cell configuration, a boundary layer is first meshed in all inner faces (walls), using an initial spacing of 1 cm, with a growth factor of 1.2 and four layers in total, giving a total boundary layer thickness of 5.37 cm. Subsequently, the remainder of the volume is meshed using hex elements and a cooper meshing with a spacing of 5 cm, which corresponds to a total of 8580 elements. These configurations are simple to implement with a basic knowledge of GAMBIT, and are chosen because of the good convergence results they yield in the associated FLUENT simulations. No grid size or orientation tests are administered for this case study, but a comprehensive and detailed account of these procedures is given in Section 7.7.2.

Once the computational domain configuration is created, it can be read into FLUENT as a system of nodes and volume types. The remainder of the numerical setup involves setting initial and boundary conditions, temperature monitors, time steps, and residual tolerance values. For this case, the energy balance of Equation 7.1 is enabled, and water properties are set via the Boussinesq natural convection approximation in Equation 7.6. The entire volume is initialized to have zero gauge pressure and a temperature of 60 °C, and the convective heat transfer boundary condition is set using the “Boundary Conditions” panel. The SIMPLE solver is utilized, but the pressure discretization scheme is weighted by body forces, as required for natural convection cases. For natural convection to occur, gravity must be enabled. Here, gravitational acceleration is set to 9.81 m/s^2 in the negative y -direction. Monitors are put in place to record the volume-averaged

temperature in the tank at 5-min intervals, and the residual tolerances are set to 10^{-3} for the x , y , and z velocities and continuity and 10^{-6} for energy. The time step is set to 2 s, a coarse value that eases the simulation. As in grid construction, time step independence is not demonstrated in this case, but is explained in detail in Section 7.7.2. The simulation is then run. With a computational time ratio of about 1:3, the simulation required is about 10 h to complete.

Performance Criteria

Since no mass flow crosses the tank walls and no work is done on the control volume, the energy balance from Section 7.4.4 can be simplified to

$$\Delta E_{\text{sys}} = Q \quad (7.24)$$

The energy efficiency, based on the ratio of product to input energies, can be computed at any time during the simulation, since monitors are in place to calculate the heat loss via the average change in water temperature. The product energy is defined as the recoverable energy in the tank at any time, while the total energy input is taken to be the recoverable energy in the tank at the beginning of the simulation. These two values are evaluated by monitoring the average temperature within the tank at each time step, and the energy efficiency becomes

$$\eta = \frac{E_{\text{prod}}}{E_{\text{input}}} = \frac{H(t)}{H(0)} = \frac{H(0) - Q}{H(0)} \quad (7.25)$$

where

$$H(t) = m [h_{\infty} + C (\bar{T}_v(t) - T_{\infty})] \quad (7.26)$$

The exergy efficiencies are similarly calculated, with no mass flows across the control volume. For simplicity, we assume reversible behavior in the tank with no viscous losses or volumetric changes, so the only system loss is the exergy loss associated with heat leakage:

$$\Delta \Xi_{\text{sys}} = X_I \quad (7.27)$$

The exergy content at each time step of the simulation can be similarly calculated by monitoring the volume-averaged temperature in the tank. Then, the exergy efficiency can be expressed as

$$\psi = \frac{\Xi_{\text{prod}}}{\Xi_{\text{input}}} = \frac{\Xi(t)}{\Xi(0)} = \frac{\Xi(0) - X_I}{\Xi(0)} \quad (7.28)$$

where

$$\Xi(t) = mC \left[\bar{T}_v(t) - T_{\infty} - T_{\infty} \ln \left(\frac{\bar{T}_v(t)}{T_{\infty}} \right) \right] \quad (7.29)$$

The total volume of the system is calculated to be 339 L, corresponding to a mass m of 336 kg. The specific enthalpy of water at the reference-environment condition is given in thermodynamic tables as $h_{\infty} = 83.93$ kJ/kg. Note that, although the tank is taken to undergo a reversible process for simplicity, all other cases have internal irreversibilities.

Results and Discussion

Before considering the performance values calculated from the monitored simulation data, we utilize the field data visualization software in FLUENT. Views of the temperature and velocity (scalar)

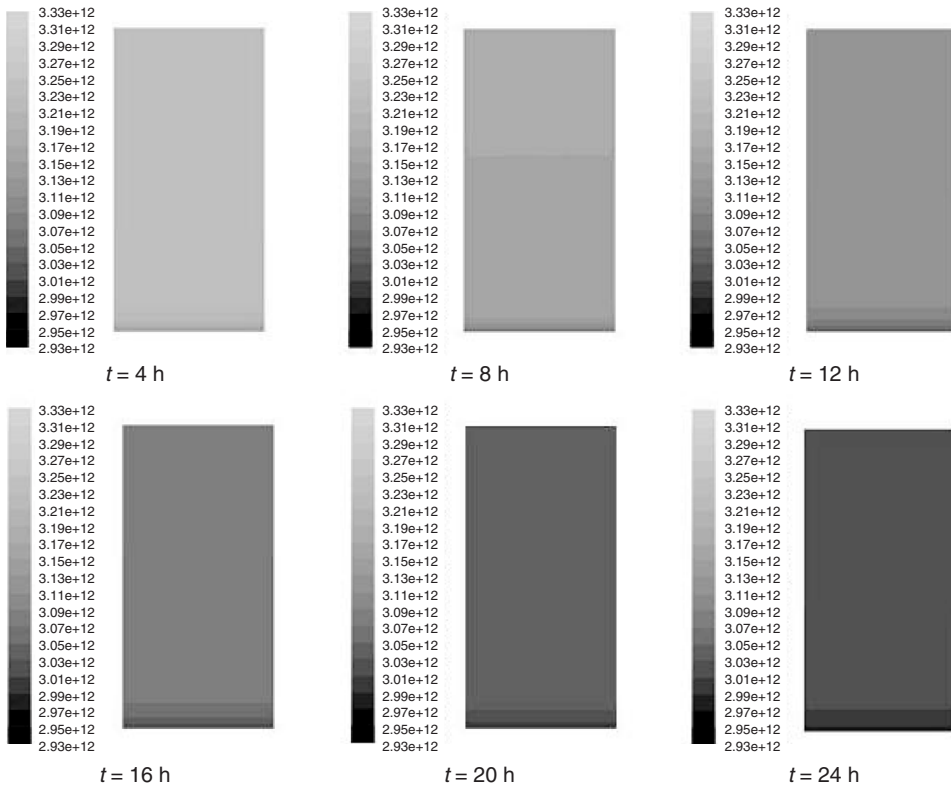


Figure 7.6 Temperature distributions (in K) for the storage tank at 4-h intervals

fields are taken at 4-h intervals. These views are shown for an axial cross section (see Figure 7.5b) in Figures 7.6 and 7.7.

In the temperature fields in Figure 7.6, darker regions indicate cooler temperatures. It is seen that the tank cools considerably as time progresses, and that cooler temperatures exist in the lower parts of the tank, due to natural convection currents, as well as on the tank walls. This is not surprising since the natural convection model is employed and warmer fluids have a lower density than cooler fluids.

From the absolute velocity field of the tank in Figure 7.7, it is observed that the velocities, although small, vary as time progresses. Darker areas represent lower velocities. Two points are apparent in Figure 7.7: the velocity differences in the storage tank decrease with time and the velocities are highest along the tank walls and lowest at the tank bottom. These observations are attributable to natural convection. Since the tank walls experience the highest velocity gradients, the cells nearest to the walls exhibit the lowest temperatures in the domain and the greatest densities, leading to the greatest downward velocity. As time passes, the density variations within the tank decrease as the average temperature within the tank decreases toward the ambient temperature. If the simulation is continued for enough time, all velocity vectors would become zero. Note that small eddy currents are present in the tank interior due to the fact that FLUENT automatically uses a turbulence model for such situations. Compared to thermal energy losses, the losses due to viscous heating in both laminar and turbulent cases are extremely small and therefore are assumed negligible for this and all subsequent TES case studies.

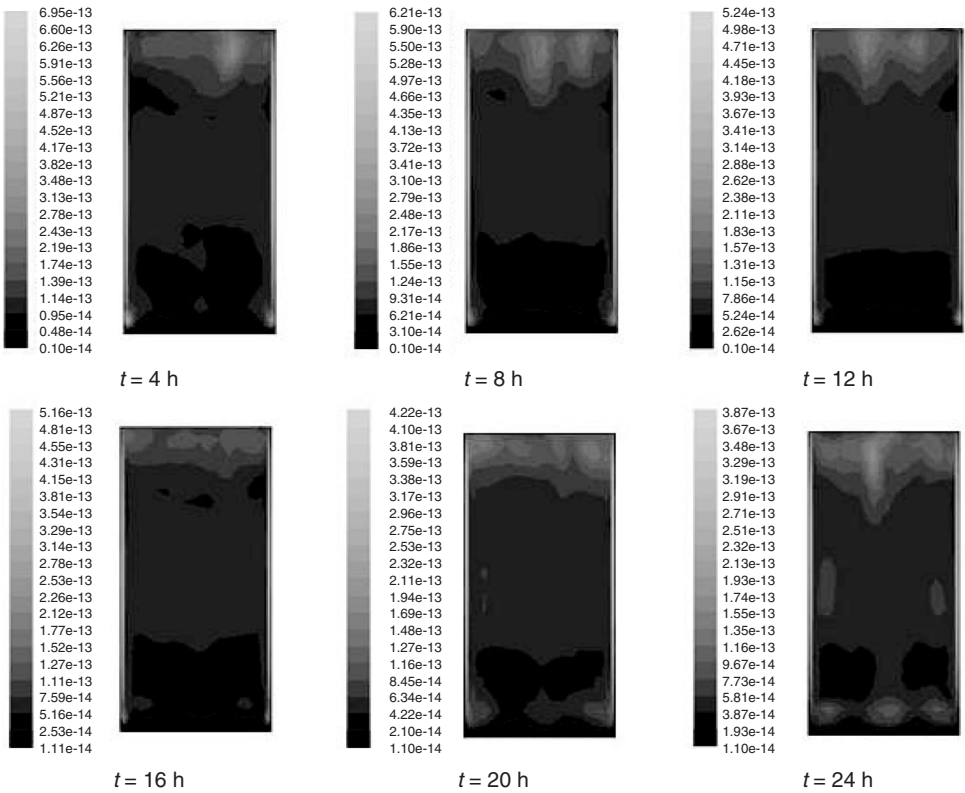


Figure 7.7 Velocity profiles (in m/s) for the storage tank at 4-h intervals

The tank temperature progression over 24 h is obtained with the volume-averaged temperature monitor (see Figure 7.8). A significant loss of temperature is observed over the period because of the lack of insulation surrounding the tank. The temperature decreases sharply at first and the rate of decrease levels off as time progresses. The temperature profile parallels the heat transfer from the tank, with the greatest heat transfer rate at high temperatures due to Newton’s law of cooling. The tank energy storage and thermal energy loss are shown over 24 h in Figure 7.9, while the tank exergy storage and thermal exergy loss are depicted in a similar format in Figure 7.10.

Several points concerning with the differences between energy and exergy values in TES applications can be noted by comparing Figures 7.9 and 7.10:

- First, the exergy storage and thermal exergy loss are much less than the corresponding energy quantities. This is due to the fact that the exergy of a substance is relative to the reference-environment state, and that thermal exergy is much less than thermal energy at near-reference-environment temperatures. In contrast, the energy of the thermal storage is considerable, reflecting incorrectly the usefulness of the TES.
- Second, while the energy storage and heat loss curves are almost linear, the corresponding exergy curves tend to change much more sharply with time. This observation indicates that the usefulness (or exergy content) of the thermal store is much greater at higher temperatures, that is, a high-temperature thermal storage contains much more exergy than a lower temperature storage. Clearly, exergy takes into consideration not only the quantity but also the quality of energy.

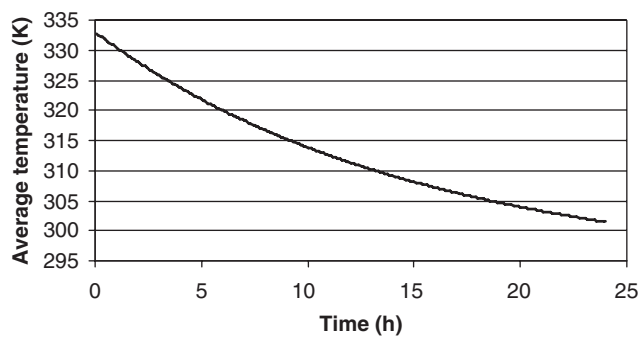


Figure 7.8 Volume-averaged temperature in the storage tank over the 24-h cooling period

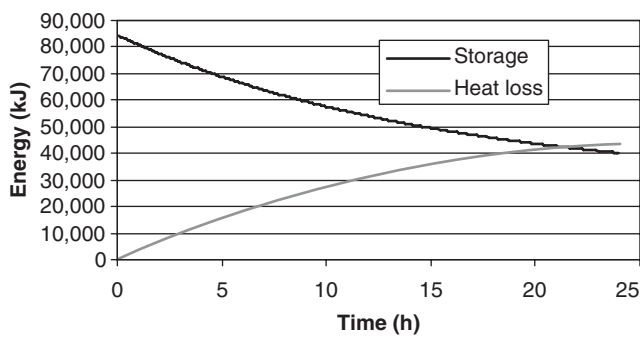


Figure 7.9 Total energy storage and thermal energy loss over the 24-h cooling period

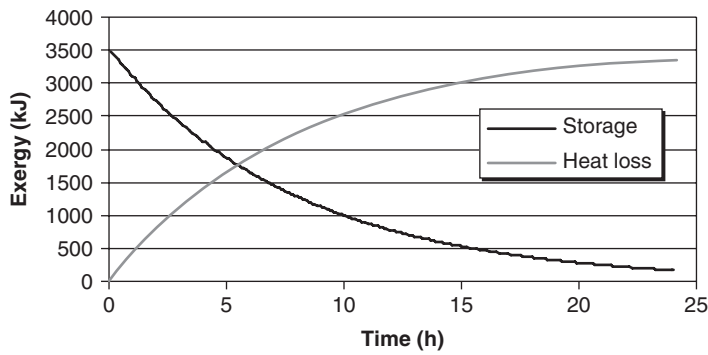


Figure 7.10 Total exergy storage and thermal exergy loss over the 24-h cooling period

These results demonstrate useful aspects of exergy analyses and explain in part why both energy and exergy efficiencies are often sought in evaluating the merit of TES systems.

The efficiencies for this case are shown as a function of time in Figure 7.11. As anticipated, the exergy efficiencies are much lower than the corresponding energy efficiencies, and represent a more realistic view of system performance. If the tank were left to cool for an infinite time, the exergy profile would asymptotically approach a zero efficiency value. However, the energy profile would

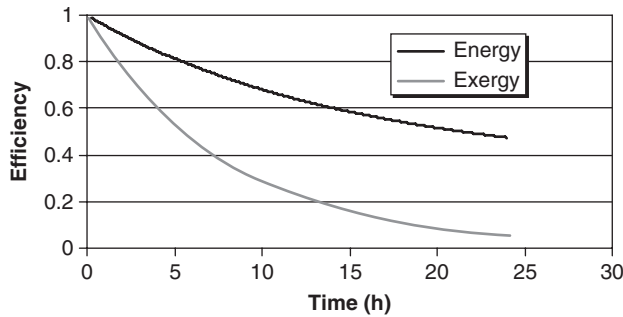


Figure 7.11 Variation with time of the energy and exergy efficiencies of the cooling process

eventually decrease to a value of $mh_{\infty}/E(0)$ or approximately 33.4%. The fact that a completely useless mass of water, with zero heating potential, still retains a recovery efficiency of 33.4% illustrates the inadequacies of using energy alone in TES system assessments and improvement efforts.

Closure for Case Study 1

The cooling is investigated for a large tank of hot water initially at 60 °C as it exchanges heat with its surroundings at 20 °C, via convective heat transfer with a convective coefficient of 10 W/m² K. The average temperature within the tank is monitored as time progresses, so that efficiencies and thermal losses can be recorded.

The process is observed to be highly efficient in both the energy and exergy senses at the beginning of the simulation, since most of the thermal energy or exergy can be recovered. As time progresses and the temperature of the storage tank drops due to heat losses, the efficiencies decrease and less recoverable thermal energy or exergy remains. The energy efficiency is 47.5% after the 24-h cooling period, while the exergy value is 4.79%. The differences between the two efficiencies demonstrate the usefulness of exergy analysis in TES applications: since the TES is at a temperature of just over 23 °C after the 24-h period, it is misleading to deem that the thermal energy is almost half recoverable as the energy efficiency suggests since the quality of the thermal energy is neglected.

This case study is intended to give the reader an understanding of the usefulness of FLUENT in TES applications. Although this particular example is simple and incorporates many assumptions to simplify the modeling and simulation, it provides a good introduction for the more complicated simulations that are investigated in subsequent case studies. These include forced convection and stratification for sensible TES, as well as external flow, solidification, and melting for latent TES.

7.5.2 Case Study 2: Forced Convection in a Stratified Hot Water Tank

This case study is concerned with forced convection in a stratified, hot water storage tank. Whereas the study in the previous section is concerned with the losses due to only natural convection, this example examines the charging of a hot water tank with warm water. The tank considered is cylindrical, with a height of 100 cm and a radius of 15 cm, and is insulated along its walls with fiberglass. The tank is initially at a temperature of 20 °C. A schematic of the system is shown in Figure 7.12. The physical model and variable inputs are chosen to be similar to those in an investigation by Ghaddar and Al-Maarafie (1997). FLUENT is used to investigate the charging process using hot water at 70 °C.

The system is subject to convective heat loss to surroundings at 20 °C, and has a surface convective heat transfer coefficient of 4.5 W/m² K, which is taken to be constant. The inlet velocity

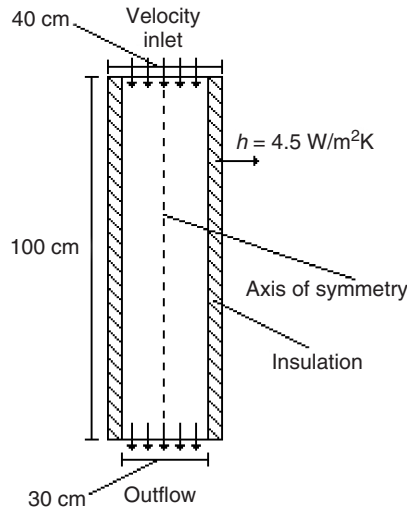


Figure 7.12 Schematic of physical domain of a thermal storage, modified from Ghaddar and Al-Maarafie (1997)

is treated as uniform. The effect of flow rate on the resulting performance criteria is examined by considering two flow rates (9 L/min and 3 L/min). The water is taken to have a density of 998.2 kg/m^3 , a specific heat of 4.182 kJ/kg K , a thermal conductivity of 0.6 W/m K , and a dynamic viscosity of 0.00103 kg/m s . Natural convection is considered negligible. As the Reynolds number for the flow cases considered here is between 200 and 650, which is in the laminar regime, the flows are treated as laminar. The insulation is a common fiberglass type, with a density of 12.0 kg/m^3 , a specific heat of 0.844 kJ/kg K , and a thermal conductivity of 0.04 W/m K (Harris *et al.*, 2003).

The flow is considered to have a no-slip condition on the inner walls of the insulation, which is contained by a steel wall of thickness 3 mm. Although not shown in Figure 7.12, this boundary condition includes a “virtual” wall for simulation purposes; it does not occupy finite space, but still applies a conductive resistance to the heat flow as in a thin wall. The steel in this case is considered to be stainless steel, with a density of 8030 kg/m^3 , specific heat of 0.502 kJ/kg K , and conductivity of 16.27 W/m K , based on FLUENT default values. The specified inlet temperature and velocity corresponding to each flow rate considered, along with the outflow boundary condition (discussed in Section 7.4.3) and convectively cooled tank walls, provide sufficient boundary and initial conditions for the simulation.

The model was created using GAMBIT software, with special attention at the inner walls of the flow regime. The computational domain, separated into finite volumes, can be seen in Figure 7.13. The cell densities on the inner walls of the tank can be seen in Figure 7.13(a) and (b), where longitudinal and cross sections of the volume, respectively, are shown. The top view in Figure 7.13(c) shows the cell distribution and shape of the outer tank wall more clearly. The meshing is developed by first creating a four-layer boundary region on the innermost cylinder, with an initial spacing of 0.5 cm and a growth factor of 1.2. With this boundary layer, the cells for the remainder of the volume, including the insulation, are created with hex/wedge elements in a cooper-type mesh, resulting in a total of 7718 computational volumes.

This physical domain, after specifying the appropriate zone and boundary types, is simulated with FLUENT. The inlet velocity is set to 0.000707 m/s and 0.002121 m/s for the flow rates of 3 L/min and 9 L/min, respectively. Simulations are run for 18 min of real flow time for the slower flow rate and 6 min for the faster, with three data samples of the temperature and velocity fields

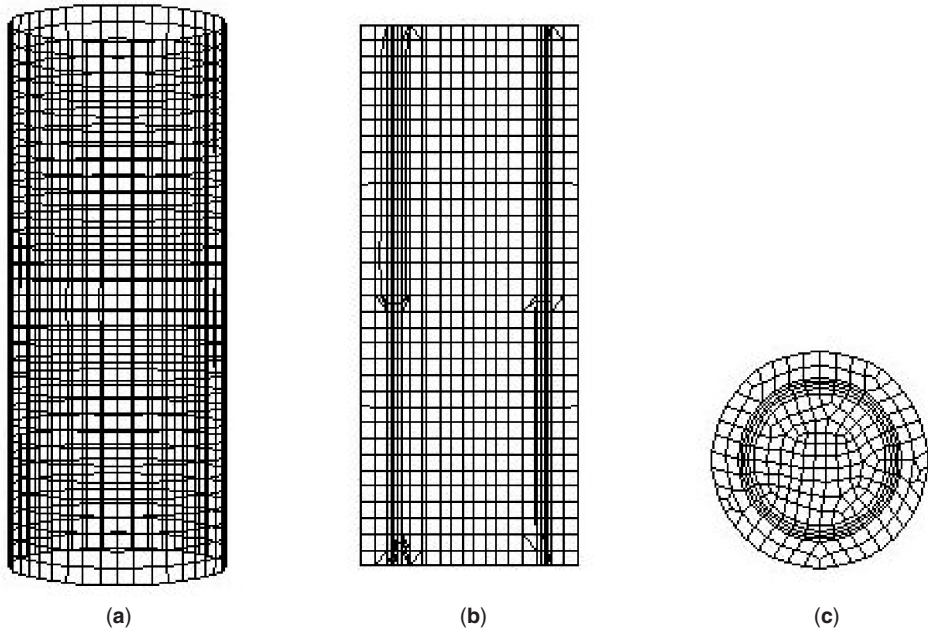


Figure 7.13 Views of the computational grid for the hot water storage in the outer wall section (a), radial cross section (b), and axial cross section (c)

taken at equally spaced intervals in each case. The residual tolerances are set to 10^{-3} for the x , y , and z velocities and continuity and 10^{-6} for energy.

To simulate the efficiency and performance equations correctly, the following quantities are monitored over the duration of the simulation: the outlet mass-weighted average temperature (see Equation 7.21), the volume-weighted water and insulation average temperatures (Equation 7.23), and the surface heat flux from the tank (Equation 7.22). The simulations are run with a time step of 1 s for the slower flow rate and 0.5 s for the faster, while temperature and heat flux data are taken at 5-s intervals. A comparison of the simulation results with experimental results from Ghaddar and Al-Maarafie (1997) shows good agreement. Time step independence is also verified, but the reader should consult the case study in Section 7.7.2 for an illustration of the methodology of independence verification. With the proper monitors in place and the computational domain initialized at 20°C , the simulation is then run with a computational time ratio of about 1:1, so that each simulation concludes in less than 20 min.

Performance Criteria

The energy balance for the tank charging process at time t is as follows:

$$\Delta E_{sys} = \Delta E_{water} + \Delta E_{insulation} = \int_0^t \dot{m}C (T_{in} - \bar{T}_{out}) dt - Q(t) \quad (7.30)$$

where $Q(t)$ is the total heat loss from the system at time t . Since the purpose is hot water storage, the energy product for the energy efficiency is taken to be the change in energy of the water in

the tank. The total required energy is the total flow energy difference in the flow, so the energy efficiency can be expressed as

$$\eta = \frac{E_{prod}}{E_{input}} = \frac{\Delta E_{water}}{\Delta E_{water} + \Delta E_{insulation} + Q(t)} \quad (7.31)$$

The total heat loss is evaluated by approximate integration over n time steps of equal length Δt as

$$Q(t) = \int_0^t Q dt = \sum_{i=0}^n Q_n \Delta t \quad (7.32)$$

Since kinetic and potential energy effects are neglected, the changes in energy in both the water and insulation portions of the domain are evaluated using incompressibility assumptions as

$$\Delta E_{water} = m_{water} C_{water} (\bar{T}_{v,water} - T_{\infty}) \quad (7.33)$$

$$\Delta E_{insulation} = m_{insulation} C_{insulation} (\bar{T}_{v,insulation} - T_{\infty}) \quad (7.34)$$

The ambient temperature in this case is set to 20°C, while the masses of water and insulation are 70.1 kg and 0.66 kg, respectively.

The exergy analysis reflects the losses associated with the mixing of fluids, which is an irreversible process. The exergy balance can be expressed as follows:

$$\Delta \Xi_{sys} = \Delta \Xi_{water} + \Delta \Xi_{insulation} = \epsilon_{in} - \epsilon_{out} - X_I - I \quad (7.35)$$

Before delving into entropy balances, which can be used to calculate the exergy destroyed because of irreversibility I , the exergy efficiency is defined in the same format as used for the energy efficiency. That is, the exergy efficiency is taken to be the ratio of product exergy to the thermal exergy stored in the tank, or the change in exergy in the storage medium, water. The required input exergy content is the difference in exergy from the inlet to outlet, so that

$$\psi = \frac{\Xi_{prod}}{\Xi_{input}} = \frac{\Delta \Xi_{water}}{\Delta \Xi_{water} + \Delta \Xi_{insulation} + X_I(t) + I(t)} \quad (7.36)$$

Here, the exergy change of the system at any time t is once again obtained from the instantaneous volume-averaged temperatures in the respective mediums:

$$\Delta \Xi_{water} = m_{water} C_{water} \left[\bar{T}_{v,water} - T_{\infty} - T_{\infty} \ln \left(\frac{\bar{T}_{v,water}}{T_{\infty}} \right) \right] \quad (7.37)$$

$$\Delta \Xi_{insulation} = m_{insulation} C_{insulation} \left[\bar{T}_{v,insulation} - T_{\infty} - T_{\infty} \ln \left(\frac{\bar{T}_{v,insulation}}{T_{\infty}} \right) \right] \quad (7.38)$$

The exergy loss due to heat leakage is again calculated with an approximated integral, assuming heat leakage takes place at the average temperature of the insulation:

$$X_I(t) = \int_0^t \left(1 - \frac{T_{\infty}}{\bar{T}_{v,insulation}} \right) Q dt = \sum_{i=0}^n \left(1 - \frac{T_{\infty}}{\bar{T}_{v,insulation,i}} \right) Q_i \Delta t \quad (7.39)$$

The remainder of the performance criteria determination is concerned with evaluating the exergy destroyed by irreversibilities. Entropy expressions are used, including an entropy balance at time t :

$$\Delta S_{sys} = \Delta S_{water} + \Delta S_{insulation} = (S_{in} - S_{out})(t) + S_Q(t) + \Pi(t) \quad (7.40)$$

where

$$\Delta S_{water} = m_{water} C_{water} \ln \left(\frac{\bar{T}_{v,water}}{T_{\infty}} \right) \quad (7.41)$$

$$\Delta S_{insulation} = m_{insulation} C_{insulation} \ln \left(\frac{\bar{T}_{v,insulation}}{T_{\infty}} \right) \quad (7.42)$$

$$S_Q(t) = \frac{Q(t)}{\bar{T}_{v,insulation}} \quad (7.43)$$

If the quantity \bar{T}_{out} is measured for the outflow, then the total difference in entropy flow at any time t is as follows:

$$(S_{in} - S_{out})(t) = \int_0^t \dot{m} C_{water} \ln \left(\frac{\bar{T}_{out}(t)}{T_{in}} \right) dt = \sum_{i=0}^n \dot{m} C_{water} \ln \left(\frac{\bar{T}_{out,i}}{T_{in}} \right) \Delta t \quad (7.44)$$

Finally, the exergy destroyed because of irreversibilities is evaluated:

$$I(t) = T_{\infty} \Pi(t) \quad (7.45)$$

and the exergy efficiency can now be determined.

Results and Discussion

FLUENT allows for data sampling of the entire field at any time during the simulation. Here, the temperature and velocity fields are sampled at intervals of 6, 12, and 18 min for the flow rate of 3 L/min, and at intervals of 2, 4, and 6 min for the flow rate of 9 L/min. These sampling rates permit qualitative examinations of the intrinsic nature of the flow and temperature values in the tank. For a lengthwise cross-section of the tank, temperature distributions for the flow rates of 3 L/min and 9 L/min, respectively, can be seen in Figures 7.14 and 7.15, while corresponding velocity distributions are shown in Figures 7.16 and 7.17.

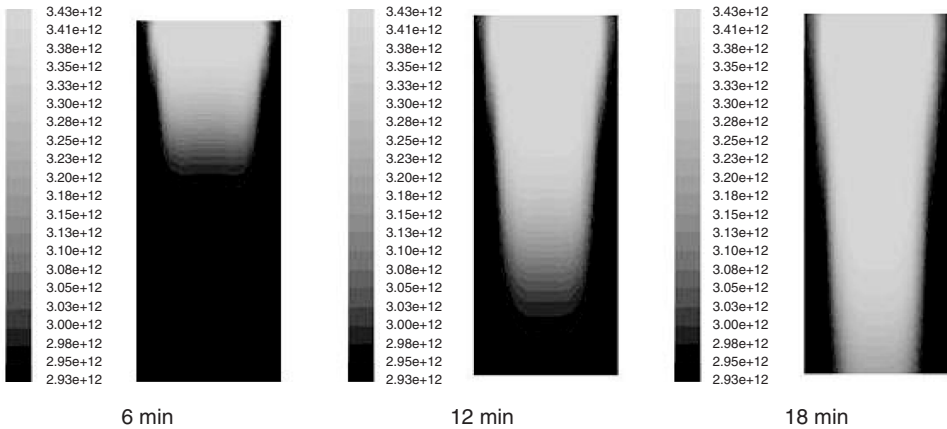


Figure 7.14 Temperature distributions (in K) in a thermal storage tank at selected times for a flow rate of 3 L/min

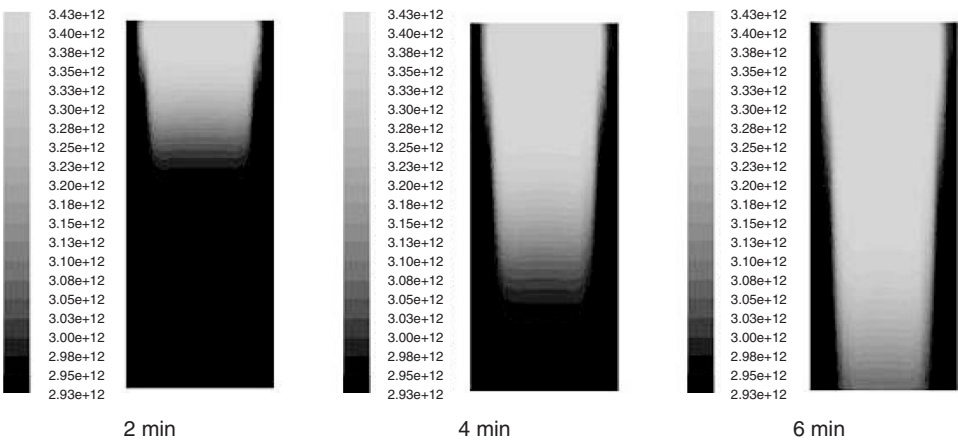


Figure 7.15 Temperature distributions (in K) in a thermal storage tank at selected times for a flow rate of 9 L/min

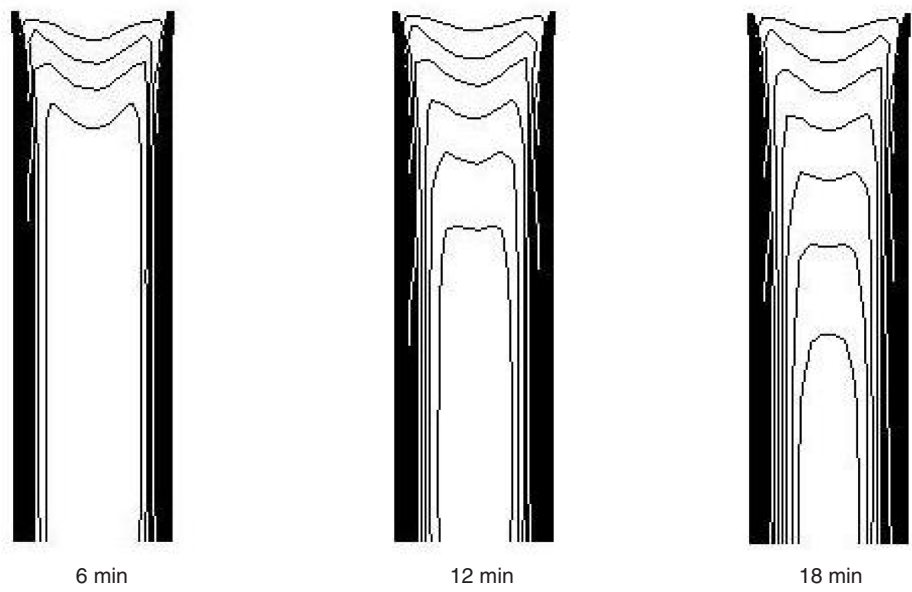


Figure 7.16 Velocity contours in a thermal storage tank at selected times for a flow rate of 3 L/min

The distinct difference in temperature between the insulation and the flowing fluid is clearly evident in the temperature distributions. The insulation hinders the amount of heat transfer to the ambient air, and the dark color in this region, indicating a relatively low temperature, confirms that little heat escapes. As time progresses, however, especially for the slower flow rate case (Figure 7.14), the upper portion of the tank is seen to be losing some heat because of the increasing temperature difference between the ambient air and the warm inner fluid. It is also observed that a thermal boundary layer is developing in the flow and, although this case is not simulated for

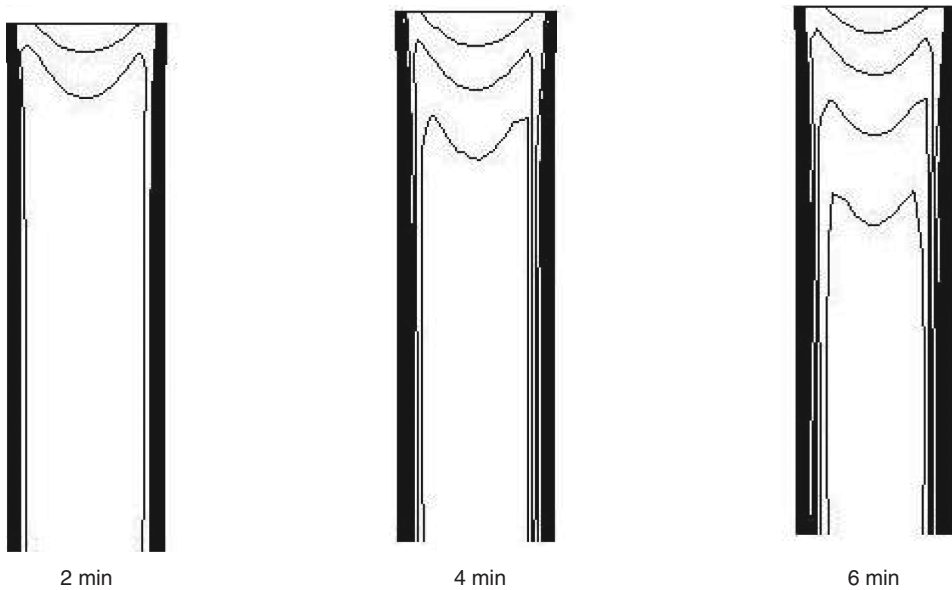


Figure 7.17 Velocity contours in a thermal storage tank at selected times for a flow rate of 9 L/min

steady-state conditions, it is apparent that equilibrium would be reached after sufficient time with respect to thermal and velocity gradients within the computational domain.

The shapes of the temperature contours in Figures 7.14 and 7.15 are also interesting to compare. In the faster moving flow, the temperature contours at the edge of the warm flow appear to be much more sharply differentiated from the cold region. In contrast, the slower flow appears to have more rounded isotherms, mainly because of the fact that more time is available in the case of the slower flow rate for heat from the hot water to diffuse downstream. In both cases, the hot water travels the same distance along the tank, but less heat diffusion clearly occurs in the faster moving case, yielding less rounded isotherms.

The velocity contours also help explain the differences in the temperature profiles for the two flow rates. Since the computational domain is initialized at zero velocity, there is a trend as the fluid traverses the tank for the flow to become fully developed, as seen in Figures 7.16 and 7.17. There, the velocities become more representative of a continuous, fully developed regime as time progresses, and less like plug flow. Consequently, the corresponding isotherms also tend toward fully developed flow.

The types of contour plots shown here, which are easily accessible in FLUENT, help determine whether simulations are achieving good results, and in some cases can indicate problems in modeling and setup. For this reason, it is prudent when performing simulations to intermittently check the pressure, temperature, and flow fields to determine the accuracy or precision of the numerical progression.

After reviewing qualitative aspects of the simulation, the previously outlined performance criteria and their variations with time can be examined, including thermal energy and exergy losses, exergy destruction due to irreversibility, and energy and exergy efficiencies. The variation with time of the overall volume-averaged temperature of the tank and insulation are shown for the two flow rates considered in Figures 7.18 and 7.19. The two temperature profiles appear similar, but for the case with the slower flow rate (3 L/min), the temperature of the insulation is higher. This phenomenon is due to the increased wall conduction and correspondingly reduced heat loss to the surroundings associated with the longer charging time.

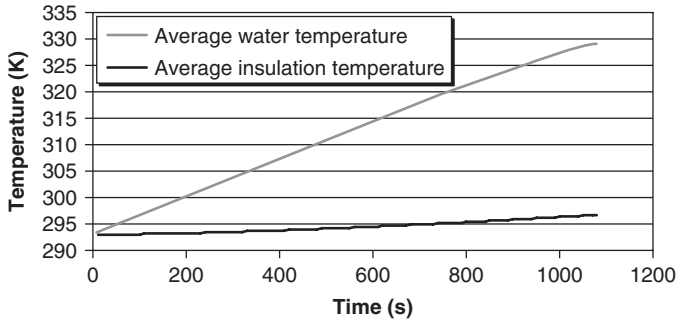


Figure 7.18 Volume-averaged temperatures of the water and insulation for a flow rate of 3 L/min

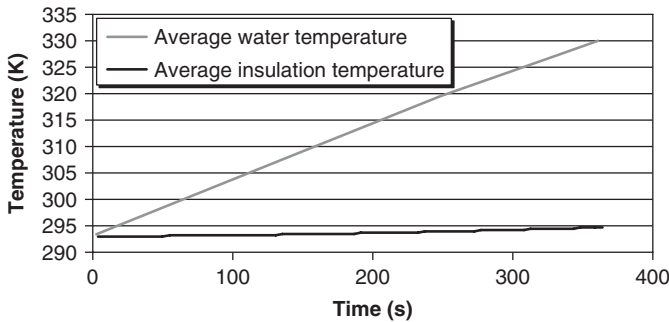


Figure 7.19 Volume-averaged temperatures of the water and insulation for a flow rate of 9 L/min

The two flow rates exhibit similar trends and are compared in the remainder of the analysis by plotting them against a dimensionless time, $t^* = t/t_{\max}$, to better reveal their differences. For the 3 L/min case, $t_{\max} = 1800$ s, and for the case where the flow rate is 9 L/min, $t_{\max} = 360$ s.

The loss of heat to the environment, $Q(t)$, is plotted as a function of the dimensionless time t^* in Figure 7.20 for both flow rate cases. It is clear that the higher flow rate case experiences a greater heat loss, which is almost five times the heat loss of the 3 L/min flow rate case.

The energy efficiencies for both cases are presented in Figure 7.21. The energy efficiencies are very high for both cases, indicating that almost all of the injected heat is recovered. At the conclusion of each simulation, that is, when $t^* = 1$, the energy efficiencies are 99.93% and 99.84% for the flow rates of 9 L/min and 3 L/min, respectively. Furthermore, since the only mode of energy loss is heat leakage, the efficiencies are directly dependent on heat leakage. For the higher flow rate, the energy efficiency is higher since less heat leaks to the surroundings.

The energy efficiencies do not reflect the thermodynamic performance properly, and a more comprehensive view is provided when exergy considerations are taken into account. The exergy loss to the surroundings via heat loss is shown in Figure 7.22. A comparison of this figure with Figure 7.20 shows that the absolute magnitudes of the thermal energy and exergy losses differ greatly, with the heat leakage varying between 5 and 30 J, while the corresponding exergy values of these heat leakages are relatively insignificant (less than one-hundredth of a joule in all cases). These values indicate that the tank is well insulated, and are not a large factor in performance calculations. The thermal exergy loss is small because the heat loss occurs at a temperature near that of the reference environment. The exergy associated with the heat loss depends on the temperature

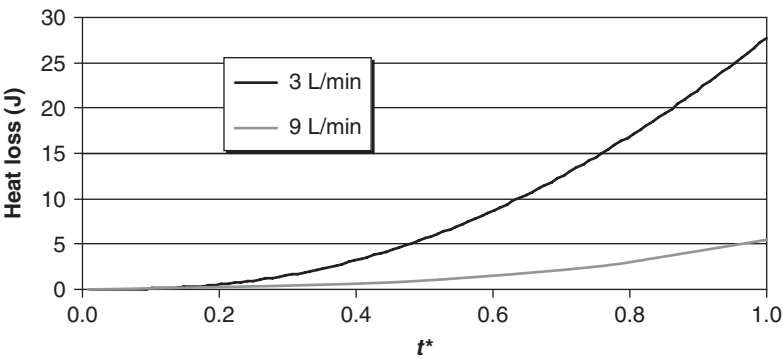


Figure 7.20 Loss of thermal energy from the storage to the surroundings, for the two flow rates

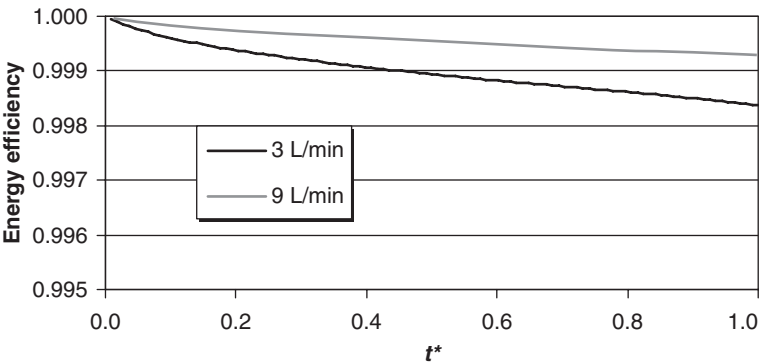


Figure 7.21 Energy efficiencies of the storage, for the two flow rates

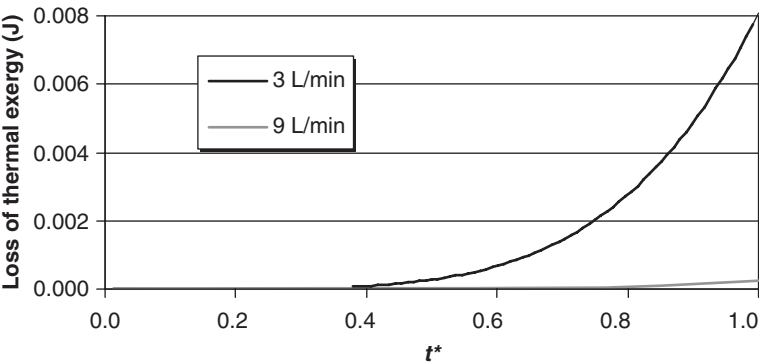


Figure 7.22 Exergy lost from the storage to the surroundings owing to heat leakage, for the two flow rates

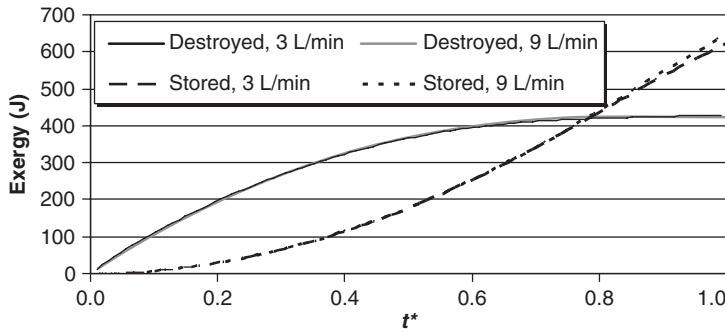


Figure 7.23 Exergy destruction in the storage due to irreversibilities and exergy of the stored hot water, for two flow rates

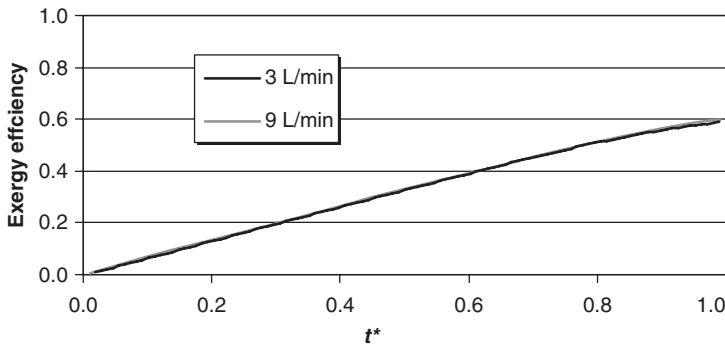


Figure 7.24 Exergy efficiencies of the storage, for the two flow rates

ratio of heat loss to the reference environment in such a manner that these temperatures render the thermal exergy loss very small, especially in comparison to the overall thermal exergy of the tank.

The other component of the exergy loss, the destroyed exergy, is displayed in Figure 7.23. Also shown is the exergy of the stored hot water. This loss provides a much more perceptive picture of the overall performance of the charging process, since the destroyed and stored exergies both significantly affect the exergy efficiency. The exergy destroyed because of irreversibilities is much greater than the thermal exergy loss and is the main contributing factor to the exergy efficiency values (see Figure 7.24), which are approximately 60% at the conclusion of the simulation for both flow rate cases. The exergy efficiencies are clearly significantly lower than the energy efficiencies.

The exergy efficiencies are lower largely as a result of the recoverable thermal exergy. Near the beginning of the simulation, the overall water tank temperature is low and it can be shown with Equation 7.18 to have little exergy (see Figure 7.23). As the volume-weighted temperature of the tank increases, its recoverable exergy content becomes greater. Since the thermal energy input to the tank is of a much higher quality because of its relatively high temperature, the ratio of recovered to input exergy is initially almost zero and increases as the tank charges. However, it is apparent in Figure 7.23 that the increase in exergy destruction with time levels off after a period of time. This observation is mainly attributable to the fact that the outlet temperature increases with time, so less mixing with the colder fluid occurs. When the outlet temperature rises, the exergy difference between inlet and outlet drops sharply, so less of the quality of the charging fluid is wasted. The exergy efficiency consequently levels off also, as can be partly seen in Figure 7.24.

The result comparisons also reveal a similarity between the efficiencies of the two flow rates considered. The energy efficiencies, although of high magnitude, exhibit discernable differences, as seen in the profiles for the two flow rates. However, the exergy efficiencies are more similar. This observation reinforces the point made earlier that thermal leakage, which differs greatly for the two cases, does not affect exergy efficiency markedly. For both cases, heat leakage and the energy stored in the insulation are unimportant, and it is the exergy destruction (due to entropy generation) that affects performance significantly. The two storage cases are equally efficient at charging the thermal store.

Finally, it is noted that the results demonstrate that energy analysis creates confusion regarding the performance of this TES system. While energy analysis suggests to engineers that the process is nearly ideal, the exergy efficiencies indicate that this is not the case, and that there exists a significant margin for efficiency improvement. This important observation recurs in subsequent case studies.

Closure for Case Study 2

In this sensible TES case study, the charging of an insulated, stratified hot water tank with forced convection is investigated. The tank considered contains around 72 L of water initially at the ambient temperature of 20 °C, and is charged using hot water at 70 °C. Heat loss to the surroundings is accounted for. Two flow rates (3 and 9 L/min) are considered, and the simulated charging times for the two cases are 18 min and 6 min, respectively. To facilitate performance calculations, average temperatures in the water and insulation regions are monitored, as are the total heat loss through the outer tank walls and the mass-weighted outlet temperature.

The main simulation results demonstrate that the energy and exergy efficiencies exhibit different trends. The energy efficiency of the process begins at 100% and gradually decreases over the course of the simulation to 99.9%, while the exergy efficiency begins at 0% and increases with time to a final value of approximately 60%. This result suggests that a thorough charging of hot water tanks provides one means of avoiding loss of energy quality. The energy and exergy losses due to heat leakage to the environment are found to affect performance values relatively insignificantly.

Although this sensible TES case study is more complex than the first in terms of thermodynamic analysis, the simulation of similar sensible TES processes is relatively straightforward. The ease of numerical solution has a cost – the need to understand the volume and surface monitors available (many of which are either not mentioned or addressed in Section 7.6.3) sufficiently well so that they can be used to achieve proper results.

7.5.3 General Discussion of Sensible TES Case Studies

The case studies in this section help illustrate the usefulness of FLUENT and, more generally, finite volume solvers. While the modeling and simulation algorithms are complex, commercially available software for TES purposes provides ease of use. Complex fluid flow problems coupled with heat transfer phenomena can be straightforwardly investigated.

In the first case study, natural convection is modeled in a large storage tank, with heat leakage via natural convection. The simulation results confirm the contribution of insulation to efficiency. Similarly, forced convection is modeled in the second case study for an insulated storage. The results show that the heat leakage to the surroundings detracts less from efficiency than internal irreversibilities. In both cases, energy efficiencies are misleadingly high, and second-law considerations need to be taken into account to better understand performance and efficiency.

The case studies presented provide a good introduction to the latent TES cases considered subsequently. Most latent TES systems involve some sensible heat interactions, for example, in a heat transfer fluid (HTF). In addition, to extract energy from a latent store like a PCM, temperature changes in the liquid or solid phases sometimes occur, and sensible considerations must be

accounted for. The main objective of the following section is to build upon the material introduced in this section and thereby explain how more complicated cases may be simulated using FLUENT. However, since many of the modeling, simulation, and analysis techniques are similar, repetition is avoided in the next section and only pertinent information provided.

7.6 Numerical Modeling, Simulation, and Analysis of Latent TES Systems

The modeling and simulation of latent TES systems is addressed in this section. Latent TES systems are finding increasing applications because of their high volumetric heat capacities. However, compared to sensible TES systems, which are usually water based, latent TES systems can be subject to more implementation difficulties. These include finding a material with a suitably high heat of fusion and a melting point near the desired temperature, and that is relatively benign and reliable, so that successive charging and discharging cycles can be carried out without replacement of equipment. Since solidification or melting occurs for a given storage material at a specified temperature and pressure, care must be exercised to ensure that proper conditions are in place for effective phase change, which is most desirable at the heat utilization temperature of the application.

Building on the modeling, simulation, and analysis of sensible TES systems in previous sections, much of the following material avoids unnecessary repetition. Nonetheless, several models and equations need to be introduced to permit the case studies to be studied properly. These include the volume of fluid (VOF) model, the solidification/melting model, and various ancillary equations for heat transfer and thermodynamic analysis. This treatment is intended to provide the reader with a good understanding of the modeling and simulation of latent TES systems and to facilitate practical and accurate representations of real scenarios.

7.6.1 Modeling

The modeling of latent TES systems does not differ greatly from the modeling of sensible systems, as explained in Section 7.4.1. The computational domains and grid meshing procedures are analogous to the material explained in the previous modeling section. In some cases, moving-grid schemes can be used for more accurate simulations, thereby allowing solid/liquid interfaces to contain a greater concentration of cells. However, the scope of this chapter allows only some options to be explained.

Throughout the analysis, the same principles as in Section 7.4.1 are applied. It is generally advantageous to place more cells (volumes) in areas where phase change is expected to occur. This practice is addressed in subsequent case studies.

7.6.2 Heat Transfer and Fluid Flow Analysis

The phase change that occurs in latent TES leads to slight differences in the heat transfer and energy equations used in the computational domain. For those volumes in liquid phase, however, the same expressions from Section 7.4.2 apply, for example, Navier–Stokes and continuity equations. The Boussinesq model for natural convection is not to be used because of the complexities it introduces, which greatly lengthens modeling, setup, and computational times. For example, Assis *et al.* (2007) investigated melting in a spherical enclosure with FLUENT, accounting for density changes from phase change and natural convective currents. The computational time ratio in this case is over 300:1, even with a markedly more powerful computer than the one used in these case studies. The resulting simulations can require several days, while the models used in this treatment have simulation durations of only a few hours, with little loss in result accuracy or validity. With FLUENT, modeling natural convection and density differences in phase change in an enclosed

volume requires knowledge of C+ programming to implement special user-defined functions in each phase. A detailed explanation of the implementation of C+ scripts into FLUENT is beyond the scope of this book, but is needed for assessments of natural convection.

As mentioned earlier, the continuity and momentum equations in Equations 7.4 and 7.5 are valid in the fluid regions. However, the energy balance in Equation 7.1 is modified to account for energy absorption during phase change. Utilizing a modified enthalpy, the energy equation can be written as follows:

$$\frac{\partial}{\partial t} (\rho h' - p) + \nabla \cdot (\vec{V} \rho h') = k \nabla^2 T + \Phi \quad (7.46)$$

where h' denotes a combined specific enthalpy, which is the sum of two contributions: the sensible enthalpy h and the latent enthalpy h_{latent} . That is,

$$h' = h + h_{latent} \quad (7.47)$$

The sensible enthalpy is calculated with Equation 7.3, and FLUENT uses the enthalpy/porosity method (Voller, 1987; Voller and Prakash, 1987; Voller *et al.*, 1987) to calculate the latent portion. In lieu of a solver that produces a specific melt interface position, this method is often chosen to solve problems with more complex geometries. Instead of tracking the solid/liquid interface position explicitly, the “liquid fraction,” that is, the fraction of the cell in liquid form, is determined. The liquid fraction φ is calculated as

$$\varphi = \frac{T - T_{solid}}{T_{melt} - T_{solid}} \quad (7.48)$$

where T_{solid} denotes the solidification temperature and T_{melt} the melting temperature. The liquid fraction is determined during each iteration to correctly define the temperature field and energy balance. The liquid fraction varies between $\varphi = 0$ when $T < T_{solid}$ and $\varphi = 1$ when $T > T_{melt}$. Cells with a liquid fraction between 0 and 1 have a temperature of $T_{solid} < T < T_{melt}$ and it is only when a cell has a temperature between T_{solid} and T_{melt} that the liquid fraction in Equation 7.48 is calculated.

The latent enthalpy can be written in terms of the latent heat of the material L and the liquid fraction φ :

$$h_{latent} = \varphi L \quad (7.49)$$

Once a cell has received or released all of its latent heat, it cools or warms in a sensible manner as either a solid or a liquid, depending on the process. Equations 7.46 through 7.49, when combined with the sensible enthalpy (Equation 7.3), allow the liquid fractions in all cells, and the temperature and latent energy absorbed in the entire domain, to be calculated.

Note that for the solidification and melting modeling used in FLUENT, there exists a “mushy” zone, which refers to the portion of the domain with a liquid fraction between 0 and 1. This zone is treated as a porous medium, creating a momentum sink. However, due to the lack of forced convection over solidifying or melting regions and the lack of natural convective currents, this momentum sink becomes negligible, and is consequently usually omitted from the momentum equations. For most cases, the solidification and melting temperatures can be set to be equal to facilitate computations and avoid the dampening effects of the mushy zone.

The VOF model also plays an important role. This model permits two or more fluids to be treated by specifying the interface and patching each phase once the domain has been initialized. This approach is important for phase change in an enclosed space, where compressible air is often present with a PCM, to allow for expansion. In the VOF model, the momentum equations are satisfied for the two fluids, and a quantity called the *volume fraction* is computed in each cell for each iteration. The volume fraction ranges from 0 to 1 for each fluid, where a volume fraction of 0 indicates that the cell is void of the fluid and 1 indicates that the cell contains only the fluid.

A volume fraction between 0 and 1 indicates that the cell contains an interface between the fluid and another substance. The momentum and energy equations can be chosen based solely on the volume fraction of each cell, allowing the simulation to proceed. While the VOF model is suitable for predicting phase change in the presence of a compressible gas, it involves some computational challenges, as shown for the case study in Section 7.7.1.

The models presented here, with the accompanying modifications to the heat transfer and fluid flow equations, allow latent TES systems to be well represented for simulation. Before applying these models in the case studies, changes in both simulation and thermodynamic analyses are described.

7.6.3 Simulation

For simplicity, the SIMPLE algorithm (Section 7.4.3) is utilized in the subsequent case studies. Although a pressure-based solver is not always the best choice when a simulation is concerned with density changes and natural convection during phase change, it nonetheless provides reasonable convergence characteristics for the cases considered.

7.6.4 Thermodynamic Analysis

The thermodynamic assessment discussed in Section 7.4.4 applies to latent TES systems, but with a few minor differences in the energy and entropy expressions to account for solidification and melting. The enthalpy change of a material as it undergoes phase change is expressible as

$$\Delta H = \pm mL \quad (7.50)$$

where the positive sign is associated with melting and the negative sign with solidification.

The entropy change during phase change can be expressed as

$$\Delta S = \frac{\Delta Q}{T_b} \quad (7.51)$$

where the subscript b denotes the boundary at which the heat transfer occurs. For a substance undergoing phase change with heat transfer with its surroundings at a temperature of T_{sf} , normally taken as the solidification temperature, the change in entropy can be written as

$$\Delta S = \frac{\pm mL}{T_{sf}} \quad (7.52)$$

To calculate entropy changes, which facilitate the evaluation of entropy and exergy balances, the heat added and the temperatures of the substances need to be known. In some cases, there are changes in the densities of the mediums due to phase change. To evaluate entropy changes in the system in such instances, the mass-weighted average temperature is used:

$$\bar{T}_m = \frac{\sum_{i=1}^n T_i \rho_i |V_i|}{\sum_{i=1}^n \rho_i |V_i|} \quad (7.53)$$

This parameter is similar to the volume-weighted quantity in Equation 7.23. Furthermore, an additional monitor is put in place to observe the heat dissipation from viscous sources. Hence, the

mass-weighted total pressures at the inlet and outlet are monitored:

$$\bar{p}_{out} = \frac{\sum_{i=1}^n p_i \rho_i \left| \vec{V}_i \cdot \vec{A}_i \right|}{\sum_{i=1}^n p_i \left| \vec{V}_i \cdot \vec{A}_i \right|} \quad (7.54)$$

With this parameter, changes in pressure can be translated to head generation from pressure.

7.7 Case Studies for Latent TES Systems

To build on the latent TES case studies in Section 7.5, two cases involving latent TES systems are examined here. The first case considers the melting of a PCM in an infinitely long cylinder, using a two-dimensional mesh representing the cross-section of such a cylinder. The second case considers melting and solidification in a spherical shell exposed to an external heat transfer fluid flow, and represents a more comprehensive analysis.

The first case demonstrates ways of using the VOF model. Since the PCM is modeled as in contact with a compressible gas, the density differences accompanying phase change are considered, and the sinking of the solid in the melting regime is observed. This particular case is computationally demanding, resulting in an extremely high computational time ratio. Although using the VOF model can help achieve more accurate results, especially when modeled with natural convective currents in the PCM volume, the second case study shows that simplifying assumptions can greatly reduce simulation time while retaining good results.

The second case study considers air as the heat transfer fluid that heats paraffin wax until it completely melts. The wax then cools until it completely solidifies. The model is subject to a complete validation and independence testing phase, after which it is considered accurate for similar simulations. This case presents a culmination of the first four case studies in this chapter, and serves as an example of proper comprehensive modeling and simulation using FLUENT of either latent or sensible TES systems.

Through these case studies and the techniques explained through them, the reader should be able to construct, model, and simulate various sensible and latent TES systems. As with any experiment or simulation, the main objective is to obtain useful results and to present them informatively. It is also demonstrated that simulation, while important, also requires sound analysis and interpretation of numerical data in order to achieve meaningful results.

7.7.1 Case Study 1: Two-Dimensional Study of the Melting Process in an Infinite Cylindrical Tube

This first latent TES case involves the melting process in a horizontal cylindrical duct. PCMs are often contained in cylindrical tubes because of the ease of manufacturing such enclosures as well as their ability to accommodate pressure changes induced by expansion or contraction of the PCM during phase change. A simplified approach is adopted in this case in which the tube is treated as infinitely long, resulting in a two-dimensional simulation.

The PCM is a paraffin blend, RT27, supplied by Rubitherm GmbH. Applications of RT27 in hot latent storage applications and experiments have been reported in the literature, for example, Assis *et al.* (2007). The paraffin fills 85% of the volume, while the VOF model (see Section 7.6.2) is used to account for the remaining 15%, which is filled with compressible air, acting as an ideal gas.

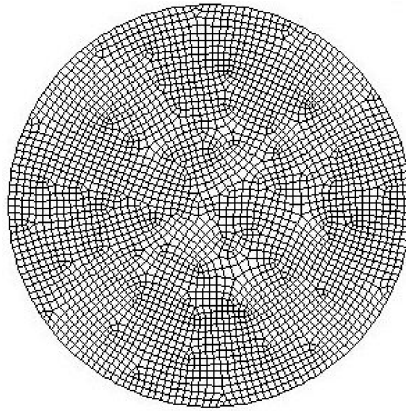


Figure 7.25 Grid structure of the two-dimensional surface representing the infinite cylinder

Throughout the analysis, a two-dimensional cross section of the cylindrical duct of unit depth is considered. The cylinder has a diameter of 20 mm, and the volume can be created straightforwardly using GAMBIT software. The circular shape is constructed first, and then meshed with quadrilateral elements, in a paved meshing. The volume is discretized into 2890 cells, as shown in Figure 7.25. Since the melting front is not known *a priori*, no boundary layer meshings are created; consequently, the equations involving the melt front have equal accuracy, regardless of its position. Once the proper boundary (wall) condition and interior zones are identified, they are input to FLUENT for simulation.

The volume is assigned simple initial and boundary conditions to reduce the computational cost involving density changes with the VOF model. The entire volume, including both the PCM and air regions, is set initially to the ambient temperature of 25 °C (298 K). Then, a constant wall temperature boundary condition of 50 °C (333 K) is invoked to induce melting. This constant wall temperature is not intended to be a condition experienced in real scenarios, but rather is a simple boundary condition that allows for simpler calculations and thus permits the phase change process to be studied qualitatively. The small diameter of 20 mm is chosen to further reduce computational times, since the surface area to volume ratio decreases markedly as the diameter of the cylinder is decreased. Consequently, heat transfer from the cylinder increases, reducing the time required for complete melting of the PCM.

The solidification/melting model is enabled, as is the VOF model, to ensure that proper equations for phase change are used in the domain. Once initial and boundary conditions are set, the PCM is patched to the lower region to model the equilibrium initial state. A density contour diagram is presented in Figure 7.26, which shows the interface position of the PCM and air regions.

The PCM has a melting temperature of 30 °C and a solidification temperature of 28 °C. Many of the thermophysical properties are not held constant, but instead are considered to vary linearly between the two temperatures experienced during phase transition, to increase simulation accuracy. In the solid and liquid phases, respectively, the specific heats are taken to be 2.4 kJ/kg K and 1.89 kJ/kg K and the thermal conductivities 0.24 W/m K and 0.15 W/m K. The solid density is 870 kg/m³ and the liquid density is 760 kg/m³. The decrease in density during melting indicates that expansion occurs during the process. In addition, the dynamic viscosity of the liquid is taken to be 0.0032 kg/m s. All thermophysical properties used here are taken from Assis *et al.* (2007). Air is modeled as an ideal gas, for which properties are obtained using FLUENT's built-in thermophysical properties.

With material properties and boundary conditions established, the melting progression is simulated using a time step of 0.005 s. Larger time steps can be shown in this case to result in a

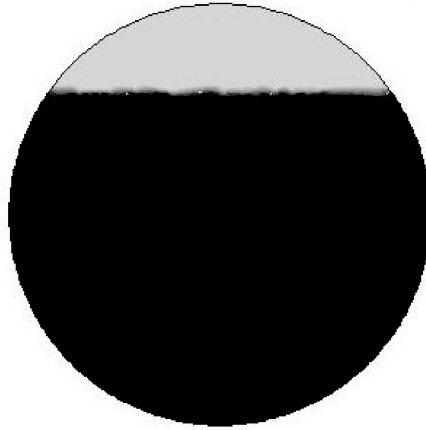


Figure 7.26 Variation in density in the cylinder at time $t = 0$. The darker region represents the PCM and the lighter region above it represents air

diverging residual error, indicating the complexity of using the VOF model in conjunction with solidification/melting. To properly calculate the performance criteria, the heat flux to the region is monitored on an integral basis to determine the total heat addition to the volume as time progresses. To monitor quantitatively the solidification process, the liquid fraction is also monitored on a volume-averaged basis, and the mass-weighted temperature of the entire region is tracked to facilitate entropy calculations. All monitors sample at 1-s intervals throughout the melting process.

The residuals are set to default values of 10^{-3} for the x , y , and z velocities and continuity, and 10^{-6} for energy. The total time to simulate the melting process is considerable; although the real time for the simulation was 173 s, the computational time required was over 4 h. These data indicate a computational time ratio of around 80:1. This result explains why a smaller volume is chosen for assessment here and demonstrates the increase in computational cost when changes in density are considered.

Performance Criteria

With the data obtained from the monitors, the melting process can be evaluated on a thermodynamic basis. Energy, entropy, and exergy balances and efficiencies are presented and discussed.

The only energy input to the control volume is the heat added through the constant-temperature wall, so the energy balance can be written as

$$\Delta E_{sys} = Q_w \quad (7.55)$$

The energy efficiency is defined as the ratio of the energy stored in the volume, that is, the change in energy of the system, to the total input energy. Since no heat is assumed lost to the surroundings, the energy efficiency is

$$\eta = \frac{E_{prod}}{E_{input}} = \frac{\Delta E_{sys}}{Q_w} = 1 \quad (7.56)$$

The 100% energy efficiency is somewhat artificial because of the assumption regarding heat loss. For this system, all heat delivered to the PCM and used for melting is available for recovery on PCM solidification.

The exergy balance more effectively describes the behavior of this system. At any time t during the simulation, the exergy balance can be written as

$$\Delta \Xi_{sys} = X_w - I \quad (7.57)$$

where $\Delta \Xi_{sys}$ denotes the change in exergy of the system, X_w the wall exergy addition associated with heat transfer, and I the exergy destroyed. Hence, we can examine the exergy efficiency progression during the melting process.

The total exergy transferred to the system via the heated wall over n sampling time periods of 1 s each from the start of the simulation to time t can be approximated as follows:

$$X_w = \int_0^t \left(1 - \frac{T_\infty}{T_w}\right) Q_w dt = \sum_{i=0}^t \left(1 - \frac{T_\infty}{T_w}\right) Q_{w,t} \quad (7.58)$$

Since the exergy destroyed due to irreversibilities is given by the relation

$$I = T_\infty \Pi \quad (7.59)$$

the exergy efficiency can be determined using the total entropy generated from the start of the simulation to time t , which can be obtained with an entropy balance:

$$\Delta S_{sys} = \frac{Q_w}{T_w} + \Pi \quad (7.60)$$

The entropy addition to the system by the heated wall is approximated using the sampled data from the monitors:

$$\frac{Q_w}{T_w} = \sum_{i=0}^n \frac{Q_{w,t}}{T_w} \quad (7.61)$$

The change in entropy of the system must account for the change in phase and a change in density in both regions. For an internally reversible process, the change in entropy can be evaluated as an integral of the ratio of heat transferred to the temperature of the heat transfer:

$$S_2 - S_1 = \left(\int_1^2 \frac{\delta Q}{T} \right)_{int, rev} \quad (7.62)$$

If the PCM/air region is assumed to receive heat at its average temperature, the change in entropy of the system at time t can be written as the incremental heat additions to the region divided by the mass-weighted temperature at which these incremental heat additions occur, that is,

$$\Delta S_{sys} = \int_0^t \frac{Q_w}{\bar{T}_m} = \sum_{i=0}^t \frac{Q_{w,t}}{\bar{T}_{m,t}} \quad (7.63)$$

The exergy efficiency is defined as the ratio of product to total input exergy, where the product exergy is the change in exergy of the system and the total input exergy is the exergy transferred to the system from the wall:

$$\eta = \frac{\Xi_{prod}}{\Xi_{input}} = \frac{\Delta \Xi_{sys}}{X_w} = \frac{\Delta \Xi_{sys}}{\Delta \Xi_{sys} + I} \quad (7.64)$$

Results and Discussion

Using the visualization tools in FLUENT, the liquid and solid fractions can be viewed as time progresses (see Figure 7.27). It is clear that the solid gradually decreases in size and sinks as time progresses. Additionally, at the later stages of melting, the solid region takes on an unexpected shape from what is conventional in solidification problems. This shape is attributable to the omission of natural convection in the simulation. Currents in this case are based solely on the sinking solid PCM and very little motion occurs in the fluid regions as melting progresses. Since heat transfer occurs at the surface, the static liquid PCM region tends to act as an insulator to the melt front, causing the center region to melt less quickly than would be the case in a real scenario. It is not until the mushy zone is completely melted, between 120 and 165 s, that the solid region sinks to the bottom of the domain as expected.

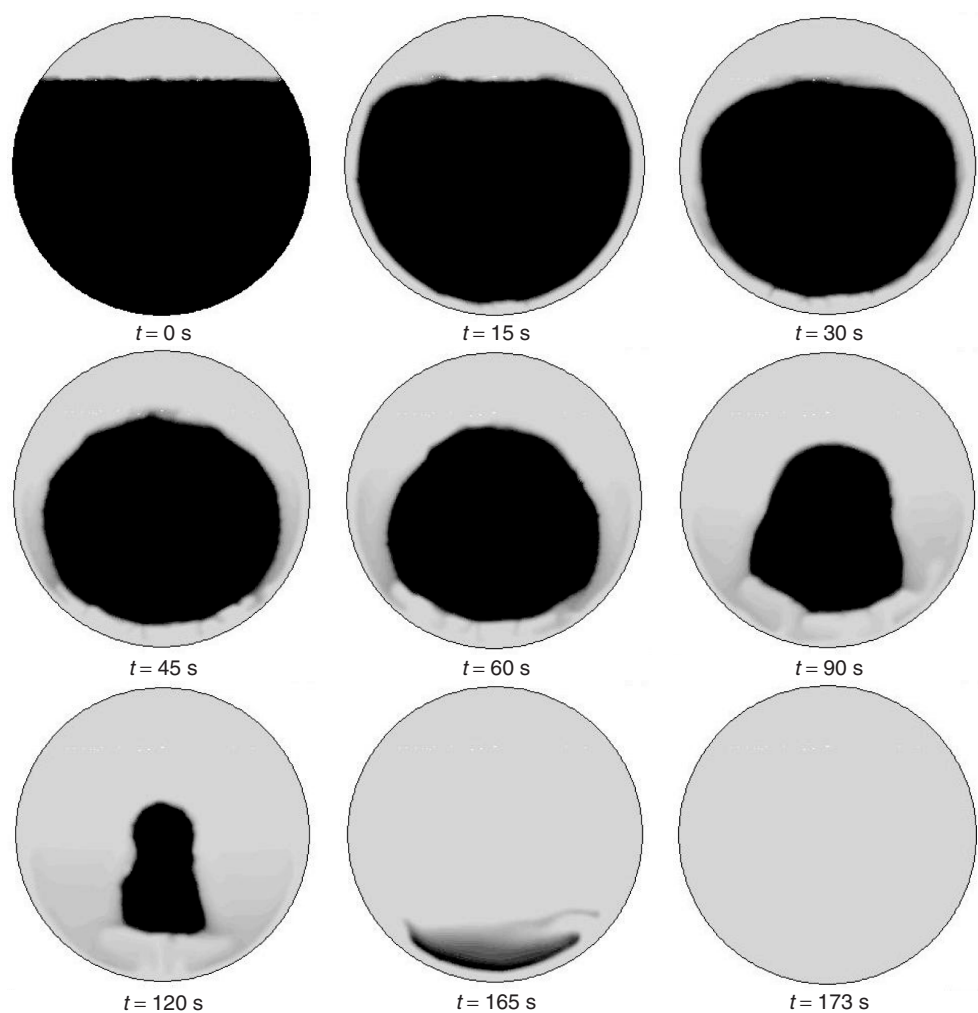


Figure 7.27 Liquid and solid fractions in the storage domain at selected time intervals during melting. The darker image represents the solid material

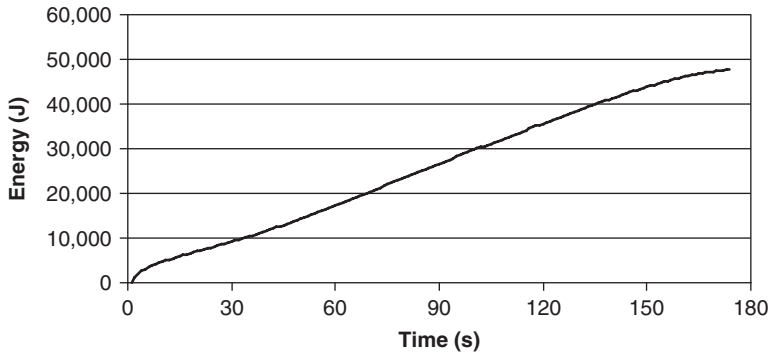


Figure 7.28 Total energy transferred to the cylinder from the heated wall over time

Although the liquid/solid front exhibited in Figure 7.27 is only approximated in this case, the thermodynamic performance presented provides an understanding of the efficiency of melting processes using a high-temperature source.

The total heat transferred to the cylinder as time progresses is shown in Figure 7.28. As expected, the heat transfer from the wall increases sharply at first and then shifts to a nearly linear pattern. The initial heat addition is large at the beginning of the simulation because of the large temperature gradients, which become smaller as time progresses. The almost linear nature of the curve in Figure 7.28 indicates that the temperature gradients are somewhat constant in the cylinder, and suggests that the sinking motion of the PCM allows for some convection. The heat transfer in the domain is enhanced by considering the change in density, and mirrors the behavior of models with natural convection considered in the liquid portion of the PCM.

With energy analysis, the efficiency of the system is determined to be 100%, since all of the heat added to the system is recoverable. This value is not indicative of the actual thermodynamic behavior of the system, and exergy analysis provides a more perceptive assessment. The exergy efficiency of the system as time progresses is shown in Figure 7.29, along with the liquid fraction. The most significant difference between the exergy and energy efficiencies is magnitude. Whereas the energy efficiency is 100% at all times, the exergy efficiency is initially zero and gradually

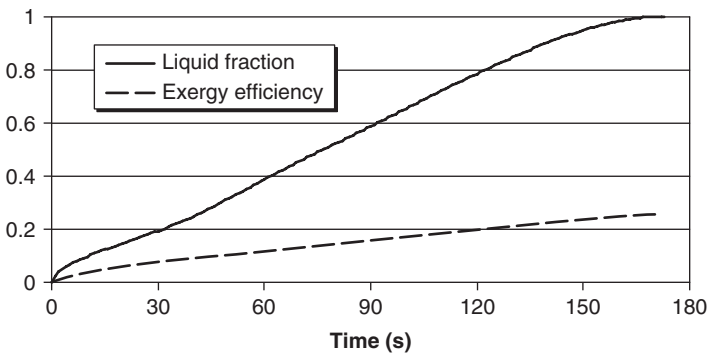


Figure 7.29 Exergy efficiency and liquid fraction of the melting process with time for the cylindrical storage

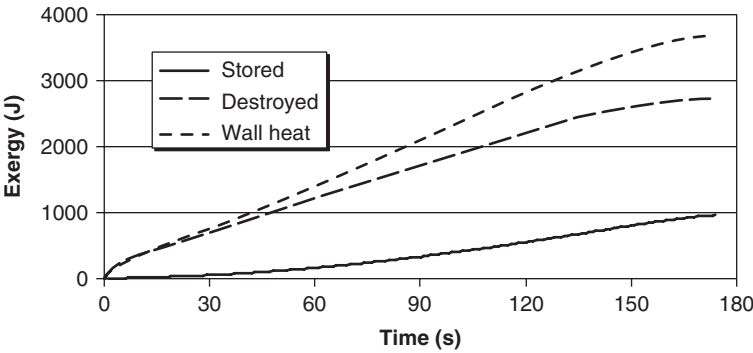


Figure 7.30 Quantities of exergy stored, destroyed, and input with wall heat for the cylindrical storage

increases to 26% at the end of the 173-s simulation period. The result indicates that the heat addition is most efficient when the PCM temperature is hottest and least efficient when relatively high-temperature heat is added to a lower temperature medium. The change in exergy of the entire system is small at the initial stages of the simulation due to the low temperature (near-ambient conditions) in the cylinder, and the exergy added with wall heat is large in comparison. When the temperature of the thermal storage PCM rises appreciably, the difference between its temperature and that associated with the wall heat becomes smaller, and the efficiency increases.

Figure 7.30 depicts the stored and destroyed exergy as well as the exergy addition by wall heat. It can be seen in that figure that the stored exergy does not increase significantly until the later stages of melting. Also, the stored exergy is the difference between the wall thermal exergy and destroyed exergy, as indicated by the exergy balance of Equation 7.57. The exergy quantities are smaller than the corresponding energy quantities. Whereas almost 50 kJ of energy is stored in the PCM, the exergy content is well below 1 kJ for most of the melting process. This disparity highlights the usefulness of exergy analysis. Until the temperature of a substance reaches a useful level, the corresponding exergy is relatively small. This generality in the analysis of TES systems is also observed in the final case study in this chapter.

Closure for Case Study 1

The present case study concerns the modeling of the melting process in a narrow, infinitely long cylinder containing a paraffin-blend PCM. A two-dimensional mesh is constructed in GAMBIT with a uniform meshing structure and simulated using FLUENT 6.3 with the VOF and solidification/melting models. The paraffin PCM initially occupies the bottom 85% of the cylinder volume and the top portion contains air modeled as an ideal gas. The paraffin/air region is initially set to 25 °C, and at time $t > 0$ the wall surrounding the region is set to a constant temperature of 50 °C, allowing heat to be transferred from it to the contents of the cylinder.

The transient behavior of the PCM melting front exhibits unusual trends in terms of shape of the solid fraction due to the omission of natural convection modeling. However, the sinking motion of the solid region enhances heat transfer to a degree, somewhat offsetting the lack of natural convection.

The thermodynamic assessment based on energy and exergy shows the process to be 100% energy efficient at all times since all heat added to the cylinder is recoverable. However, the exergetic performance is much different, with an initial exergy efficiency of 0% that increases to approximately 26% after the 173-s simulation time. These differences indicate the importance of energy quality in TES assessments, particularly since substances at temperatures at or near the reference-environment temperature contain little exergy.

Although the physical configuration, assumptions, and methods used in this latent TES are not entirely based on real-world scenarios (e.g., the omission of natural convection and the use of a constant wall temperature), this case helps demonstrate the use of proper models for phase change with FLUENT. Although the next case study in this chapter is more comprehensive and realistic, the relatively simple case in this section shows how satisfactory results can sometimes be attained while using simplifications to avoid complicated modeling.

7.7.2 Case Study 2: Melting and Solidification of Paraffin in a Spherical Shell from Forced External Convection

This latent TES case study models the charging and discharging processes inside an encapsulated-paraffin latent TES sphere. Because of its complexity, the case is in some way a culmination of the first four case studies in this chapter. The results are validated with experimental data, and the model is subject to rigorous independence testing to ensure satisfactory behavior of the numerical simulation. Then, several input and boundary conditions are considered to determine their impacts on various performance criteria. A detailed discussion of the results is provided, along with a description of the importance of the data obtained.

The case simulated is similar to that reported by Ettouney *et al.* (2005). A paraffin blend is contained in a spherical, copper shell, and air is used as the heat transfer fluid. The paraffin is heated until it completely melts and then cooled to solidification using a fan, which blows air at 10 m/s through a vertical glass tube containing the copper sphere. The experimental apparatus is shown in Figure 7.31.

The glass column has a diameter of 20 cm and a height of 40 cm. The copper sphere, which is suspended by a thin supporting rod, has an outer diameter of 3 cm and a copper wall thickness of 1.2 mm, and is filled with a paraffin PCM. Thermocouples are located throughout the PCM to record temperature variations and also to estimate the energy stored in the capsule during the charging and discharging processes. Owing to the high velocity of the incoming air, heat transfer from the glass column to the ambient environment is neglected.

During charging of the latent store, the air is heated to a specified temperature above the melting point of the PCM, and the fan is used to force convective heat transfer to the sphere from the air. During discharging, the inlet air has a temperature below that of the PCM, so that heat is removed from it and solidification occurs.

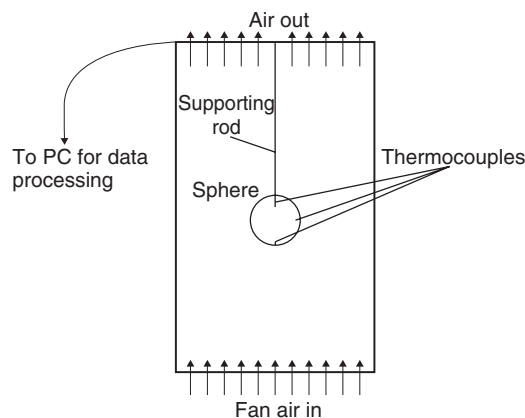


Figure 7.31 Experimental apparatus used for the charging and discharging of the latent store using a forced air flow, modified from Ettouney *et al.* (2005)

The thermophysical properties used for the air and the PCM are taken for specified ranges from Ettouney *et al.* (2005), and in cases where variations exist between the solid and liquid states (e.g., density), the property is taken as the average of the two. Although this is not a precise approximation, its use as a simplifying assumption reduces the cost of computation. The impact on the results of this assumption is assessed subsequently.

The paraffin wax used as the PCM is thus assumed to have a constant density of 820 kg/m^3 , a latent heat of fusion of 210 kJ/kg , and a melting temperature of 48.51°C (321.66 K). Its specific heat and thermal conductivity, taken as the average between solid and liquid states, are taken to be 2.5 kJ/kg K and 0.195 W/m K , while the viscosity of the paraffin wax in the liquid state is taken to be 0.205 kg/m s . The air used as a heat transfer fluid has a density of 1.137 kg/m^3 , specific heat of 1.005 kJ/kg K , thermal conductivity of 0.0249 W/m K , and dynamic viscosity of $2.15 \times 10^{-5} \text{ kg/m s}$. The copper shell, in which the PCM is contained, has a FLUENT-defined density of 8978 kg/m^3 , thermal conductivity of 387.6 W/m K , and specific heat of 0.381 kJ/kg K .

An analysis of the experiment of Ettouney *et al.* (2005) reveals an axis of symmetry, which can be exploited to reduce the computational effort. Consequently, the cylindrical column in Figure 7.31 is split into four quadrants, reducing the computational cost of simulation by 75%. This simplification does not change the validity of the results, as shown subsequently, and lowers simulation times significantly. The quarter-section considered of the physical domain, as created in GAMBIT, is shown in Figure 7.32.

In addition to assuming axisymmetric properties along the cuts made to the original domain, a number of other assumptions are also introduced to facilitate calculations. These include neglecting kinetic and potential energy effects, including buoyancy, and assuming a zero-shear wall (see Equation 7.8) for the symmetric walls in Figure 7.32. In addition, the outer walls, while exhibiting no-slip wall conditions, are assumed adiabatic. Since the heat transfer fluid passes rapidly through the volume, this assumption is both accurate and reasonable; it also simplifies modeling procedures greatly.

Since the HTF experiences drastic pressure, velocity, and temperature gradients in regions near the PCM capsule, the first step in the meshing procedure is to create a boundary layer on the outside of the PCM face. Seven rows of boundary layer meshing are created, with the first layer at a thickness of 0.2 mm and a growth factor of 1.3, resulting in a boundary layer thickness of about 0.35 cm . The cell density in this boundary layer is determined by the meshing of the copper shell. Since this material connects the PCM to the HTF regions, a small mesh spacing here results in a very small initial volume size in the boundary layer region. For this reason, a spacing of 0.2 mm

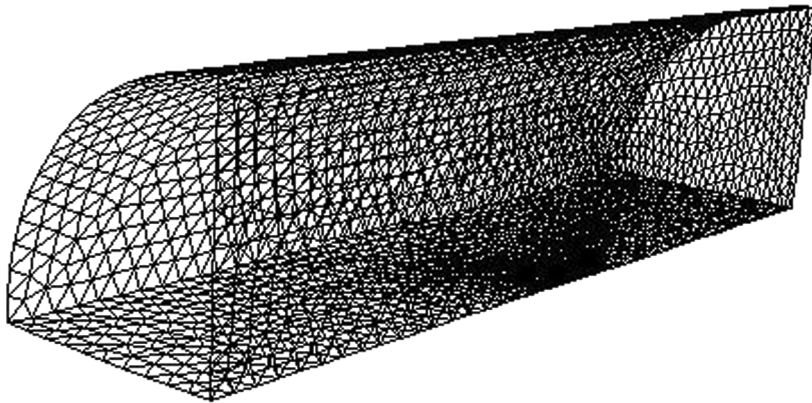


Figure 7.32 Wall grid volumes for the computational domain considered for a latent TES. The PCM capsule volumes are shown in the darker center region

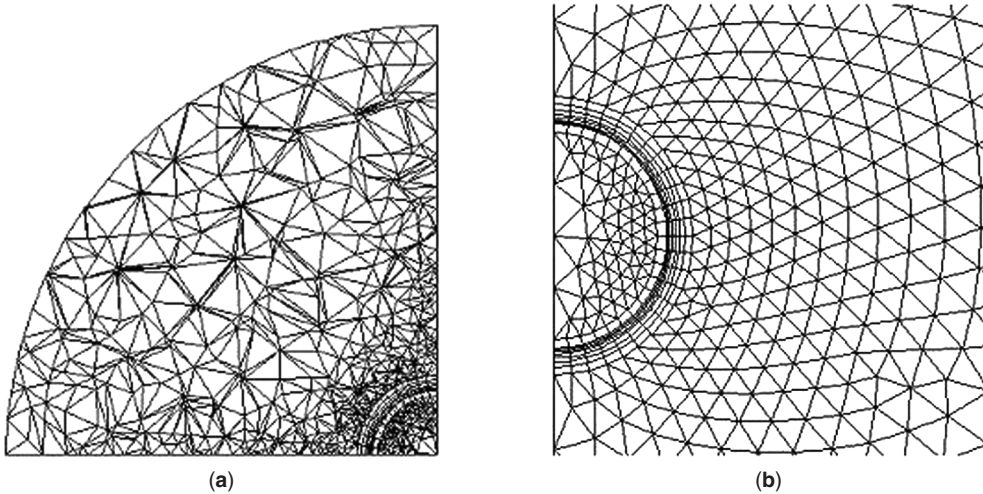


Figure 7.33 Views of the grid cell distributions, for (a) the axial, or flow, direction, and (b) the view of the PCM/HTF cell distribution on the symmetric wall. Note that the view in (a) appears disproportional because of the three-dimensional nature of the grid

is used in the copper region, resulting in 200 volumes for the shell, and the rest of the domain is meshed using 1-cm spacing, resulting in 2048 and 29,616 volumes for the PCM and HTF regions, respectively. Therefore, a total of 31,864 volumes are used for the domain in Figure 7.32. A close-up view of the mesh volumes near the capsule region is shown in Figure 7.33, for lengthwise and axial cross-sections of the grids. The views of the cell densities in Figure 7.33 clearly show that large numbers of volumes are used in regions where computational accuracy is more important, namely, in and around the copper shell.

Once the geometric creation from GAMBIT is loaded into FLUENT, the remaining steps in the simulation setup are concerned with using the correct models, defining material properties, monitoring data for performance calculations, choosing a suitable time step, and setting the residual tolerances. Since these simulations involve phase change, the solidification/melting model is turned on, with the material properties for air, copper, and paraffin as previously described entered. The performance calculations in this case are more complicated than in the previous case studies in this chapter, so the monitors include such quantities as liquid fraction (average), inlet pressure, outlet pressure, temperatures within all domains, and heat flux to the PCM. These are explained in greater detail when the performance criteria are defined.

The case study investigates the effects of variations in the inlet air temperature on the performance of the system. In the study, four cases are considered: two charging and two discharging. For the charging (melting) cases, the initial temperature of the PCM is set to a subcooled temperature 5 °C below its freezing point (i.e., at 316.66 K), while the inlet air temperature is set to either 10 °C or 20 °C above the melting point (i.e., to 331.66 K and 341.66 K). The resulting performance values help indicate which option is more efficient. For the discharging (solidification) cases, the initial temperature is set 5 °C above the melting point (i.e., at 326.66 K) so that the PCM is completely melted. As with the charging case, the inlet air temperatures are set between 10 °C and 20 °C below the melting point (i.e., at 311.66 K and 301.66 K). The reference-environment temperature for exergy calculations in all cases is taken to be 23 °C.

The residual tolerances for this case are set to the default values of 10^{-3} for the x , y , and z velocities and continuity, and 10^{-6} for energy. The time step is determined to be most efficient for simulating the processes when set to 1.0 s, for which the computational time ratio is about

1:1. This case study includes independence testing in which variations are examined in simulation progression when the time step and the grid size change. These discussions are presented in the next section along with a validation of the model.

Validation of Numerical Model and Model Independence Testing

To validate the numerical model, conditions from Ettouney *et al.* (2005) are mirrored so that the resulting temperature variations on the inner portion of the shell can be monitored and compared. The experimental steps are as follows: Air enters the glass column at 60 °C and with a velocity of 10 m/s. The PCM capsule, initially at a temperature of 23 °C, receives heat from the hot air until complete melting is achieved after 1120 s. Then, the air heater is removed and ambient air at 23 °C is used to resolidify the PCM, which occurs after 760 s. The PCM temperatures are recorded with thermocouples located just inside the copper shell at three locations: facing the flow direction, away from the flow direction, and at the side of the sphere where the air moves the fastest. That is, the thermocouples are located at the top, bottom, and side of the sphere as shown in Figure 7.31.

The FLUENT simulation is configured to match the above conditions, and the temperature profiles at the thermocouple locations are monitored by selecting a point in the PCM domain and recording the temperature in the corresponding volume or cell as time progresses. The resulting temperature profiles are shown in Figure 7.34.

Differences between the numerical and experimental temperature profiles are likely because of a number of factors, including contact resistance, effects caused by embedding thermocouples in the PCM, and convection effects in the PCM. However, the solidification and melting times, as well as the overall heat transfer rates, are important to this investigation, the purpose of which is to determine heat transfer characteristics between the PCM and HTF and associated performance criteria.

The time required for the PCM to completely melt is similar with both the experimental and numerical approaches. Complete melting is detected in 600 s experimentally, while the numerical approach quite accurately predicts complete melting in 615 s. A duration of 280 s is required to completely solidify the PCM after solidification is initiated in the experimental unit. This value is again in good agreement (within 1.5%) with the numerically obtained value of 285 s.

The similarities in the numerical and experimental results are encouraging and well within normal acceptable errors when validating a numerical model such as the one considered here. With these

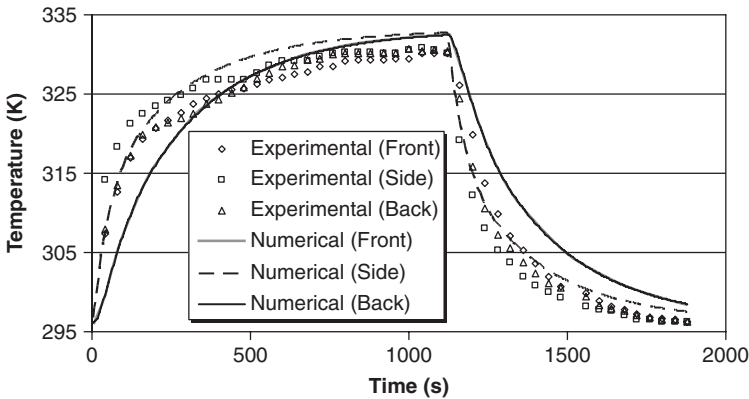


Figure 7.34 Comparison of numerical temperature profiles at three locations in the sphere with the experimental results from Ettouney *et al.* (2005), for the model validation

results, the model can next be subject to grid size and time step validations, to improve confidence in the performance data.

The grid size performance independence tests are presented first. In any numerical model, if the results are to be taken as a realistic representation of actual behavior, the simulation results must be shown to be independent of small changes in the structure of the computational volume. Here, therefore, the mesh spacing is changed in the copper shell region, causing the spacing in the other connected regions of the domain to change correspondingly. The cell density throughout the region is varied so that more and fewer volumes are considered compared to the grid used in the base performance analysis. The cell distribution in all three cases is shown in Table 7.1.

To determine the dependence of the overall results on the small changes in cell distribution, simulations are performed using the same conditions as in the model validation tests in Figure 7.34, and the variation of the liquid fraction inside the PCM with time is monitored. The resulting liquid fraction variations are shown in Figure 7.35.

Since the liquid fraction is a good indicator of the heat transfer characteristics to and from the capsules, it is taken here to be a sufficient gauge of the overall grid performance. From Figure 7.35, it can be clearly observed that the changes in grid size have little impact on the overall solutions. Hence, the chosen grid size and orientation are deemed adequate. In general, care must be taken when initially choosing the cell distribution in a computational domain to ensure the model is not only able to model physical scenarios well but also capable of passing grid independence tests.

The time step independence is now tested. In the present case, the time step is set to 1.0 s. The dependence of the simulation progression on changes in time step can be evaluated straightforwardly

Table 7.1 Cell distribution for the three cases considered in the grid independence tests for the sphere

Cell data	Grid size		
	Small	Base	Large
Mesh spacing in copper shell (cm)	0.21	0.20	0.18
Mesh volumes in copper region	164	200	221
Mesh volumes in PCM region	1,523	2,048	2,313
Mesh volumes in air (HTF) region	27,775	31,864	33,238
Total volumes	29,462	32,312	35,772

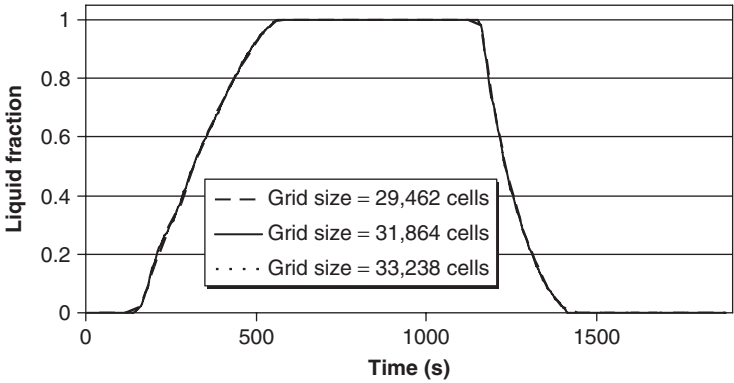


Figure 7.35 Liquid fraction as a function of time for the grid size independence tests for the sphere

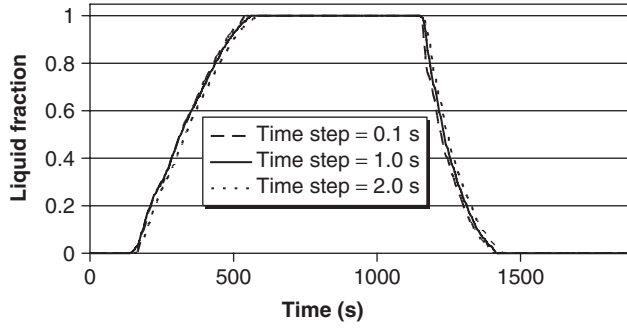


Figure 7.36 Liquid fraction as a function of time for the time step independence tests for the sphere

by altering the time step in the FLUENT controls, and monitoring the changes in liquid fraction for the overall process. To illustrate, alternative time steps of 0.1 s and 2 s are considered, and the resulting liquid fraction variations with time are shown in Figure 7.36.

The liquid fraction variations in Figure 7.36 correlate very well for all time steps considered, suggesting that the step of 1.0 s used in the initial analysis is adequate. Although the smaller time step of 0.1 s may permit a more accurate representation of the physical domain and phenomena, the computational cost is increased tenfold, increasing the simulation time greatly and, depending on the computer resources available, perhaps unreasonably. For the time step of 2 s, little difference is observed in the variation of liquid fraction while computational cost is severely decreased but, although not shown here, it was found that increasing the time step beyond 2.0 s significantly influenced the validity of results. This test shows the importance of choosing the time step appropriately. The selection of time step and grid sizes can serve as a useful tool for determining the most computationally efficient scenario for any given problem.

With the model having been validated and passing time step and grid size independence testing, the remainder of the analysis focuses on the performance criteria.

Performance Criteria

Since kinetic and gravitational potential energy effects are neglected, the energy balance for a system undergoing either charging or discharging processes can be written as follows:

$$\Delta E_{\text{sys}} = E_{\text{in}} - E_{\text{out}} = U_{\text{in}} - U_{\text{out}} \quad (7.65)$$

The change in energy of the system itself is comprised of the changes in energy of each material within the domain, namely, the air, copper, and PCM (paraffin) regions:

$$\Delta E_{\text{sys}} = \Delta E_{\text{air}} + \Delta E_{\text{copper}} + \Delta E_{\text{pcm}} \quad (7.66)$$

The change in energy of the air and copper regions at any time can be calculated using the change in volume-averaged temperature within each region:

$$\Delta E_{\text{air}} = m_{\text{air}} C_{\text{air}} (\bar{T}_{\text{air}} - T_{\text{air,ini}}) \quad (7.67)$$

$$\Delta E_{\text{copper}} = m_{\text{copper}} C_{\text{copper}} (\bar{T}_{\text{copper}} - T_{\text{copper,ini}}) \quad (7.68)$$

Owing to the complexities resulting from solid/liquid interfaces within the PCM, its energy change is evaluated by monitoring the heat transfer from the copper to the PCM on the inner surface of

the copper shell:

$$\Delta E_{pcm} = \int_0^t Q_w dt = \sum_{i=0}^t Q_{w,t} \quad (7.69)$$

The efficiency of the system in general differs for each process. First, we consider energy efficiencies. For the charging process, the purpose is to add heat to the PCM region. In other words, the energy content of the PCM and copper shell regions is increased, while the energy input to achieve this objective is the change in enthalpy from inlet to outlet of an HTF (air in the present case).

$$\eta_{ch} = \frac{E_{prod}}{E_{input}} = \frac{\Delta E_{sys}}{H_{in} - H_{out}} = \frac{\Delta E_{sys}}{U_{in} - U_{out} + V(p_{in} - p_{out})} \quad (7.70)$$

The term $V(p_{in} - p_{out})$ can be written as follows:

$$V(p_{in} - p_{out}) = \frac{\dot{m}t}{\rho_{air}} \int_0^t (\bar{p}_{in} - \bar{p}_{out}) dt = \frac{\dot{m}t}{\rho_{air}} \sum_{i=0}^t (\bar{p}_{in,t} - \bar{p}_{out,t}) \quad (7.71)$$

During discharging, the purpose is to recover heat from the solidifying PCM, so that the total enthalpy received from the capsule is the product energy content. The total energy obtained is the change in energy of the PCM and its shell:

$$\eta_{dc} = \frac{E_{prod}}{E_{input}} = \frac{H_{in} - H_{out}}{\Delta E_{sys}} = \frac{U_{in} - U_{out} + V(p_{in} - p_{out})}{\Delta E_{sys}} \quad (7.72)$$

The change in energy of the system is negative during the discharging process, and there is a drop in pressure through the column. The energy efficiency varies between 0% and 100% for both discharging and charging cases. Although the dependence of the evaluated parameters on the progression time of the simulation is not written explicitly here, the energy and exergy efficiencies are examined as the simulation time progresses.

The exergy performance criteria can be similarly examined. For charging or discharging processes, the exergy balance can be expressed as follows:

$$\Delta \Xi_{sys} = \epsilon_{in} - \epsilon_{out} - I \quad (7.73)$$

Here, I denotes exergy destruction and includes exergy destroyed because of heat transfer and viscous dissipation in the flowing fluid. The exergy balance excludes thermal exergy flows across system boundaries, since the walls are assumed adiabatic. The exergy destruction can be determined with an entropy balance:

$$I = T_{\infty} \Pi \quad (7.74)$$

where

$$\Delta S_{sys} = S_{in} - S_{out} + \Pi \quad (7.75)$$

The change in entropy of the system is calculated as the summation of the changes in entropy for each of its three components:

$$\Delta S_{sys} = \Delta S_{pcm} + \Delta S_{copper} + \Delta S_{air} \quad (7.76)$$

where

$$\Delta S_{pcm} = \frac{\Delta E_{pcm}}{\bar{T}_{m,pcm}} = \sum_{i=0}^t \frac{Q_{w,t}}{\bar{T}_{m,pcm}} \quad (7.77)$$

$$\Delta S_{copper} = m_{copper} C_{copper} \ln \left(\frac{\bar{T}_{m,copper}}{T_{ini}} \right) \quad (7.78)$$

$$\Delta S_{air} = m_{air} C_{air} \ln \left(\frac{\bar{T}_{m,air}}{T_{ini}} \right) \quad (7.79)$$

The above expression for ΔS_{pcm} presumes that no entropy generation occurs within the PCM. Further, it is assumed that heat transfer to the PCM occurs at its mean temperature. The expressions for ΔS_{copper} and ΔS_{air} assume incompressible fluid behavior and constant specific heats.

The difference between inlet and outlet entropy is dependent on the flow temperatures, so that after time t the entropy difference is

$$S_{in} - S_{out} = \sum_{i=0}^t \dot{m} C_{air} \ln \left(\frac{T_{in}}{\bar{T}_{out,t}} \right) \quad (7.80)$$

To solve the exergy balance, the total exergy change of the system is needed at each time t . The exergy balance depends on the change in energy of the system as well as the entropy change:

$$\Delta \Xi_{sys} = \Delta E_{sys} - T_{\infty} \Delta S_{sys} \quad (7.81)$$

With this information, the charging and discharging exergy efficiencies can be written analogously to their energy counterparts:

$$\psi_{ch} = \frac{\Delta \Xi_{sys}}{\epsilon_{in} - \epsilon_{out}} \quad (7.82)$$

$$\psi_{dc} = \frac{\epsilon_{in} - \epsilon_{out}}{\Delta \Xi_{sys}} \quad (7.83)$$

The energy and exergy efficiencies can now be assessed while the simulation progresses.

It is instructive to examine the nature of the irreversibilities, which are a result of viscous dissipation within the fluid and heat transfer. The exergy destruction associated with viscous dissipation can be expressed as follows:

$$I_{dissipative} = T_{\infty} \Pi_{dissipative} \quad (7.84)$$

The exergy destroyed via heat transfer during the melting and solidification processes can be written as the difference between the overall exergy destruction I and the exergy destruction associated with viscous dissipation:

$$I_{ht} = I - I_{dissipative} \quad (7.85)$$

Results and Discussion

For the charging and discharging processes, many of the performance results as well as energy and exergy quantities are presented here as a function of a dimensionless time t^* , defined as

$$t^* = \frac{t}{t_{sf}} \quad (7.86)$$

where t_{sf} denotes the time for total solidification or melting.

The liquid fractions for solidification and melting are plotted against this dimensionless time in Figure 7.37. In this figure, as noted previously, inlet air temperatures 10°C and 20°C above the

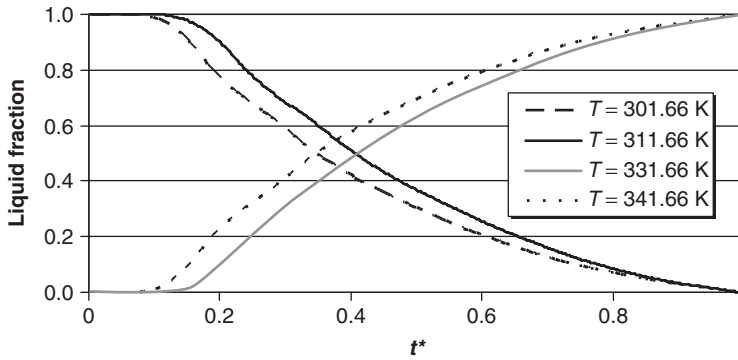


Figure 7.37 Variation of liquid fraction for the charging and discharging cases with dimensionless time t^* , for several inlet air temperatures

melting point (i.e., at 331.66 K and 341.66 K) are considered for the charging (melting) cases, while inlet air temperatures 10 °C and 20 °C below the melting point (i.e., at 311.66 K and 301.66 K) are considered for the discharging (solidification) cases. It is observed in Figure 7.37 that inlet air temperatures, which are further removed from the phase change temperature, promote heat transfer more readily between the air and the copper capsule, causing the liquid fraction to decrease more rapidly for the solidification process and increase more rapidly for the melting process.

To illustrate the energy-related processes during charging and discharging, energy quantities for each case are shown in Figures 7.38 and 7.39. These include the heat generated through viscous dissipation, the energy stored during charging, and the energy recovered during discharging.

The heat generated through viscous dissipation for both the charging and discharging cases is small compared with the stored and recovered energy quantities. This result is expected, since heat generation through viscous dissipation is usually small compared to the input and recovered thermal energy quantities in most TES systems. In this case study, the high velocity of the heat transfer fluid (air) causes the heat generation through viscous dissipation to be somewhat larger than usual.

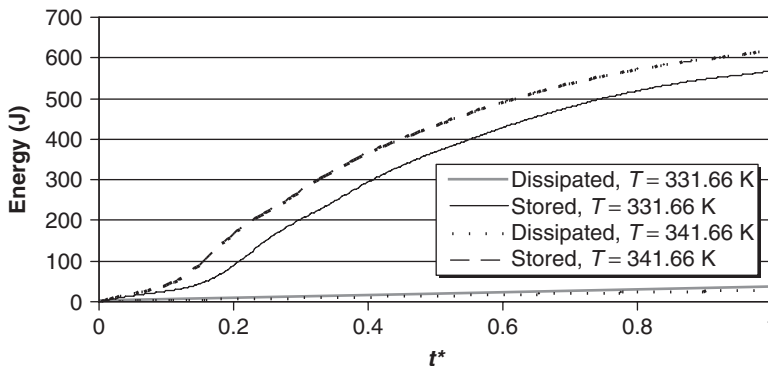


Figure 7.38 Variation of the energy stored and the heat generated through viscous dissipation for the two charging cases, as represented by the two inlet air temperatures considered

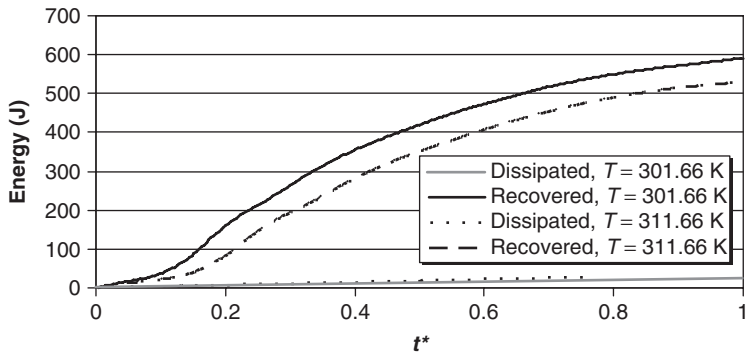


Figure 7.39 Variation of the energy recovered and the heat generated through viscous dissipation for the two discharging cases, as represented by the two inlet air temperatures considered

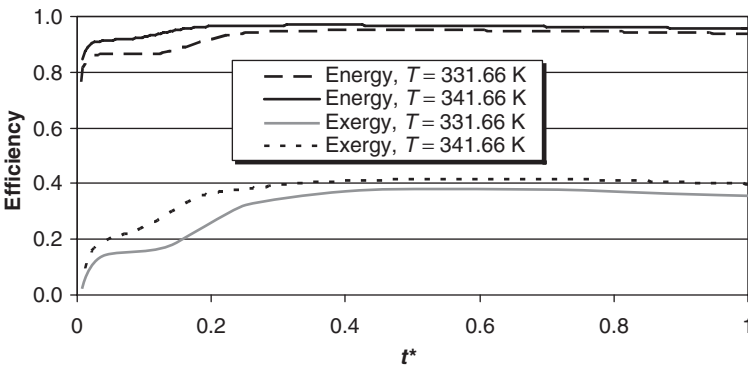


Figure 7.40 Variation of energy and exergy efficiencies with dimensionless time t^* for the charging process, for two inlet air temperatures

Energy and exergy efficiencies are shown in Figures 7.40 and 7.41 for the charging and discharging cases, respectively. Note that there are no external heat losses from the system shown in Figure 7.31, so the energy efficiencies accounting for only external energy losses are always 100%. In this case study, the heat generated through viscous dissipation, which is relatively small, is assumed unrecoverable and thus treated as an energy loss. Hence, the energy efficiencies are somewhat less than 100%. The exergy efficiencies in Figures 7.40 and 7.41 are discussed further after the various exergy quantities (destroyed, stored, and recovered) are presented.

Energy efficiency varies with dimensionless time as observed because the stored and recovered energy quantities in the initial stages of the simulations are high because of the good heat transfer characteristics of the copper shell. The shell's high thermal conductivity permits it to convey heat readily when $t^* < 0.1$. As t^* increases, the paraffin must be heated or cooled to its fusion temperature, so little heat storage or retrieval occurs until melting or solidification begins. Heat storage or retrieval further increases the energy efficiency until $t^* \approx 0.6$, where a maximum is realized (although the efficiency is fairly constant for $t^* > 0.3$). The existence of this energy efficiency maximum can be attributed to the superheating of the paraffin liquid state (or supercooling of the solid state), which reduces heat transfer significantly. Since the energy stored or retrieved is slightly curtailed, the energy efficiency decreases.

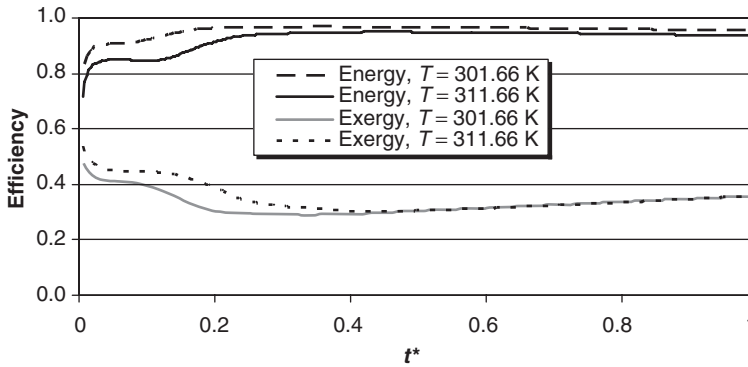


Figure 7.41 Variation of energy and exergy efficiencies with dimensionless time t^* for the discharging process, for two inlet air temperatures

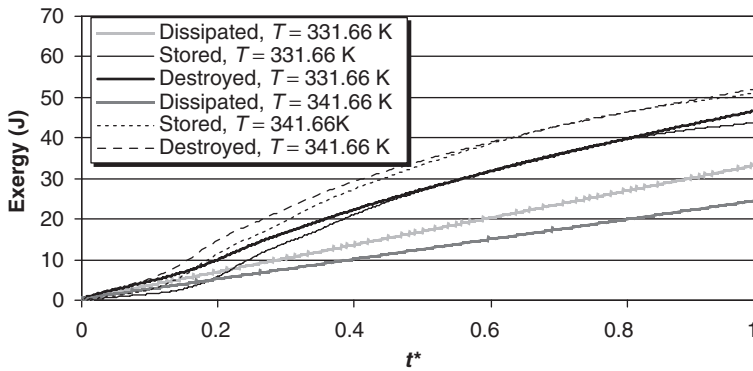


Figure 7.42 Variation with dimensionless time t^* of exergy stored, destroyed via viscous dissipation, and destroyed via heat transfer during charging, for two inlet air temperatures

Another important observation in Figures 7.40 and 7.41 is that the energy efficiencies are higher for inlet air temperatures that lead to lower solidification or melting times. Inlet air temperatures that decrease the simulation time also decrease the energy loss, thereby increasing the energy efficiency.

To explain the behaviors of the exergy efficiencies, the quantities of exergy destroyed, stored, and recovered are shown in Figures 7.42 and 7.43. Two primary exergy destruction mechanisms occur, and both are considered: exergy destruction as a result of irreversibilities associated with viscous dissipation (referred to as *dissipated*) and exergy destruction due to irreversibilities associated with heat transfer (referred to as *destroyed*). This use of “dissipated” and “destroyed” is followed throughout the remainder of this case study.

The variations in exergy quantities with time for the charging and discharging cases are noteworthy. A complex balance exists between the magnitudes and modes of exergy destroyed and recovered (or stored), which affects the exergy efficiency. The balance suggests multiple interpretations of the most efficient scenario. The main factors involved are the entropy production associated with the two irreversibilities: viscous dissipation and heat transfer.

In Figures 7.42 and 7.43, the largest exergy quantity is the destroyed exergy due to heat transfer, followed by the stored (recovered) exergy, and then the exergy destruction due to viscous

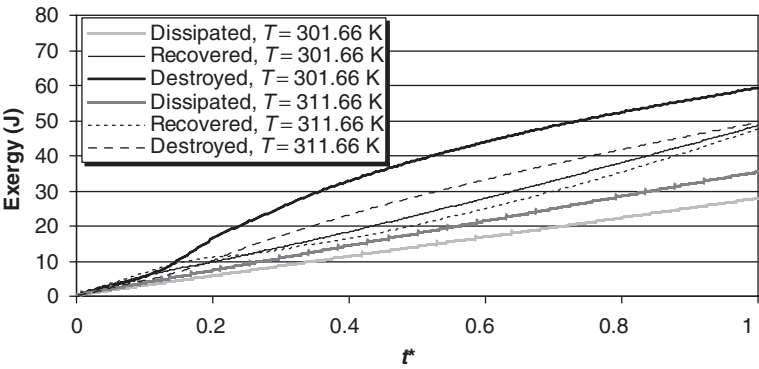


Figure 7.43 Variation with dimensionless time t^* of exergy recovered, destroyed via viscous dissipation, and destroyed via heat transfer during discharging, for two inlet air temperatures

dissipation. This finding suggests that the temperature of the inlet air is an important factor when optimizing charging or discharging processes involving latent encapsulated PCMs. Note that when the inlet air temperature is further removed from the solidification temperature, the exergy destruction associated with heat transfer increases. However, since reducing the difference between the inlet air temperature and the PCM solidification temperature raises the charging/discharging time, the exergy destruction due to viscous dissipation is greatly increased in this instance, which reduces the exergy efficiency.

The destroyed exergy due to heat transfer and viscous dissipation, as well as the overall destroyed exergy, after solidification or melting is shown in Figure 7.44 for each air inlet temperature case.

An important inference from the results is that efficiencies increase as inlet temperatures are lowered for the discharging case and are raised for the charging case. This result can be attributed to the increased viscous dissipation in the computational domain as the air speed used to charge or discharge the capsule rises. Note that in most cases the heat transfer fluid used in macroencapsulated paraffin PCMs is not air, but rather a glycol-based refrigerant (for cold storage) or water (for warm storage). These fluids have advantageous thermophysical properties (e.g., relatively high specific heats), heat transfer characteristics, and low costs. Thus, the results of the current case study are most meaningful when a high pressure head is present during charging or discharging.

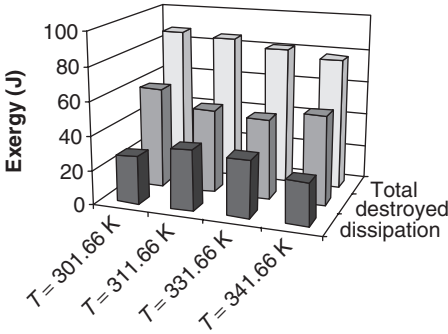


Figure 7.44 Exergy destroyed via viscous dissipation and heat transfer, and the total exergy destruction, after the overall storage process, for all inlet air temperature cases

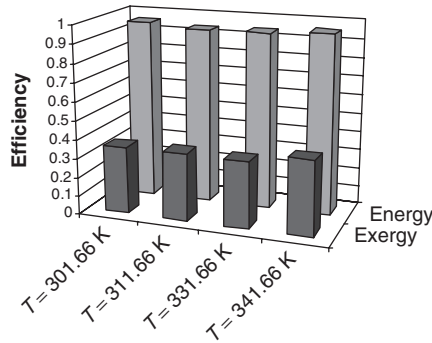


Figure 7.45 Energy and exergy efficiencies at the completion of the overall storage process, for all inlet air temperature cases

In most other packed-bed analyses, the irreversibility associated with heat transfer usually is responsible for the dominant exergy loss. For example, consider the detailed TES investigation by MacPhee (2008) of the charging and discharging efficiencies over a wide range of inlet temperatures, flow rates, and geometries, including spherical, cylindrical, and slab capsules. The capsules are situated in a packed bed of similar capsules, and an ethylene glycol solution is the heat transfer fluid. The results indicate that all processes are more efficient at lower inlet velocities, which decreases the exergy destroyed due to viscous dissipation (rendering it almost negligible). As a result, the dominant exergy loss is the exergy destruction due to heat transfer, and this quantity decreases as inlet temperature approaches the solidification temperature.

For higher inlet velocities of the heat transfer fluid, the results suggest that it may be more efficient to consider inlet temperatures, which achieve solidification or melting more quickly, to decrease exergy destruction via viscous dissipation. This result could be useful for understanding TES using microencapsulated packed beds or any medium that normally experiences a high pressure drop in a flowing heat transfer fluid. Nonetheless, the irreversibility associated with heat transfer is likely to be of major importance for any space heating or cooling applications. This irreversibility is reduced when the two materials exchanging heat are at similar temperatures. When larger temperature differences exist, entropy generation and exergy destruction are greater. In most cases, like those reported by MacPhee (2008), it is beneficial in terms of efficiency to keep the inlet temperature close to the fusion temperature of the PCM.

The overall energy and exergy efficiencies after the solidification or melting processes are completed are shown in Figure 7.45.

An important outcome of this case study is the demonstration provided of the usefulness and versatility of exergy analysis. From an energy perspective, only heat generation through viscous dissipation is considered a loss (and usually even this is not treated as a loss), resulting in very high overall efficiencies. In Figure 7.45, exergy efficiencies are contrasted with their energy counterparts. The lower magnitudes of the exergy efficiencies reflect more accurately and comprehensively the actual efficiency of the TES system.

Since exergy analysis provides a detailed understanding of system performance and efficiency as well as the exergy destroyed and its breakdown by cause, the method allows designers to test different options and determine performance trends, ultimately facilitating system enhancements and optimization.

Extension to Other Geometries

An advantageous aspect of TES numerical simulation is that once the numerical scheme is validated and found to be independent of grid and time step changes, it can be applied to a range of similar

applications. For the present case study, for instance, alternative geometries can be investigated to determine the most beneficial configuration of the PCM capsule. Further, the effect could be examined by varying physical properties and the inlet temperature and flow rate of the heat transfer fluid. Here, the effect of geometry variation is examined.

Two alternative capsule geometries are considered: cubic and cylindrical. Performance data are obtained for these cases and compared to those for the spherical capsule. The PCM volume is fixed at the same value for all geometries, and the quantities of energy and exergy stored and recovered are determined. For all cases, the capsule contains the same paraffin PCM, has the same shell material and thickness, and undergoes one charging and one discharging process. The inner length of the cubic capsule is therefore 2.225 cm and the outer length is 2.465 cm. The inner height and diameter for the cylindrical capsule are set to be equal, so the inner diameter (and height) is 2.411 cm, while the outer diameter (and height) is 2.651 cm. The grid meshing is developed in a similar manner as for the spherical capsules, with similar grid sizes and a higher density on the capsule outer surfaces.

After the geometries are properly created and segmented, the same simulation procedures are performed as for the spherical element. To properly compare the new geometries, one charging and one discharging process is simulated for each element, with the inlet temperature for charging and discharging set to 341.66 K and 301.66 K, respectively. The inlet air velocity is fixed at 10 m/s, while the initialization temperature in the PCM and copper regions for the charging and discharging case are 316.66 K and 326.66 K, respectively. Consequently, performance comparisons can be made for the spherical, cubic, and cylindrical cases.

The overall energy and exergy efficiencies are shown in Figure 7.46 for the three cases. Note that the overall efficiencies are obtained by multiplying the charging and discharging efficiencies.

The cylindrical capsule attains the highest efficiency from both energy and exergy perspectives. This result is due to a number of factors, most of which are more readily explained once the modes of exergy destruction are considered, as is done in Figure 7.47.

The exergy destruction values in Figure 7.47 can explain the overall efficiencies by separating the destroyed exergy by cause. First, the exergy destroyed due to viscous dissipation is greatest in the cubic capsule. This observation is expected based on aerodynamic considerations since a cubic capsule has the most drag of the three geometries and creates higher velocity gradients, especially at the edges. The spherical capsule experiences much lower dissipated exergy, while the lowest amount is experienced by the cylindrical capsule. Owing to the higher surface area to volume ratio of the cylindrical capsule, it experiences lower charging and discharging times, and as such realizes less total dissipation.

The energy efficiencies in Figure 7.46 indicate that the cylindrical capsule achieves the highest energy efficiency, followed by the spherical and cubic capsules.

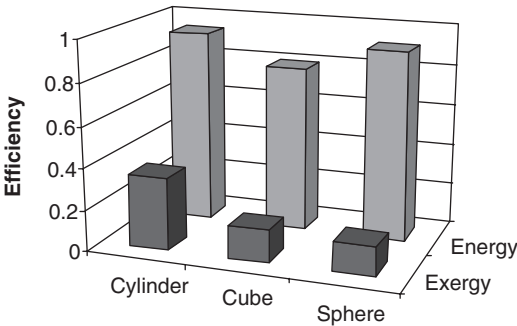


Figure 7.46 Overall energy and exergy efficiencies for charging and discharging for the three storage capsule geometries

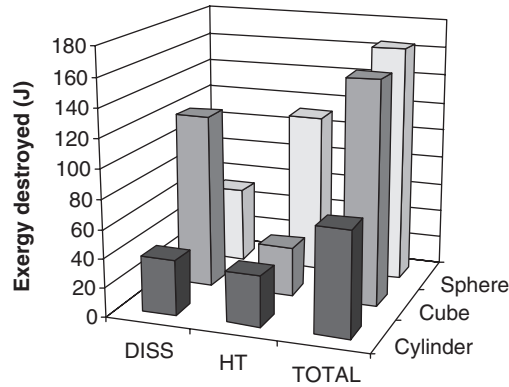


Figure 7.47 Exergy destroyed for several storage capsule geometries by viscous dissipation (DISS), heat transfer (HT), and their combination (TOTAL)

The exergy destruction due to heat transfer is greatest for the spherical capsule, followed by the cylindrical and cubic capsules. The spherical capsule realizes the largest exergy destruction due to its poor heat transfer characteristics. The other geometries have higher surface areas and thus transfer heat more efficiently. When overall exergy destruction is considered, however, the cylindrical capsule is observed to be preferable, followed by the cubic and spherical capsules. These results are reflected in the exergy efficiencies, as greater exergy destruction results in lower efficiencies.

This brief assessment demonstrates the versatility of numerical simulations and supports their use in similar studies. Provided proper validation and independence tests are completed, a model may be run for other cases in lieu of experimentation. However, a more detailed analysis is required in this particular case before generalizations can be inferred about performance when geometry and heat transfer fluid flow conditions are varied.

Closure for Case Study 4

This latent TES case study addresses the charging and discharging of a paraffin wax storage contained in a copper shell, which is suspended in a glass column, while air is used as a heat transfer fluid to transfer heat convectively to and from the capsule. The inlet air velocity is set at 10 m/s, and four inlet air temperature cases are investigated: 341.66 K and 331.66 K for charging and 311.66 K and 301.66 K for discharging. The solidification temperature of the paraffin wax is 321.66 K, and trials are conducted until the liquid fraction reaches 1 in the charging case and 0 in the discharging case. Energy and exergy efficiencies, as well as the different modes of losses, are obtained as a function of time.

Before simulation data can be used reliably, a detailed model validation must be conducted. This validation demonstrated the accuracy of the numerical procedures. In addition, time step and grid size independence tests showed that the model provides an accurate representation of real-world scenarios.

The results indicated that energy analysis is incomplete and misleading for assessing TES losses. For the charging cases, the processes have energy efficiencies of 93.4% and 95.4% for inlet temperatures of 311.66 K and 301.66 K, respectively. The corresponding exergy efficiencies are 36.0% and 35.8%, indicating that the charging process is much less efficient than indicated considering energy. The lower efficiencies are due to the decreased exergy content of the PCM storage compared to its energy content, as well as the increased losses from two modes of entropy generation: viscous dissipation and heat transfer.

For the discharging processes, the inlet temperatures are 331.66 K and 341.66 K, respectively, and the corresponding energy efficiencies are 93.8% and 95.6%, while the corresponding exergy efficiencies are 35.2% and 39.8%. The differences between energy and exergy efficiency values for the discharging processes mirror those for the charging processes.

Following the spherical geometry simulations, two more geometry cases (cylindrical and cubic) are considered to assess their performances with identical PCM volumes. The cases demonstrate the versatility of numerical simulation and show the cylindrical capsule to have the highest overall energy and exergy efficiencies because of a smooth profile and a high surface area to volume ratio.

Although exergy destruction due to viscous dissipation is a major loss in all cases considered here, it is observed for most sensible or latent TES systems that viscous dissipation is not the major source of irreversibility. Viscous dissipation is important for quickly moving flows. Designers can use exergy analyses to perform detailed optimization and improve efficiency.

This case study is intended to give the reader a good understanding of the modeling, validation, testing, and simulation procedures necessary for all numerical simulations of latent TES. It is hoped that the four case studies considered to this point in this chapter allow the reader to conduct TES case assessments typical of those used by industry today. By using the techniques presented here in sensitivity or parametric analyses, optimization or loss minimization schemes can be realized relatively straightforwardly and inexpensively.

7.8 Illustrative Application for a Complex System: Numerical Assessment of Encapsulated Ice TES with Variable Heat Transfer Coefficients

Encapsulated ice storage systems are an effective type of TES in part because they have a large heat transfer area per unit storage volume, resulting in higher heat transfer rates. Such latent TES systems and the phase change that takes place within them in the PCM capsules are the focus of this illustrative application.

An average heat transfer coefficient is commonly used for heat transfer analysis, whether analytical or numerical, in encapsulated ice TES systems. In reality, the heat transfer coefficient changes along the flow path since the fluid flow around capsules is not hydrodynamically and thermally developed. In most instances, consequently, the results deviate significantly compared to experimental data. More accurate heat transfer coefficients and correlations are thus desirable, and are obtained in this illustrative application by simulating a series of 120 numerical “experiments” for encapsulated ice TES systems, considering various capsule diameters, mass flow rates, and temperatures of the heat transfer fluid. Changes in the heat transfer coefficient along the flow path are thus taken into account, avoiding the need to use the average heat transfer coefficients for encapsulated TES. We compare the numerical results with experimental data.

Only the charging process is examined in this section, which is adapted from a recent investigation (Erek and Dincer, 2009).

7.8.1 Background

Modeling and analytical assessments of latent TES systems have been reported for some time, as have experimental studies. More recently, latent TES systems have been investigated numerically, and often verified with experimental data. Some of these are reviewed here, as they pertain to this illustrative application.

Numerical assessments of many types have been reported for TES. Tao (1967) presented a numerical method, using constant values of heat capacity and thermal conductivity for the solid region and a constant heat transfer coefficient, for solidification inside both cylindrical and spherical containers. Shih and Chou (1971) describe an iterative method for predicting solidification in

spherical capsules, while Ismail and Henriquez (2000) apply a finite difference approximation and moving-grid approach to solidification in a spherical container. Ismail *et al.* (2003) numerically assessed heat transfer during the solidification of water inside a spherical nodule, and discussed the effect on solidification time and rate of container size and material and flow parameters. A numerical investigation of inward solidification of a PCM encapsulated in cylindrical and spherical containers yielded a correlation that expresses the dimensionless total solidification time in terms of Stefan number, Biot number, and a superheat parameter (Bilir and İlken, 2005). Kousksou *et al.* (2005) used a two-dimensional porous-medium approach to describe the effect of storage tank position and the flow pattern inside a tank containing spherical capsules.

Various experimental TES assessments have also been reported. Eames and Adref (2002) experimentally investigated the heat transfer characteristics for water in spherical elements during TES charging and discharging processes and introduced a method to measure interface position during solidification. Chen *et al.* (1999) examined experimentally the nucleation probability of supercooling, that is, cooling the contained liquid (water inside capsules) to below its freezing point prior to solidification and investigated the effect of different factors on the nucleation behavior. This information is important since encapsulated containers can be subject to supercooling, which can occur in fully discharged containers and reduces the heat transfer rate at the beginning of charging, but which can be significantly reduced by the addition of nucleating agents. Chen *et al.* (2000) examined the thermal behavior of an encapsulated cold TES during charging for varying inlet coolant temperatures and flow rates. An investigation of the thermal characteristics of paraffin wax in a spherical capsule during freezing and melting showed that the average heat transfer coefficient around capsules is affected by the inlet and initial temperature and Reynolds number more during melting than freezing due to the effect of natural convection during melting (Cho and Choi, 2000).

Numerical TES assessments often use experimental data for verification purposes. For instance, numerical and experimental investigations of the heat transfer characteristics associated with phase change in a horizontal cylindrical capsule containing a paraffin wax PCM demonstrated that melting is mainly governed by the Stefan number (Regin *et al.*, 2006). Also, Bedecarrats *et al.* (1996) introduced a model that accounts for supercooling and investigated experimentally and numerically the energy storage in a tank filled with PCM encapsulated in spherical capsules.

7.8.2 System Considered

The encapsulated ice TES considered is shown in Figure 7.48. The TES system consists of a cylindrical tank of height H and diameter D_{inf} and contains PCM spherical capsules. The tank is completely insulated and the PCM, which is pure water, is homogenous and isentropic. The thermal behavior of the TES system is investigated numerically for the charging process, in which a cold heat transfer fluid flows over capsules and the PCM in the capsules solidifies. Solidification begins at the capsule surface and moves toward the center with time.

7.8.3 Modeling and Simulation

The modeling of the heat transfer for the ice TES is described, along with assumptions and simplifications. Also, the numerical simulation process is explained, including initial and boundary conditions and the simulation procedure employed.

Assumptions

The following assumptions are considered in the numerical model:

- The temperature in the tank changes mainly along axial direction with time.
- Heat transfer within the container is dominated by conduction in the radial direction.

- The heat flux is isotropic over the PCM capsule area.
- Natural convection in the tank is negligible.
- Thermophysical properties of the container wall and the heat transfer fluid are independent of temperature.
- Thermophysical properties of the PCM in the solid and liquid phases differ.

Heat transfer

Since such a three-dimensional and time-dependent system is difficult to model and analyze numerically, the system is simplified using symmetry surfaces. The resulting system includes four quarter-sphere capsules and the heat transfer fluid around them, as shown in Figure 7.49. This three-dimensional view is utilized in the numerical simulation. Assuming that heat loss from the system is negligible, the heat transfer equation for the heat transfer fluid can be expressed as

$$\varepsilon \rho_f c_f \frac{\partial T_f}{\partial t} + \rho_f c_f u \frac{\partial T_f}{\partial x} = \frac{\partial}{\partial x} \left(\varepsilon k_f \frac{\partial T_f}{\partial x} \right) + \frac{q_{capsule}^0}{V_{CV}} \quad (7.87)$$

where $q_{capsule}^0$ represents the heat transfer from the capsules to the heat transfer fluid. As seen in Figure 7.49, the fluid around the four quarter-capsules is taken as the control volume. This is done because the discretization of Equation 7.87 is simpler. The assumption of constant surface temperature and temperature distribution in only the radial direction leads to heat conduction inside the capsules. Heat transfer between the heat transfer fluid and the PCM inside the capsules can be determined using the following analogy:

$$q_{capsule}^0 = \frac{T_{s,i} - T_{f,i}}{R_{t,cond} + R_{t,conv}}$$

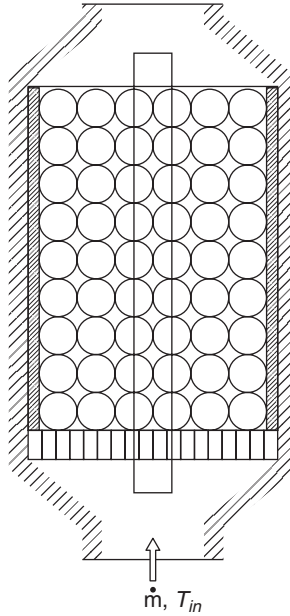


Figure 7.48 Physical model of ice TES system

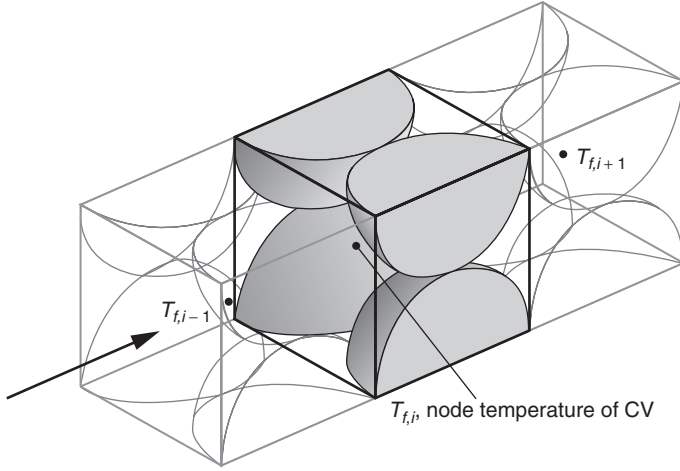


Figure 7.49 Segment of ice TES system used for numerical simulation

Here, $R_{t,cond}$ and $R_{t,conv}$ represent thermal conduction and convection resistances, respectively. After substituting these terms, this expression can be written as

$$q_{capsule}^0 = \frac{T_{s,i} - T_{f,i}}{\frac{1}{h\pi D^2} + \frac{1}{2\pi k} \left(\frac{1}{D_i} - \frac{1}{D} \right)}$$

Rewriting Equation 7.87 in the dimensionless form,

$$\varepsilon C_f \frac{\partial \theta_f}{\partial Fo} + C_f \text{Re}_f \text{Pr}_f \frac{\partial \theta_f}{\partial X} = \frac{\alpha_l}{\alpha_f} \frac{\partial}{\partial X} \left(\varepsilon K_f \frac{\partial \theta_f}{\partial X} \right) + \frac{q_{capsule}'''}{Dk_f (T_m - T_{in})} \quad (7.88)$$

The heat transfer can then be written in dimensionless form as

$$q_{capsule} = \frac{\pi (\theta_{s,i} - \theta_{f,i})}{\frac{1}{\text{Nu}_f} + \frac{K_f}{K_w} \left(\frac{t_w}{1 - 2t_w} \right)} \quad (7.89)$$

Note that the relation between $q_{capsule}$ and $q_{capsule}^0$ is $q_{capsule} = q_{capsule}^0 / Dk_f (T_m - T_{in})$. The Nusselt number Nu_f is obtained using CFD. Details on the numerical analysis are given in the next section.

To link the heat transfer between capsules and the heat transfer fluid, the heat transfer equation for the PCM capsules must be solved. The heat transfer equation in the spherical capsules is described by a temperature transforming method using a fixed-grid numerical model (Cho and Choi, 2000). In this method, it is assumed that phase change occurs over a temperature range from $T_m - \delta T_m$ to $T_m + \delta T_m$. This approach can also be used to simulate the solidification process occurring at a single temperature by taking a small range of phase change temperature, $2\delta T_m$. Where water is used as the PCM, there is a quick transition from solid to liquid and the value of the dimensionless semirange phase change temperature, $\delta\theta_m$, is taken as 0.001.

The dimensionless heat transfer equation for the PCM in the capsules can be written as

$$\frac{\partial(C\theta)}{\partial Fo} = \frac{\alpha_l}{\alpha_f} \frac{1}{R^2} \frac{\partial}{\partial R} \left(KR^2 \frac{\partial \theta}{\partial R} \right) - \frac{\partial S}{\partial \tau} \quad (7.90)$$

where

$$\begin{aligned}
 C = C(\theta) &= \begin{cases} C_{sl} & \theta < -\delta\theta_m & \text{Solid} \\ \frac{1}{2}(1 + C_{sl}) + \frac{1}{2Ste\delta\theta_m} & -\delta\theta_m \leq \theta \leq \delta\theta_m & \text{Mushy} \\ 1 & \theta > \delta\theta_m & \text{Liquid} \end{cases} \\
 S = S(\theta) &= \begin{cases} C_{sl}\delta\theta_m & \theta < -\delta\theta_m & \text{Solid} \\ \frac{1}{2}\delta\theta_m(1 + C_{sl}) + \frac{1}{2Ste} & -\delta\theta_m \leq \theta \leq \delta\theta_m & \text{Mushy} \\ C_{sl}\delta\theta_m + \frac{1}{Ste} & \theta > \delta\theta_m & \text{Liquid} \end{cases} \\
 K = K(\theta) &= \begin{cases} K_{sl} & \theta < -\delta\theta_m & \text{Solid} \\ K_{sl} + \frac{(1 - K_{sl})(\theta + \delta\theta_m)}{2\delta\theta_m} & -\delta\theta_m \leq \theta \leq \delta\theta_m & \text{Mushy} \\ 1 & \theta > \delta\theta_m & \text{Liquid} \end{cases}
 \end{aligned}$$

Initial and Boundary Conditions

The initial and boundary conditions can be written as follows:

- Initial condition ($Fo = 0$):

$$\text{At } 0 \leq R \leq R_i, \theta = \theta_i$$

- Boundary conditions ($Fo > 0$):

$$\text{At } R = 0, \frac{\partial \theta}{\partial R} = 0$$

$$\text{At } R = R_i, -K \left(\frac{\partial \theta}{\partial R} \right)_{R=R_i} = q''_{capsule}$$

Physical Behavior

The phase change process of solidification of water inside a capsule involves four stages (Chen *et al.*, 1999, 2000). The first stage, sensible heat extraction, is the process from the initial stage to the subcooling state before water nucleation occurs. The second stage, dendritic ice formation, is the process from the start of nucleation to the completion of dendritic ice formulation. The other two stages are latent heat transfer and sensible heat transfer in the solid. Since the time interval of the second stage is relatively small, the modeling of this stage is difficult. Here, the growth of ice crystals is not taken into account and the first two stages are combined into a sensible heat extraction process for liquid water.

The one-dimensional conduction equation is written for the PCM inside a capsule, and the effect of natural convection that takes place inside the encapsulated liquid PCM is taken into account using an effective thermal conductivity, as given elsewhere (Lacroix, 1993). The effective thermal

conductivity denotes the ratio of total heat transfer rate to heat transfer rate by conduction, and is expressible as

$$K_{effective} = \frac{Nu}{Nu_{cond}} \quad (7.91)$$

Limited studies have been reported on natural convection inside an encapsulated PCM. Here, the Nusselt number correlated experimentally by Ettouney *et al.* (2005) for a capsule during melting and solidification is used.

Numerical Solution Procedure

The temperature distribution inside the problem domain is calculated by solving the heat transfer equations expressed by Equation 7.90. The solution procedure used for these energy equations is a control-volume approach described elsewhere (Patankar, 1980). The thermal conductivity K is calculated by a harmonic mean method at the control surface; the thermal conductivity for any control surface K_n results in

$$K_n = \frac{1}{\frac{1-f_n}{K_P} + \frac{f_n}{K_N}} \quad (7.92)$$

where the interpolation factor f_n is defined as

$$f_n = \frac{\frac{1}{R_n} - \frac{1}{R_N}}{\frac{1}{R_P} - \frac{1}{R_N}} \quad (7.93)$$

Here, the subscripts P and N denote control-volume nodes and n denotes the control surface.

A semi-implicit solver (Ettouney *et al.*, 2005) is employed for solving the discretized heat transfer equations. CPU time is greatly reduced for a single iteration using this solver, which requires less storage than other solvers (e.g., the Gauss–Seidel iteration method). Since the energy equation for the PCM is a nonlinear heat conduction equation, iterations are needed during each time step. For a given time step, convergence is deemed at iteration $k+1$ when $|\theta_{i,j}^{k+1} - \theta_{i,j}^k| \leq 10^{-6}$. The numerical results are then verified by testing the resulting predictions for independence relative to grid size, time step, and other parameters. The grid size used for the solution is 200 (radially) for each capsule with a time step $\Delta t = 0.1$ s. Furthermore, the overall energy balance is checked during the calculation process to verify the numerical results. At a time step, the change in energy storage in the PCM and container wall must equal the total energy supplied by the heat transfer fluid as follows:

$$\int_0^\tau Pe_f C_f (\theta_{b,out} + 1) d\tau = \sum_{k=1}^N \int_{R=0}^{R_i} 4\pi R^2 (H - H_i) dR \quad (7.94)$$

Here, $H = C \times T + S$ represents the total enthalpy of the control volume. The left side of Equation 7.94 represents the thermal energy supplied by the heat transfer fluid and the right side the thermal energy stored in the encapsulated PCM. In the calculation procedure, the numerical deviation between the two sides of Equation 7.94 is less than 1%.

7.8.4 Numerical Determination of Heat Transfer Coefficients for Spherical Capsules

In this section, we examine the variation in heat transfer coefficients using the simplified physical model in Figure 7.49. The heat transfer fluid flows past four quarter-spherical capsules that are kept at a constant temperature of 273.15 K for each segment. The side walls are taken along planes that are symmetric regarding heat transfer. At the inlet, fluid with a constant mass flow rate \dot{m} and a temperature T_{in} enters the TES system at a constant speed u_0 . The flow is assumed to be developing and steady. Here, ethyl alcohol is taken as the heat transfer fluid. This selection allows the results obtained from the numerical analysis to be compared with experimental data provided by Chen and Yue (1991). In calculating the heat transfer coefficient, the density, thermal conductivity, and dynamic viscosity of the heat transfer fluid are assumed linear or a second-order polynomial, depending on temperature. Thermophysical properties of the heat transfer fluid are given in Table 7.2 and of the capsule wall and PCMs in Table 7.3.

The primitive volume mesh for the FLUENT CFD program used to obtain solutions is constructed with the aid of the GAMBIT program. Along the entire system, 20 separate zones for each capsule zone and an additional two zones for the inlet and the outlet are formed, as illustrated in Figure 7.49. These allow specification of uniform velocity for the inlet and outflow for the outlet. For each simulation, nearly 650,000 tetrahedral cells are used.

Table 7.2 Properties of heat transfer fluids

Heat transfer fluid	Temperature, T (°C)	Density, ρ (kg m ⁻³)	Specific heat, c_p (J kg ⁻¹ K ⁻¹)	Thermal conductivity, k (W m ⁻¹ K ⁻¹)	Thermal diffusivity, α (m ² s ⁻¹)	Dynamic viscosity, μ (Pa.s)
Ethyl alcohol	−10	838.6	2253	—	1.053×10^{-7}	0.0030
	−15	842.9	2209	0.199	1.069×10^{-7}	0.0034
	−20	847.3	2149	—	1.093×10^{-7}	0.0038
Ethylene	−5	1068.3	3384	0.389	1.08×10^{-7}	7.18×10^{-3}
glycol (40%)	−10	1069.6	3367	0.383	1.06×10^{-7}	9.06×10^{-3}
	−15	1070.9	3351	0.377	1.05×10^{-7}	11.7×10^{-3}

Table 7.3 Properties of capsule wall and PCMs

Material	Phase	Density, ρ (kg m ⁻³)	Specific heat, c_p (J kg ⁻¹ K ⁻¹)	Thermal conductivity, k (W m ⁻¹ K ⁻¹)	Thermal diffusivity, α (m ² s ⁻¹)	Enthalpy change, ΔH (J m ⁻³)
Capsule wall: polyethylene	Solid	940	1900	0.35	1.96×10^{-7}	—
PCM: <i>n</i> -tetradecane	Liquid	765	2100	0.211	1.31×10^{-7}	175.2×10^6
PCM: water	Solid	803	1800	0.273	—	—
	Liquid	999.8	4217	0.561	1.33×10^{-7}	333.5×10^6
	Solid	916.8	2040	2.2	—	—

For the heat transfer fluid, the continuity, momentum, and energy equations follow:

$$\begin{aligned}\frac{\partial}{\partial x_i}(\rho u_i) &= 0 \\ \frac{\partial}{\partial x_i}(\rho u_i u_j) &= -\frac{\partial P}{\partial x_i} + \frac{\partial \tau_{ij}}{\partial x_j} + \rho g_i + S_i \\ \frac{\partial}{\partial x_i}(\rho u_i h) &= \frac{\partial}{\partial x_i}\left(k \frac{\partial T}{\partial x_i}\right)\end{aligned}$$

Here, ρ denotes density, u_i velocity component in the i direction, p static pressure, g_i gravitational acceleration in the i direction, k thermal conductivity, T temperature, and t time. Also, x_i is a cartesian coordinate and τ_{ij} is a stress tensor. Viscous heating is not taken into account since it is negligibly small.

The numerical solution is obtained using FLUENT 6.0 software. The governing equations for internal flow and heat transfer around the spherical capsules are solved with the control-volume method introduced by Patankar (1980). The SIMPLEC algorithm of Doormaal and Raithby (1984) is used to solve the coupling between velocity and pressure.

7.8.5 Heat Transfer Coefficients and Correlations

The variation of the heat transfer coefficient around the spherical capsules along the flow path is examined. The three-dimensional model shown in Figure 7.49 is applied for four capsule diameters ($D = 40, 60, 70$, and 80 mm). All capsules have a wall thickness of 1 mm. To focus better on heat transfer coefficient around the capsules, their surface temperature is taken to be constant as a result of the heat transfer fluid around them.

Heat Transfer Coefficients

A series of 120 numerical “experiments” are performed to calculate the heat transfer coefficients for various capsule diameters, mass flow rates, inlet heat transfer fluid temperatures, and capsule layers, as summarized in abbreviated form in Table 7.4. Numerical results are provided only for capsule diameters of 40 mm and 80 mm in this table. The heat transfer coefficient is seen to decrease markedly along the downstream flow. Furthermore, the heat transfer coefficient decreases as capsule diameter increases, as inlet temperature increases (or the temperature difference, $T_m - T_{in}$, decreases), and as mass flow rate decreases.

Velocities

Velocity vectors along the centerline are plotted in Figure 7.50, which shows that the flow characteristics around the capsules are different since the flow is developing. The heat transfer fluid enters the system with uniform velocity and the centerline velocity increases downstream, as is the case with internal flow in a channel. This observation supports the contention that the heat transfer coefficient changes along the flow path.

Correlations

The 120 numerical datasets are used to correlate the heat transfer coefficient via nonlinear regression using SPSS 10. The following correlation is developed by Erekan and Dincer (2009) for the heat

transfer coefficient:

$$\text{Nu}_X = 0.726(\text{Re Pr})^{0.360} \left(\frac{T}{T_s}\right)^{-20.094} X^{\frac{-450.656}{\text{Re.Pr}}} \tag{7.95}$$

Here, the correlation coefficient obtained for this correlation is high, at $R^2 = 0.950$. The numerical data are plotted with correlation curves for comparison in Figure 7.51. It is seen that the correlation agrees well with the data, as almost all numerical data falls between the correlation curves for $\text{Pe} = 500$ and $\text{Pe} = 15,000$. Since the exponent of the axial direction coordinate X is a function of the Peclet number, where $\text{Pe} = \text{Re Pr}$, two correlation curves are shown for two Peclet numbers, representing the lower and upper limits for the numerical data.

Table 7.4 Numerically obtained parameters and heat transfer coefficients for two capsule outer diameters at various capsule rows

Capsule outer diameter (mm)	Mass flow rate (kg/s)	Inlet temperature (°C)	Heat transfer coefficient (W/m ² K)					
			Row 1	Row 2	Row 3	Row 5	Row 10	Row 20
40	0.003	−5	59.65	36.20	32.19	26.33	16.49	7.56
40	0.003	−10	118.32	72.18	64.17	52.43	32.84	15.05
40	0.003	−15	175.85	107.74	95.70	78.11	48.92	22.41
40	0.003	−20	232.04	142.64	126.56	103.17	64.61	29.58
40	0.005	−5	76.18	50.59	45.92	39.07	26.76	14.66
40	0.005	−10	150.97	100.48	91.31	77.72	53.28	29.22
40	0.005	−15	224.21	149.44	135.92	115.68	79.37	43.58
40	0.005	−20	295.68	197.25	179.47	152.70	104.82	57.59
40	0.010	−5	99.53	74.08	68.99	61.50	47.17	31.76
40	0.010	−10	197.33	146.87	137.01	122.22	93.83	62.61
40	0.010	−15	293.32	218.23	203.79	181.88	139.66	94.19
40	0.010	−20	387.29	287.87	269.01	240.13	184.36	124.54
40	0.050	−5	151.28	134.39	131.98	126.55	115.48	98.75
40	0.050	−10	300.22	265.36	260.48	249.94	228.26	196.10
40	0.050	−15	446.62	393.02	385.66	370.11	338.24	292.27
40	0.050	−20	590.39	517.57	507.63	487.04	445.13	384.99
80	0.003	−5	20.20	11.35	9.58	7.32	4.00	1.33
80	0.003	−10	40.30	22.77	19.14	14.59	7.95	2.63
80	0.003	−15	60.23	34.15	28.61	21.74	11.80	3.89
80	0.003	−20	79.88	45.39	37.91	28.72	15.55	5.10
80	0.005	−5	26.92	16.18	14.05	11.29	6.89	2.92
80	0.005	−10	53.45	32.33	28.04	22.48	13.70	5.81
80	0.005	−15	79.51	48.33	41.85	33.51	20.41	8.64
80	0.005	−20	105.01	64.05	55.39	44.28	26.94	11.40
80	0.010	−5	37.90	25.61	22.85	19.48	13.43	7.29
80	0.010	−10	75.12	50.87	45.46	38.74	26.74	14.53
80	0.010	−15	111.58	75.66	67.69	57.66	39.83	21.67
80	0.010	−20	147.15	99.88	89.42	76.11	52.60	28.64
80	0.050	−5	65.19	55.26	51.96	48.75	42.11	33.30
80	0.050	−10	129.05	109.05	102.60	96.39	83.44	66.34
80	0.050	−15	191.66	161.50	152.01	142.95	123.85	98.90
80	0.050	−20	253.04	212.63	200.22	188.35	163.20	130.64

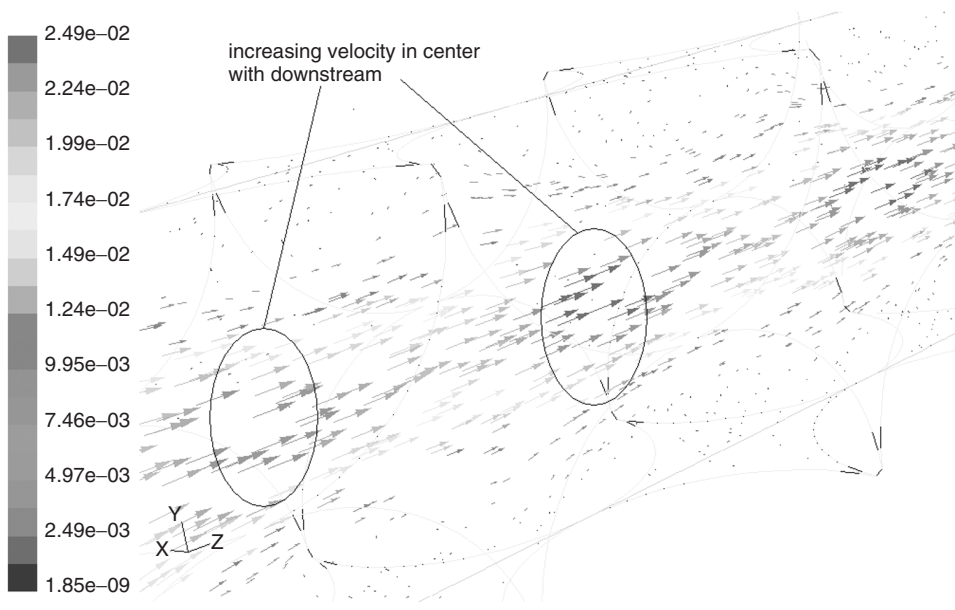


Figure 7.50 Fluid velocity vectors around the PCM capsules

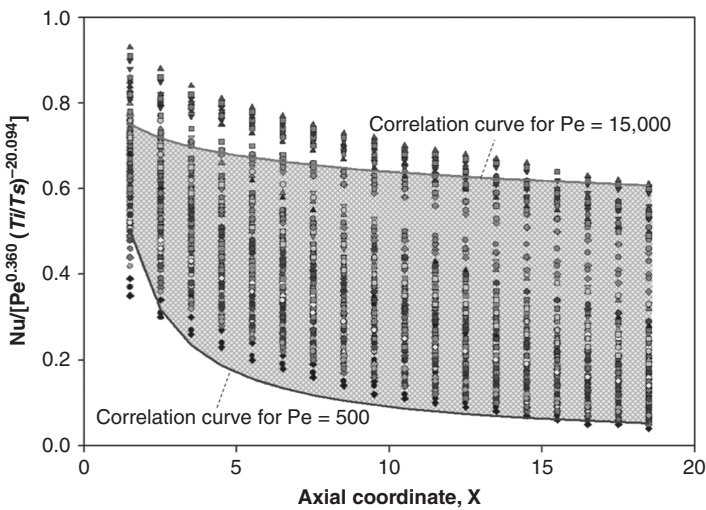


Figure 7.51 Variation with axial coordinate of the heat transfer correlations for two values of Peclet number (curves) and for numerically obtained data (dots)

To further confirm the results, we validate this correlation using experimental data from the literature. Chen and Yue (1991) proposed a correlation based on experimental data and numerical results for the heat transfer coefficient around spherical capsules. Kunii and Suzuki (1967) obtained time-averaged internal heat transfer coefficients by matching experimental measurements and theoretical results of the temperature profile for a coolant. Wakao *et al.* (1979) correlated heat transfer data published earlier for axial fluid thermal-dispersion coefficients. The corrected data for

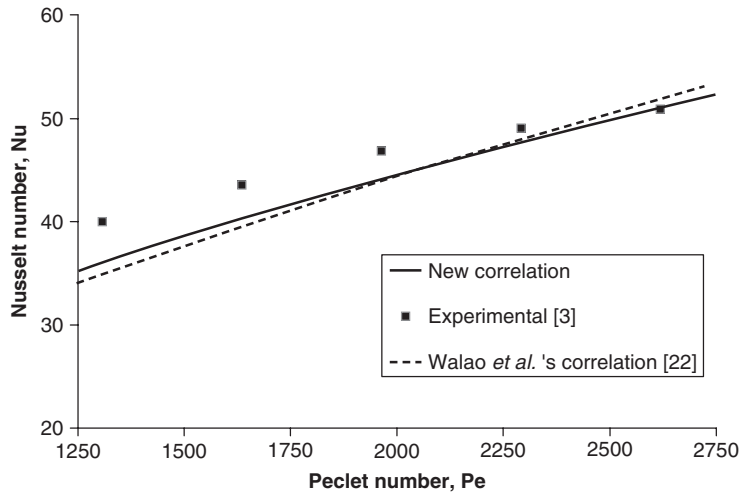


Figure 7.52 Variation of Nusselt number with Peclet number for correlation obtained here and in the literature (Wakao *et al.*, 1979) and for experimental data (Chen and Yue, 1991)

Reynolds numbers ranging from 15 to 8500 are correlated by an analogous form of mass correlation. Figure 7.52 compares the heat transfer coefficient obtained with the correlation determined here and from other studies (Chen and Yue, 1991; Wakao *et al.*, 1979). Satisfactory agreement is observed between the results in this figure.

The physical validity of the mathematical model is inspected by comparing it to predictions using experimental data. Cho and Choi (2000) determined the temperature variations inside and on the surface of a spherical capsule filled with *n*-tetradecane, along the centerline of the storage tank. To validate the numerical model with experimental data from Cho and Choi (2000), the numerical code is tested for the same geometrical and operational parameters and the same PCM (*n*-tetradecane), heat transfer fluid (40% aqueous solution of ethylene glycol), and container material (polyethylene). Properties for these materials are listed in Tables 7.2 and 7.3. The comparison of numerical results and experimental data from Cho and Choi (2000) is given in Figure 7.53(a) and (b). Although the present numerical model does not consider sensible storage in the container wall or supercooling, there is still good agreement between the numerical results and experimental data. A sharp decrease in the center temperature is more emphasized with the numerical analysis, as is also observed elsewhere (Ismail *et al.*, 2003). This decrease occurs at the end of solidification.

Effect of Other Parameters

The variation of the local heat transfer coefficient along the flow path is significant, indicating that it should not be treated as constant. Figure 7.54(a) and (b) demonstrate clearly the importance of the *x*-dependent heat transfer coefficient. The variation of time (dimensionless) for complete solidification of each capsule for different Reynolds and Stefan numbers is shown in Figure 7.54(a) for the first layer of capsules and in Figure 7.54(b) for the seventh layer. The solidification time is not sensitive to variations in Reynolds number for the first capsule, but becomes very sensitive for the seventh capsule. Hence, the effect of inlet heat transfer fluid temperature and Stefan number on the solidification time is important for the two cases. Solidification time appears to be independent of capsule diameter.

The variation of the time-dependent heat transfer rate with capsule layer is shown in Figure 7.55 for $Re = 20$ and $Re = 60$. As expected, the variation of the heat transfer rate along the flow path

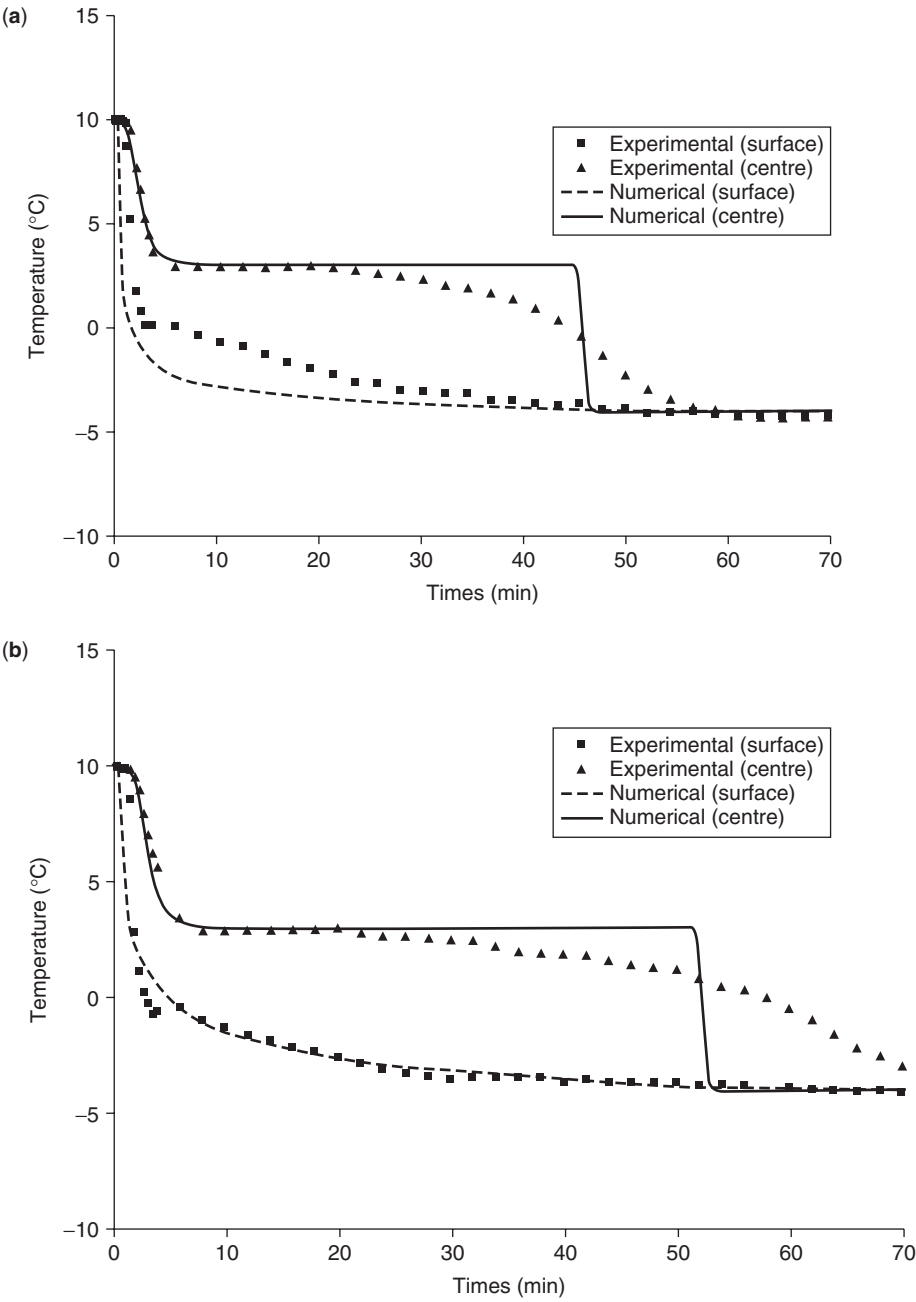


Figure 7.53 (a) Variations of experimental and numerical temperatures at center and surface points with time for first capsule layer. (b) Variations of experimental and numerical temperatures at center and surface points with time for seventh capsule layer.

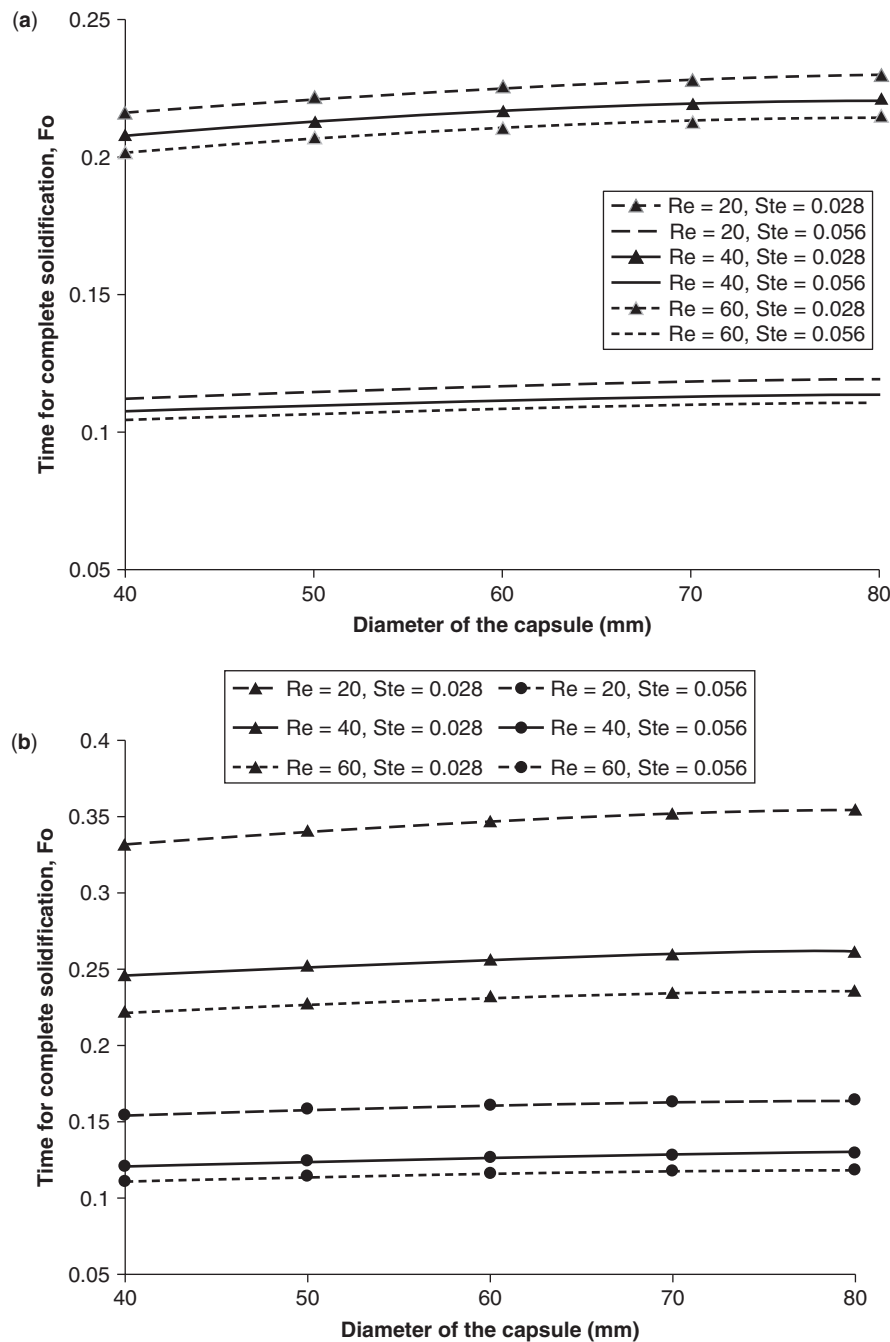


Figure 7.54 (a) Variation of dimensionless time for complete solidification with capsule diameter for several values of Reynolds and Stefan numbers, for first capsule layer (b) Variation of dimensionless time for complete solidification with capsule diameter for several values of Reynolds and Stefan numbers, for seventh capsule layer

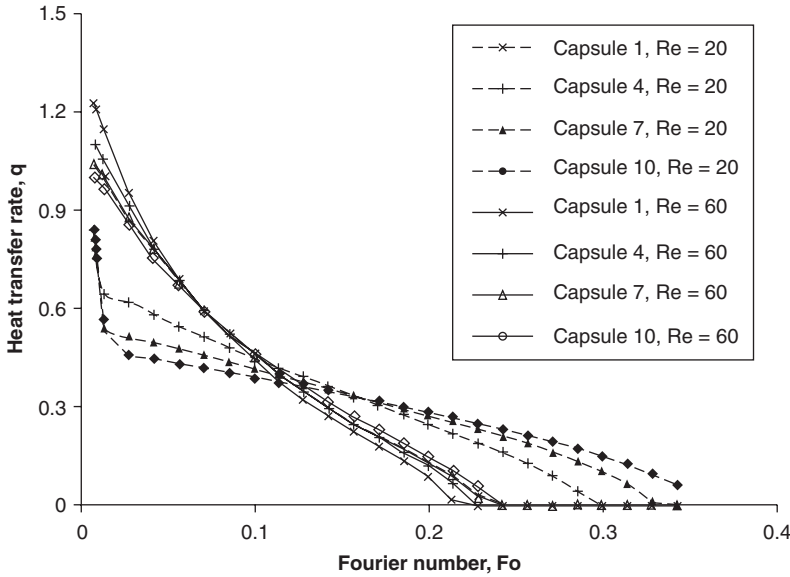


Figure 7.55 Variation of heat transfer rate with Fourier number for several Reynolds numbers and capsule row numbers

is more marked at lower Reynolds numbers. The heat transfer rate varies little along the flow path for high Reynolds numbers. But increasing the Reynolds number increases the heat transfer rate.

The effect of Reynolds and Stefan numbers on the heat transfer rate is illustrated in Figure 7.56 for the case of a 60-mm diameter capsule. The heat transfer rate is observed to increase as Reynolds number increases and heat transfer fluid inlet temperature decreases. The effect of Stefan number is more significant than that of Reynolds number.

The total energy stored as a function of time for several Reynolds and Stefan numbers is shown in Figure 7.57 for a 60-mm diameter capsule. As Reynolds number and Stefan number increase, the total charging time decreases. Note that the total stored energy increases with Stefan number at the end of charging due to sensible heat gains.

7.8.6 Closing Remarks for Illustrative Application for a Complex System

Numerical simulation has been applied to develop a heat transfer coefficient correlation that varies along the flow path for heat transfer around a spherical capsule in a cold TES. A validation shows that the correlation demonstrates good agreement with experimental data from the literature. Numerical analysis of the heat transfer behavior of an encapsulated ice TES system is performed using a temperature-based fixed-grid solution with a control-volume approach. The results show that

- the effect of varying heat transfer coefficient on the heat transfer is significant and should be considered;
- the heat transfer rate increases as Reynolds number increases and heat transfer fluid inlet temperature decreases; and
- the solidification process is primarily dependent on Stefan number, capsule diameter, and capsule row number.

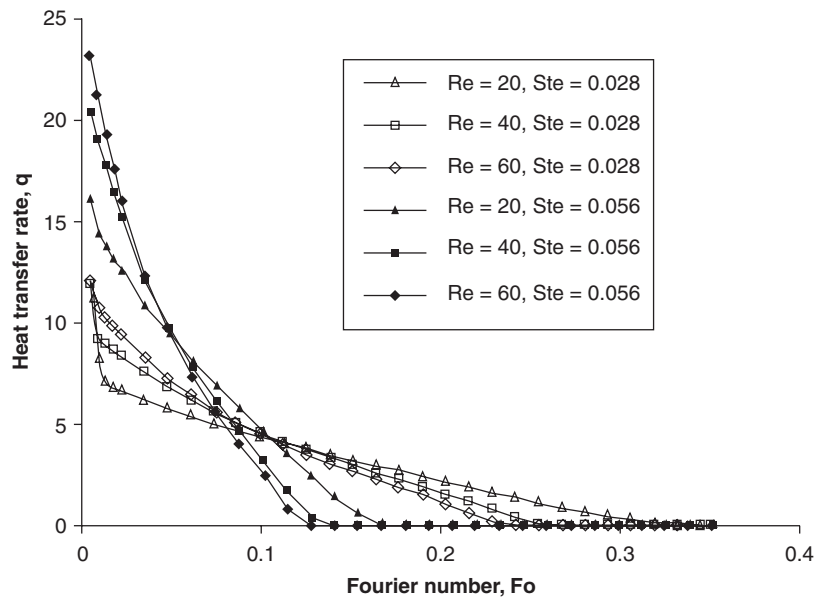


Figure 7.56 Variation of heat transfer rate with Fourier number for several Reynolds and Stefan numbers

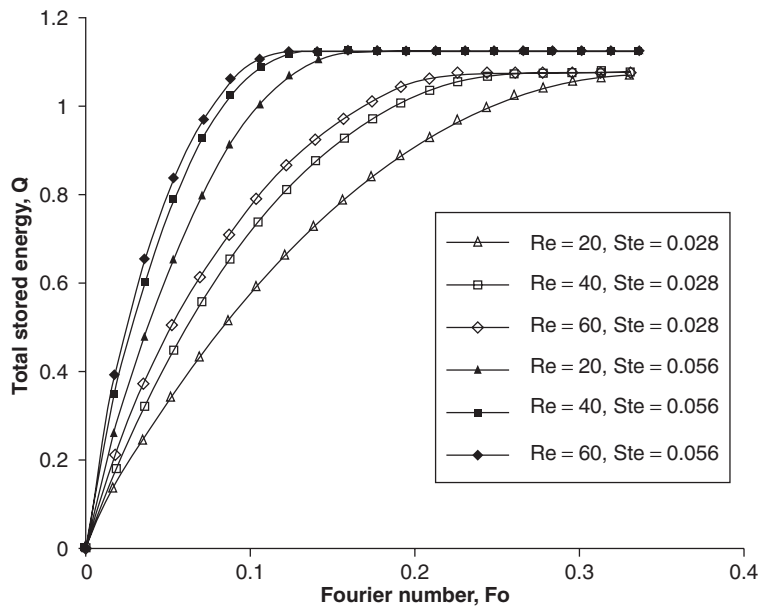


Figure 7.57 Variation of total energy stored with Fourier number for several Reynolds and Stefan numbers

7.9 Concluding Remarks

The usefulness of numerical modeling and simulation in TES applications has been demonstrated in this chapter. By considering heat transfer and thermodynamic analyses of sensible and latent TES systems, numerical simulations can provide meaningful insights into system behavior and the magnitudes of system losses.

Common practices for creating computational volumes using commercial software have been described, along with the significance of the number of volumes and the size of each. While care must be taken to ensure that a discretized volume behaves as expected, the grid should not overburden the computational algorithm with too much information. Hence a balance is sought between computational cost and complexity. A similar trade-off is required when choosing a time step size. An extremely small time step increases accuracy but increases computational cost greatly. Thus, an important factor in establishing a numerical simulation is to ensure the time step and discretization schemes are adequate for accuracy, but not overly complicated.

We have described and discussed fluid flow, which forms the basis of CFD codes, and the Navier–Stokes and continuity equations that must be solved in numerical TES simulations. The associated energy equations, including in some cases viscous dissipation, have also been described to provide a more complete understanding of the phenomena occurring in sensible and latent TES systems. An overview is included of the correct data monitoring processes for thermodynamic analyses, which are important for understanding efficiencies and losses, and which can be formulated on first- and second-law bases.

Four case studies are presented in this chapter, including two sensible and two latent TES cases. A commercial computational heat transfer and fluid dynamics software package, ANSYS FLUENT, is used. The cases incorporate various models including viscous dissipation, natural convection, and phase change. For all cases, the geometric construction and discretization of the domain into finite volumes is discussed, and simulation procedures are explained in detail. The results for all cases are examined, using FLUENT visualization tools where beneficial. Factors affecting performance criteria are explained. The fourth case study contains information about the validation and independence tests that a numerical study must satisfy. All simulations were run on a modest computer in a reasonable amount of time, and each gave insightful information into the operation of many TES systems and their components. The case studies provide examples that may prove useful for similar systems. In addition, an illustrative application for a more complex system is provided, which involves a numerical assessment of an encapsulated ice TES with variable heat transfer coefficients.

Numerical modeling and simulation of TES systems is relatively simple to perform and much less expensive than corresponding experimental investigations. The benefits of modern numerical practices are significant, since they decrease experimental costs and often provide enhanced information on the losses occurring in TES systems. Numerical investigations facilitate system optimization, and are likely to become increasingly important in the future, with the expected increase in long-term global demand for energy resources.

Nomenclature

A	area, m^2
c, C	specific heat, J/kg K ; dimensionless volumetric heat capacity ($C^0/(c_l \rho_l)$)
C_{sl}	ratio of solid–liquid volumetric heat capacity (C_s/C_l)
D	capsule outer diameter, m
Fo	Fourier number ($\alpha_f t/D^2$)
\vec{f}	wall facet
\vec{g}	gravitational force vector
h	specific enthalpy, J/kg
h'	latent enthalpy portion, J/kg

H	enthalpy, J; dimensionless enthalpy
I	destroyed exergy, J
k	thermal conductivity, W/m K
K	dimensionless thermal conductivity (k/k_l)
K_{sl}	ratio of solid–liquid thermal conductivity (k_s/k_l)
L	latent heat of fusion, J/kg
m	mass, kg
Nu	Nusselt number
p	static pressure, Pa
\bar{p}	average static pressure from monitors, Pa
Pe_f	fluid Peclet number ($Re_f Pr_f$)
Pr_f	fluid Prandtl number (ν_f/α_f)
q	heat flux, W/m ²
q^0	heat transfer rate, W
q	dimensionless heat transfer rate ($= q^0/(\alpha_l \Delta H D)$)
Q	heat transfer, J; dimensionless total stored energy ($= Q^0/(\Delta H D^3)$)
Q^0	total stored energy, J
r	radial coordinate, m
R	dimensionless radial direction (r/D)
R_i	dimensionless inner radius
Re_f	fluid Reynolds number ($\frac{\rho \cdot u \cdot D}{\mu}$)
Res	residual error
s	specific entropy, J/kg K
S	entropy, J/K; dimensionless source term ($\frac{S^0}{\rho_l \cdot c_l (T_m - T_{in})}$)
S^0	source term
Ste	Stefan number ($\frac{\rho_s c_s (T_m - T_{in})}{\Delta H}$)
t	time, s
t_w	dimensionless wall thickness of capsules ($\frac{(D - D_i)}{2D}$)
t^*	dimensionless time
T	temperature, °C or K
\bar{T}	average temperature from monitors, K
u	x-portion of velocity, m/s
U	internal energy, J
v	y-portion of velocity, m/s
V	volume, m ³
\vec{V}	velocity vector
w	z-portion of velocity, m/s
W	work, J
X	exergy of heat transfer, J; dimensionless axial direction (x/D)

Greek and Special Symbols

α	thermal diffusivity, m ² /s
ρ	density, kg/m ³
$\delta\theta_m$	dimensionless semi phase change temperature range ($\delta T_m/(T_m - T_{in})$)
θ	dimensionless temperature ($\frac{(T - T_m)}{(T_m - T_{in})}$)
ΔH	latent heat of PCM, J/m ³

Φ	viscous heating term
μ	dynamic viscosity, kg/m s
β	volumetric expansion coefficient, K^{-1}
γ	dummy variable
Π	entropy production
Ξ	exergy, J
\in	flow exergy, J
∞	reference environment
ϕ	liquid fraction
η	energy efficiency
ψ	exergy efficiency
τ	dimensionless time ($\alpha_f t / D^2$)
ν	kinematic viscosity, m^2/s

Subscripts

0	reference state
1	initial state
2	final state
<i>air</i>	air region
<i>b</i>	boundary heat interaction temperature
<i>c</i>	center
<i>ca</i>	center value at cell “a”
<i>cb</i>	center value at cell “b”
<i>ch</i>	charging
<i>copper</i>	region filled with copper
<i>CV</i>	control volume
<i>dc</i>	discharging
<i>dissipative</i>	viscous dissipation
<i>f</i>	facet value; transfer fluid
<i>ht</i>	heat transfer
<i>i</i>	<i>initial</i>
<i>in</i>	inlet
<i>inf</i>	outside of the thermal storage tank
<i>ini</i>	initial
<i>input</i>	input quantity
<i>insulation</i>	insulation region
<i>j</i>	heat interaction <i>j</i>
<i>l</i>	latent; liquid PCM
<i>latent</i>	phase change
<i>m</i>	mass-weighted; mushy phase
<i>nb</i>	neighboring
<i>ns</i>	no-slip wall region
<i>out</i>	outlet
<i>pcm</i>	paraffin phase change material region
<i>prod</i>	product quantity
<i>s</i>	slip wall region; solid PCM; inner surface
<i>source</i>	source terms
<i>t</i>	time
<i>v</i>	volume-weighted
<i>w</i>	wall; container wall or surface
<i>water</i>	water region

Acronyms

CFD	computational fluid dynamics
FEM	finite element method
FVM	finite volume method
HTF	heat transfer fluid
PCM	phase change material
SIMPLE	semi-implicit method for pressure-linked equations
TES	thermal energy storage
VOF	volume of fluid model

References

- Assis, E., Katsman, L., Ziskind, G. and Letan, R. (2007). Numerical and experimental study of melting in a spherical shell, *International Journal of Heat and Mass Transfer* 50, 1790–1804.
- Bedecarrats, J.P., Strub, F., Falcon, B. and Dumas, J.P. (1996). Phase-change thermal energy storage using spherical capsules: performance of a test plant, *International Journal of Refrigeration-Revue Internationale Du Froid* 19, 187–196.
- Benmansour, A., Hamdan, M. and Bengueuddach, A. (2006). Experimental and numerical investigation of solid particles thermal energy storage unit, *Applied Thermal Engineering* 26, 513–518.
- Bilir, L. and İlken, Z. (2005). Total solidification time of a liquid phase change material enclosed in cylindrical/spherical containers, *Applied Thermal Engineering* 25, 1488–1502.
- Chen, S.L., Chen, C.L., Tin, C.C., Lee, T.S. and Ke M.C. (2000). An experimental investigation of cold storage in an encapsulated thermal storage tank, *Experimental Thermal and Fluid Science* 23, 133–144.
- Chen, Z., Qi, X., Cheng, W. and Hu, P. (2006). A theoretical study of new-style cool storage air-conditioning systems with high-temperature water, *Energy and Buildings* 38, 90–98.
- Chen, S.L., Wang, P.P. and Lee, T.S. (1999). An experimental investigation of nucleation probability of super-cooled water inside cylindrical capsules, *Experimental Thermal and Fluid Science* 18, 299–306.
- Chen, S.L. and Yue, J.S. (1991). Thermal performance of cool storage in packed capsules for air conditioning, *Heat Recovery Systems and CHP* 11 (6), 551–561.
- Cho, K. and Choi, S.H. (2000). Thermal characteristics of paraffin in a spherical capsule during freezing and melting processes, *International Journal of Heat and Mass Transfer* 43, 3183–3196.
- Chorin, A.J. (1968). Numerical solution of Navier–Stokes equations, *Mathematics of Computation* 22, 745–762.
- Churchill, S. (1983). Comprehensive theoretically based, correlating equations for free convection from isothermal spheres, *Chemical Engineering Communications* 24, 339–352.
- De Souza, S. and Vielmo, H. (2005). Numerical analysis of water melting and solidification in the interior of tubes, *Journal of the Brazilian Society of Mechanical Sciences and Engineering* 27, 119–131.
- Doormaal, J. and Raithby, G.D. (1984). Enhancements of the SIMPLE method for predicting incompressible flow problem, *Numerical Heat Transfer* 7, 147–158.
- Eames, I.W. and Adref, K.T. (2002). Freezing and melting of water in spherical enclosures of the type used in thermal (ice) storage systems, *Applied Thermal Engineering* 22, 733–745.
- Erek, A. and Dincer, I. (2009). Numerical heat transfer analysis of encapsulated ice thermal energy storage system with variable heat transfer coefficient in downstream, *International Journal of Heat and Mass Transfer* 52, 851–859.
- Erek, A. and Ezan, M. (2007). Experimental and numerical study on charging processes of and ice-on-coil thermal energy storage system, *International Journal of Energy Research* 31, 158–176.
- Ettouney, H., El-Dessouky, H. and Al-Ali, A. (2005). Heat transfer during phase change of paraffin wax stored in spherical shells, *Journal of Solar Energy Engineering* 127, 357–365.
- Ghaddar, N. and Al-Maarafie, A. (1997). Study of charging of stratified storage tanks with finite wall thickness, *International Journal of Energy Research* 21, 411–427.
- Harris, K., Roux, J. and McCarty, T. (2003). Phenolic binder content impact on total heat transfer for fibrous insulation batts, *Journal of Thermal Envelope and Building Science* 26, 237–257.
- Hughes, T. (2000). *The Finite Element Method*, Dover Publications, Mineola, New York.

- Ismail, K.A.R. and Henriquez, J. (2000). Solidification of PCM inside a spherical capsule, *Energy Conservation and Management* 41 (2), 173–187.
- Ismail, K., Henriquez, J. and Da Silva, T. (2003). A parametric study on ice formation inside a spherical capsule, *International Journal of Thermal Sciences* 42, 881–887.
- Ismail, K.A.R. and Stuginsky, Jr, R. (1999). A parametric study on possible fixed bed models for PCM and sensible heat storage, *Applied Thermal Engineering* 19, 757–788.
- Kiatreungwattana, K. and Krarti, M. (2002). Evaluation of an internal melt ice-on-coil storage tank during partial charging and discharging cycles, *ASHRAE Transactions* 108, 1061–1071.
- Kousksou, T., Bedecarrats, J., Dumas, J. and Mimet, A. (2005). Dynamic modeling of the storage of an encapsulated ice tank, *Applied Thermal Engineering* 25, 1534–1548.
- Kunii, D. and Suzuki, M. (1967). Particle-to-fluid heat and mass transfer in packed beds of fine particles, *International Journal of Heat and Mass Transfer* 10, 845–852.
- Lacroix, M. (1993). Numerical simulation of a shell-and-tube latent heat thermal energy storage unit, *Solar Energy* 50, 357–367.
- MacPhee, D. (2008). Performance investigation of various cold thermal energy storages. M.A.Sc. thesis. University of Ontario Institute of Technology, Oshawa, Ontario, Canada.
- Oliveski, R., Krenzinger, A. and Vielmo, H. (2003). Comparison between models for the simulation of hot water storage tanks, *Solar Energy* 75, 121–134.
- Patankar, S.V. (1980). *Numerical Heat Transfer and Fluid Flow*, McGraw-Hill, New York.
- Pinelli, M. and Piva, S. (2003). Solid/liquid phase change in presence of natural convection: a thermal energy storage case study, *Journal of Energy Resources Technology* 125, 190–198.
- Regin, A.F., Solanki, S.C. and Saini J.S. (2006). Latent heat thermal energy storage using cylindrical capsule: numerical and experimental investigations, *Renewable Energy* 31, 2025–2041.
- Shah, L. and Furbo, S. (2003). Entrance effects in solar storage tanks, *Solar Energy* 75, 337–348.
- Shih, Y.P. and Chou, T.C. (1971). Analytical solutions for freezing a saturated liquid inside or outside sphere, *Chemical Engineering Science* 26, 1787–1793.
- Tao, L.C. (1967). Generalized numerical solutions of freezing a saturated liquid in cylinders and spheres, *AIChE Journal* 13 (1), 165–169.
- Voller, V.R. (1987). *Modeling Solidification Processes, Mathematical Modeling of Metals Processing Operations Conference*, American Metallurgical Society.
- Voller, V.R., Brent, A.D. and Reid, K.J. (1987). Computational modeling framework for the analysis of metallurgical solidification processes and phenomena, *Proceedings of the Conference for Solidification Processing*, Sheffield, UK, pp. 378–380.
- Voller, V.R. and Prakash, C. (1987). A fixed-grid numerical modeling methodology for convection-diffusion mushy region phase-change problems, *International Journal of Heat and Mass Transfer* 30, 1709–1720.
- Wakao, N., Kaguei, S. and Funazkri T. (1979). Effect of fluid dispersion coefficient on particle-to-fluid heat transfer coefficient in packed beds: correlation of Nusselt numbers, *Chemical Engineering Science* 34, 325–336.
- Wei, J., Kawaguchi, Y., Hirano, S. and Takeuchi, H. (2005). Study on a PCM heat storage system for rapid heat supply, *Applied Thermal Engineering* 25, 2903–2920.
- Zohoor, H. and Moosavi, Z. (2008). Increase in solar thermal energy storage by using a hybrid energy storage system, *Proceedings of World Academy of Science, Engineering and Technology* 33, 582–587.
- Zukowski, M. (2007). Mathematical modeling and numerical simulation of a short term thermal energy storage system using phase change material for heating applications, *Energy Conversion and Management* 48, 155–165.

Study Questions/Problems

- 7.1 How can numerical simulation help identify that energy-saving opportunities are offered by TES?
- 7.2 In many numerical schemes, most notably in finite difference schemes, the Courant number $v = u(\Delta t/\Delta x)$ is an important nondimensional parameter when discussing both stability and accuracy

of a numerical method involving advection. For a one-dimensional application to TES systems, where u is the velocity, Δt is the time step, and Δx is the nodal distance between points, for what values of v would you expect the method to be stable or unstable? Why?

- 7.3** In the case study in Section 7.5.1, natural convection is investigated by simulating the cooling of a hot water storage tank. Based on the resulting efficiencies, what would you expect to happen if the temperature of the water were increased or decreased? Discuss several other possible storage tank geometries and their expected relative performances.
- 7.4** What are the three main criteria for ensuring accuracy when modeling the physical domain in a numerical scheme for TES applications? Discuss how these criteria are addressed in each of the case studies in this chapter.
- 7.5** The Peclet number $Pe = VL/\alpha$ is a measure of the ratio between advection (convection) and diffusion for a particular problem, where V is the fluid velocity, L is the characteristic length, and $\alpha = k/\rho C_p$ is the thermal diffusivity. What is the Peclet number for the HTF in the case study in Section 7.5.2? What is the Peclet number for the HTF in the case study in Section 7.7.2? Should either conduction or advection be neglected in either case?
- 7.6** Try to recreate the case study in Section 7.4.1, using commercially available CFD software. Comment on the relationship between your results and the ones found in Figures 7.2 and 7.3.
- 7.7** In encapsulated ice thermal energy storage systems, porosity rate is the most important parameter affecting the maximum storage rate. The capsules may either be installed staggered or aligned in the direction of flow in the TES system.
- (a) Calculate the porosity rate for the two arrangements.
- (b) If the capsules are initially in the liquid phase at the phase change temperature T_m and at the end of the storage period are in the solid phase at the heat transfer temperature T_∞ , determine the maximum thermal storage rate per unit volume with respect to the porosity rate.
- 7.8** A nondimensional representation of governing equations makes it easier to solve equations in numerical methods. The energy equation for an encapsulated ice TES can be written as

$$\varepsilon \rho_f c_f \frac{\partial T_f}{\partial t} + \rho_f c_f u \frac{\partial T_f}{\partial x} = \frac{\partial}{\partial x} \left(\varepsilon k_f \frac{\partial T_f}{\partial x} \right) + \frac{q_{capsule}^0}{V_{CV}}$$

Using the nondimensional parameters

$$X = \frac{x}{D}, \tau = \alpha_f \frac{t}{D^2}, K = \frac{k}{k_l}, C = \frac{\rho c_p}{(\rho c_p)_l}, \alpha = \frac{k}{(\rho c_p)}, Pe = \frac{uD}{\alpha_f}, \theta = \frac{T - T_{in}}{T_m - T_{in}}$$

obtain the following nondimensional expression:

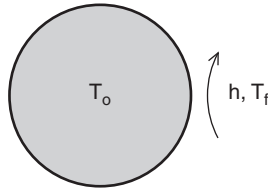
$$\varepsilon C_f \frac{\partial \theta_f}{\partial \tau} + C_f Pe_f \frac{\partial \theta_f}{\partial X} = \frac{\alpha_l}{\alpha_f} \frac{\partial}{\partial X} \left(\varepsilon K_f \frac{\partial \theta_f}{\partial X} \right) + \frac{q_{capsule}'''}{Dk_f (T_m - T_{in})}$$

- 7.9** The Nusselt number is a dimensionless temperature gradient on a surface and determines the convective heat transfer rate from that surface. For an encapsulated ice TES system, the Nusselt correlation is obtained as

$$Nu_x = 0.726 (RePr)^{0.36} \left(\frac{T_i}{T_s} \right)^{-20.094} X^{\frac{-450.656}{RePr}}$$

For $T_i/T_s = -10$ and $X = 0$ to 20, show the variation of Nusselt number for three Peclet numbers ($Pe = 500, 1000$, and $10,000$) on the same graph, noting that $Pe = Re Pr$. Discuss the effect of the Peclet number on the Nusselt number.

- 7.10** In the overall design process of a thermal system, the convective heat transfer rate is generally determined by the mean Nusselt number (\overline{Nu}), rather than the local Nu_x . For the parameters given in Problem 2, obtain an expression for \overline{Nu} .
- 7.11** A spherical capsule filled with water at a temperature T_0 is put in a refrigerated bath to observe the inward phase change process. The refrigerated bath consists of ethylene glycol at a constant temperature T_f . The bath provides a constant temperature around the capsule, and convection occurs at the interface with a heat transfer coefficient h . Assuming that the phase change process can be assumed to be one-dimensional for this scenario,
- (a) obtain the appropriate dimensionless governing equation and boundary conditions; and
 - (b) determine using numerical methods the surface temperature of the sphere, the solid/liquid interface position, and the total stored energy, all as a function of time.



- 7.12** In the case study in Section 7.8, it is emphasized that the heat transfer rate decreases and the required time for full solidification of the capsules increases as one moves downstream. What arrangements could be made in the system to achieve an almost uniform solidification for each capsule, and thereby have a more homogeneous storage? Conduct a detailed investigation, including a literature survey, on this topic.